Lunar Thermal Evolution

Insights on Crustal Structure and Radiogenics from Global Geodynamic Modeling

Sabatino Santangelo

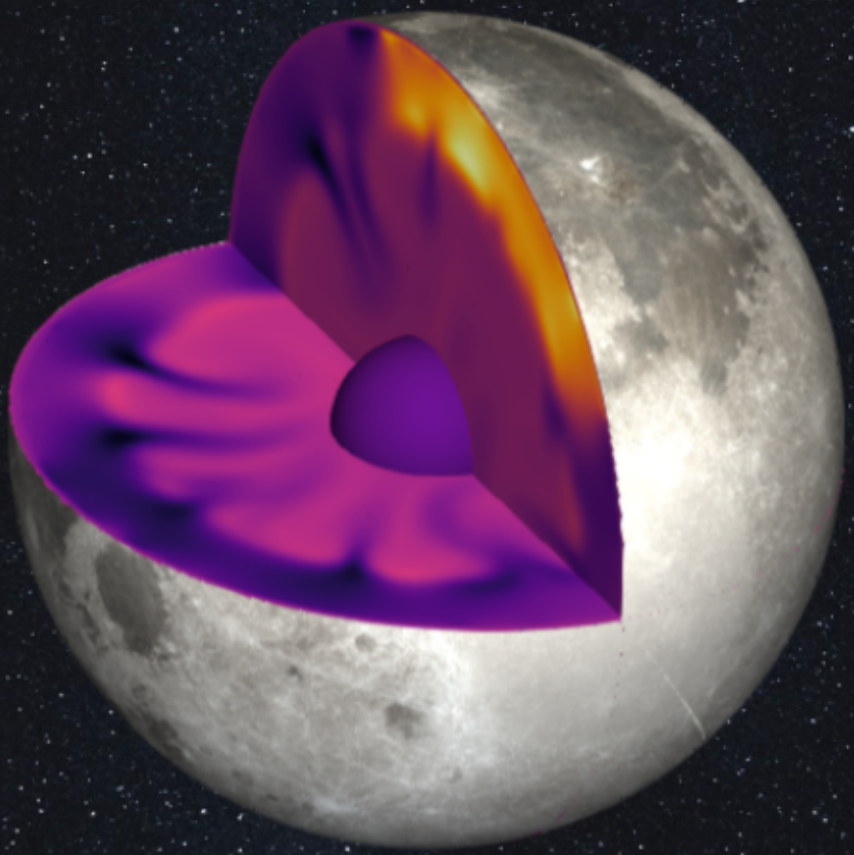

Delft University of Technology

TU Delft

DLR

Lunar Thermal Evolution

Insights on Crustal Structure and Radiogenics from Global Geodynamic Modeling

by

Sabatino Santangelo

to obtain the degree of Master of Science
at the Delft University of Technology,
to be defended publicly on Tuesday October 1, 2024 at 13:00.

Student number:	5841127	
Project duration:	January 1, 2023 – September 1, 2024	
Thesis committee:	Dr. A.-C. Plesa,	DLR, Supervisor
	Dr. ir. B. C. Root,	TU Delft, Supervisor
	Dr. A. Broquet,	DLR, Co-Supervisor

Cover: Visualization of absolute temperature field contoured to a minimum value on a quarter moon cut-out.
Style: TU Delft Report Style, with modifications by Daan Zwaneveld

TU Delft

Abstract

Surface heat flux, which can be defined as the heat flowing out of the interior of a planetary body, provides important constraints on the present-day thermal state of the lunar interior. Measurements, performed in situ during the Apollo program, and from orbit by Chang'E 1, Chang'E 2, and by the Diviner radiometer instrument indicate important lateral variations in surface heat flux on the Moon (~5 - 180 mW/m^2). The differences between Apollo 15 and Apollo 17 measurements have been explained by the presence of an anomalous region, enriched in uranium (U), thorium (Th), and KREEP (Potassium, Rare Earth Elements and Phosphorus) elements, located on the lunar nearside. Previous modeling efforts also identified crustal thickness and thermal conductivity variations as secondary causes for surface heat flux differences. However, detailed explanations for the remaining two estimates and their implications for the evolution of the Moon remain highly debated. Additionally, the structure and properties of this putative KREEP-rich layer have remained uncertain.

Therefore, this study proposes a new global geodynamic model of lunar thermal evolution that includes lateral variability in the distribution of radiogenics, crustal thickness and thermal conductivity. The present setup is capable of simultaneously explaining the variability between the Apollo 15, Apollo 17, and Region 5 heat flux values, while also providing further constraints on the KREEP layer structure and lunar crustal properties. The research question addressed in this work is: what is the effect of crustal structure (radiogenics, thickness and thermal conductivity distribution) on 3D thermal evolution models of the Moon?

Here, we model the interior dynamics and thermal evolution of the Moon after magma ocean solidification using the fluid solver GAIA. We investigate the abundance and distribution of radiogenics on the Moon, and how they shape the interior temperature distribution through time. Additionally, we account for a spatially variable crustal thickness, derived from gravity and topography data. We also include a laterally variable thermal conductivity model, derived from porosity data, which we constrain using the nearside-farside differential thermal state of lunar basins. We model and vary the extent of a putative KREEP layer underlying the PKT (Procellarum KREEP Terrane) region. We enrich the KREEP layer and crust in heat-producing elements compared to the mantle, simulating an asymmetrical distribution of radiogenics as an initial condition.

We find that measurably lower heat flux values at the lunar south pole compared to Apollo 15 and 17 require KREEP material to extend at least partly beneath mare Serenitatis. In this case, the Apollo 15 measurement would be representative of the KREEP region average heat flux, while Apollo 17 would lie on its edge. On the other hand, a smaller KREEP region (<1200 km in diameter) would make the Apollo 17 location representative of non-KREEP terrane, and show heat flux comparable to south pole values. This is incompatible with estimates based on the Diviner Lunar Radiometer Experiment onboard Lunar Reconnaissance Orbiter, although uncertainties associated with these estimates are unclear. Heat flux measurements that will be performed by the NASA CLPS-CP12 mission at Schrödinger crater will provide key information to exclude one of these two scenarios, and thus potentially constrain the extent of the KREEP layer underneath PKT region.

Our results also show that a laterally variable thermal conductivity helps reducing the interior temperatures, while maintaining surface heat flux distribution unchanged. We find an effective farside crustal conductivity of ~2 W/(mK) (comparable to that of compact anorthosite) to best match the differential basin relaxation constraints, implying negligible effect of a porous megaregolith layer on the thermal conductivity. In the KREEP region, we favour models with effective crustal conductivity below 2 W/(mK), suggesting that lunar volcanic basalts may have an even lower bulk conductivity than the 2.6-2.7 W/(mK) values considered here. This could be due to the porosity of lunar volcanic material, a more complex layering of basaltic eruptions, or the effect of the temperature and pressure dependence

of thermal conductivity. Although our model setup is simplified, it provides novel insights on the distribution of radiogenics and crustal properties on the Moon, and shows the potential to further constrain the asymmetrical character of lunar evolution.

Preface

This master's thesis gives proper closure to many important cycles in my life. It marks the end of a 9-month project, a year of research at the DLR-Institute of Planetary Research, a two-year master's degree, and a five-year university journey. The amount of hours, effort, and emotion I put into this work perfectly reflects this journey. It is a natural consequence of the passion I had on the very first day of each of these experiences; each time greater, more aware, more mature.

However, I would be lying if I said that what I have accomplished over these years is solely the product of my own merits. Many people gave a piece of themselves to enrich me and this work, and I cannot help but acknowledge and show my gratitude to at least some of them, as this work is ultimately dedicated to all of you. To the people who made this dream my life.

Each step in the making of this thesis and each opportunity to take these steps has been given to me by my supervisor, Ana-Catalina Plesa, who is simply the best mentor a student could wish for and the perfect embodiment of the scientist I strive to become. Similarly, this work would not exist without the contribution of my co-supervisor, Adrien Broquet, who not only contributed his amazing science, but also taught me how to be a better scientist through a care for this work that rivals mine. For the incredible time I spent, and will continue to spend, at DLR, I must thank the head of my department, Doris Breuer, who welcomed me into a top-notch group of researchers without knowing almost anything about me, and yet giving me the opportunity I had always dreamt of. Finally, I would not have known anything about the subject of this report, and I certainly could not have made it my master's thesis work, without my TU Delft supervisor, Bart Root, who gave me all the tools to make the most of this project. And of course, a huge thanks goes to all my colleagues at DLR-PLP for creating such a dynamic, motivating and safe work environment that I simply could not leave even after this project.

But a work like this, and a passion like mine, is not only built from university learning and studying; it comes from a lifetime of love and support. For this, my family deserves the biggest thank you of all. In particular, to my mom, who never fails to show me how to be the best possible version of myself. To my dad, who gave me a moral compass for this journey that has never wavered, allowing me to walk in the right direction under all circumstances. To my sister, who gives me the purpose to aim for the stars, which I will reach with her and make hers. To my brothers of B-Club, who will always stand by me through my achievements and downfalls, no questions asked. And to all of my huge, loving family, who will always be my home and the root of my successes.

Sabatino Santangelo
Berlin, September 2024

Contents

List of Figures

List of Tables

Nomenclature

Abbreviations

Abbreviation	Definition
BiCGS	Bi-Conjugate Gradient Stabilized method
BSE	Bulk Silicate Earth
BSM	Bulk Silicate Moon
CLEP	China's Lunar Exploration Program
CLPS	Commercial Lunar Payload Services
CMB	Core-Mantle Boundary
CSFD	Crater Size-Frequency Distribution
EBA	Extended Boussinesq Approximation
FHT	Farside Highlands Terrane
GRAIL	Gravity Recovery and Interior Laboratory
HPEs	Heat-Producing Elements
ISRU	In-Situ Resource Utilization
KREEP	Potassium (K), Rare Earth Elements and Phosphorus
LMO	Lunar Magma Ocean
LRO	Lunar Reconnaissance Orbiter
PKT	Procellarum KREEP Terrane
SPAT	South-Pole Aitken Terrane
TFQMR	Transpose-Free Quasi-Minimal Residual method
...	

Symbols

Symbol	Definition	Unit
A	Area	[m^2]
c_V	Specific heat capacity at constant volume	[J/(kg K)]
e	Specific Internal Energy	[J/kg]
g	Gravitational Acceleration	[m/s^2]
H	Surface conductive heat flux	[W/m^2]
k	Thermal conductivity	[W/(mK)]
n	Unit vector normal to a surface	[-]
Q	Total Heat Production	[W/kg]
p	Pressure	[Pa]
q	Heat flux	[W/m^2]
Ra	Rayleigh Number	[-]
T	Temperature	[K]
u	Three-Dimensional Velocity Vector	[m/s]
V	Volume	[m^3]
α	Thermal Expansivity	[1/K]
β	Isothermal compressibility	[Pa^{-1}]
ΔT	Temperature Contrast	[K]
η	Viscosity	[Pa s]
κ	Thermal Diffusivity	[m^2/s]

Symbol	Definition	Unit
Λ	Longitude	[deg]
λ	Latitude	[deg]
ρ	Density	[kg/m^3]
σ	Deviatoric Component of the Stress Tensor	[Pa]
τ	Stress tensor	[Pa]
ϕ	Porosity	[%]

Part I

Introduction

1

Introduction

The Moon is one of the most studied bodies of the Solar System, having been the focus of over 82 missions. Since the first soviet Luna program in 1959 (Nayler, 1969), and through the historic manned Apollo program in the 1960s and 70s, the Moon is once again in the spotlight of space exploration. The wealth of data collected over the decades, including over 380 kg of lunar samples (Heiken et al., 1991) and the most precise gravity field measurements to date from the GRAIL (Gravity Recovery and Interior Laboratory, Konopliv et al., 2013) mission, offered invaluable insights into planetary science. One of the main results of these endeavours is related to the formation of the Moon: our satellite is thought to have formed hot, as a consequence of a gigantic impact between early Earth and another proto-planet. Such a catastrophic event released immense amounts of energy, which contributed to raising the temperature of the newborn Moon, to the point of melting its whole surface and at least its upper mantle. This phase in lunar history is referred to as the Lunar Magma Ocean phase (LMO) (Canup et al., 2023).

Despite the close proximity and amount of available data on the Moon, many questions remain unsolved regarding its present-day state and the processes that shaped it over 4.5 Ga of evolution. In particular, the overarching question driving much of current lunar science is: Why did the Moon experience such profoundly asymmetrical evolution? This key interrogative arose as soon as, in 1959, the soviet mission Luna 3 obtained the first image of the lunar farside, that is, the hemisphere permanently concealed to an Earth-bound observer (Figure 1.1 a.; Nayler, 1969). From a first glance, it was already apparent that the two hemispheres followed different evolutionary paths. The farside is heavily cratered and lacks traces of any resurfacing process (i.e., the farside surface is geologically older), compared to the darker, basalt-flooded nearside (geologically younger). Since then, an important portion of lunar science and exploration has been focused on investigating the character of the lunar asymmetry and providing possible explanations for its development.

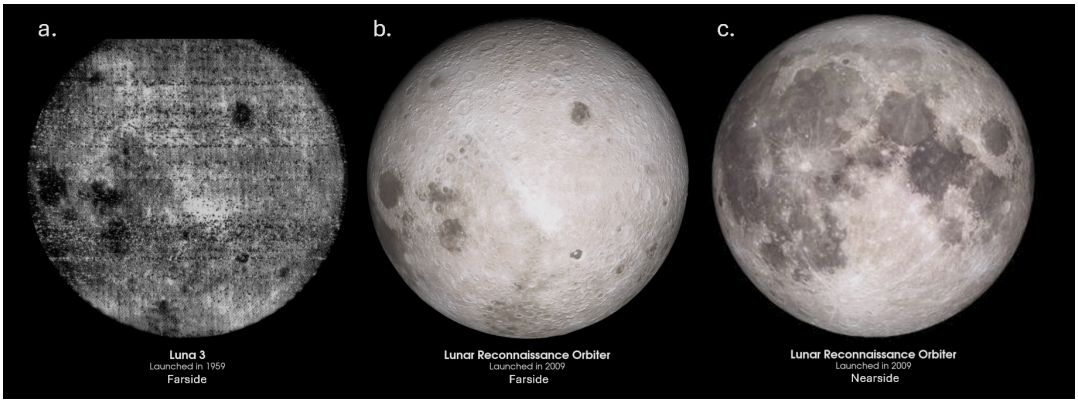

Figure 1.1: The first picture of the lunar farside, obtained by soviet mission Luna 3 in 1959 (a). Hemispherical LRO (Lunar Reconaissance Orbiter) composite images of the lunar farside (b) and nearside (c). The staggering differences between the two hemisphere are apparent in the LRO images, with dark basaltic maria covering only ~1% of the farside compared to the ~30% surface flooding on the nearside. The observation of the lunar asymmetry constituted a revolutionary turning point in lunar sciences. Credits: NASA's Goddard Space Flight Center Scientific Visualization Studio (https://svs.gsfc.nasa.gov/cgi-bin/details.cgi?aid=4109)

Since 1959, more expressions of the asymmetric evolution of the Moon were discovered through the analysis of several datasets. Indeed, what is often referred to as lunar asymmetry includes, but is not limited to, gravity field, topography, volcanic activity, HPE (Heat-Producing Elements) distribution, crustal magnetization, impact processes, crustal thickness distribution, and true polar wander (Konopliv et al., 2013; Nozette et al., 1994; Broquet and Andrews-Hanna, 2024b; Lawrence et al., 1999; Wieczorek, 2018; Ding and Zhu, 2022; Broquet and Andrews-Hanna, 2024a; M. A. Siegler et al., 2016). In particular, the Moon does not display a clear dichotomy, but rather an asymmetry or large-scale regional differences (Figure 1.2). When referring to the lunar asymmetry, we generally denote the differences between Procellarum KREEP Terrane - PKT and Feldspathic Highland Terrane - FHT (Figure 1.2, Jolliff et al., 2000), while the South Pole Aitken Terrane (SPAT or SPA) constitutes yet another anomalous region on the farside. Compared to the surface average, the PKT region shows lower radial gravitational acceleration (by ~100 mGal), topography (by ~2 km), crustal thickness (by ~6 km), and crustal magnetization (by ~1 nT) (Konopliv et al., 2013; Nozette et al., 1994; Broquet and Andrews-Hanna, 2024a, respectively).

The PKT region also hosts the largest amount of eruptive material and concentration of radiogenic isotopes on the lunar surface, with more than 10 km of basaltic lava being estimated within its major craters, and up to 12 ppm thorium concentration observed on the surface (Broquet and Andrews-Hanna, 2024b, Lawrence et al., 1999). Regarding impact processes, the FHT region is geologically older by crater counting, not displaying any form or resurfacing; additionally, large farside basins are surrounded by thicker crust, while their nearside counterparts seem to be more viscously relaxed (Ding and Zhu, 2022). Lastly, it should be noted that the asymmetry reflected by the mentioned characteristics developed either during or almost immediately after LMO solidification (4.5-4.3 Ga), not giving time to the primordial FHT crust to record any globally homogeneous evolutionary phase. The most apparent piece of evidence in this sense is the absence of volcanic basalts older than 3.6 Ga on the lunar farside (Figure 1.4, Hiesinger et al., 2023).

In addition, upcoming lunar exploration programs call for a better understanding of lunar evolution and its current state. For instance, the Chinese Chang'e 6 mission (Xin, 2024), flown between May and June this year, and NASA mission CP-12 (part of the Commercial Lunar Payload Services - CLPS deliveries, Schonfeld (2023)), scheduled for launch in 2025, both have as main scientific goal further investigations of the asymmetrical evolution of the Moon. The former will provide, for the first time, measurements of FHT soil composition from returned samples, while the latter will collect seismic data (i.e. wave velocities and impact frequency), coupled with surface heat flux measurements within SPA.

Looking further in time, more than 20 missions are envisioned to continue the exploration of the Moon in the decade 2025-2035, developed by 9 national agencies (Gaddis et al., 2023). Among oth-

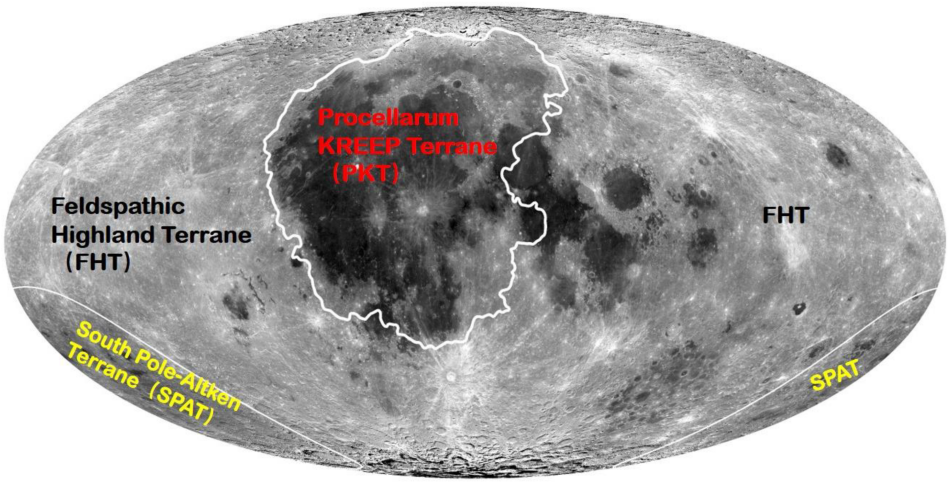

Figure 1.2: Mollweide projection of lunar global map. The three major terranes are highlighted in red (Procellarum KREEP Terrane - PKT), black (Feldspathic Highland Terrane - FHT) and yellow (South Pole Aitken Terrane - SPAT), following the definitions of Jolliff et al. (2000). Image credit: J. Zhang et al. (2023)

ers, ARTEMIS program by NASA/ESA and China's Lunar Exploration Program have as final goal the harnessing of lunar resources. The final aim is to evaluate the possibility of building and surviving on the Moon, which constitutes the current frontier of space exploration. To this end, it is crucial to understand as much as possible about the body and its history; in particular, its present-day thermal state, crustal structure and composition across the surface contain pivotal information to be exploited during a "colonization" process. Among the resources of interest for these pioneering endeavors, abundance and distribution of HPE, thermal gradients and crustal material, which are investigated in this study, have a pivotal role (Crawford et al., 2023).

When talking about lunar crust, we refer to an outer layer of up to 80 km of light anorthositic rock, covered in debris or volcanic ejecta. This layer is lighter, less dense and has different properties compared to the underlying mantle. This study investigates the structure of lunar crust, in terms of thickness and properties, by evaluating its effects as an insulating layer on the global evolution of the body. The research question we investigate in the present work is the following: What is the effect of crustal structure on 3D thermal evolution models of the Moon? We use large-scale thermo-dynamical simulations as a tool to investigate the cooling of the Moon throughout 4.5 Ga (secular cooling). Inputs to such models are the initial thermal state and interior structure of the Moon, with a focus on crustal properties, namely: thermal conductivity and thickness of the outermost porous layer within the crust (megaregolith), crustal thickness distribution, distribution and abundance of HPE.

We use a global geodynamic thermal evolution model based on two previous studies (Laneuville et al., 2013, 2018). The main constraints to our model from in-situ measurements of heat coming from the subsurface, namely the heat flux experiments performed by the crews of Apollo 15 and 17, which proved the thermal state to be laterally variable even between locations only 800 km apart (~7% of lunar circumference). We improve on the model setup by Laneuville et al. (2013, 2018) by including parameters and secondary results coming from regional-scale modeling (Siegler & Smrekar, 2014; Warren & Rasmussen, 1987)

In the following sections, we will briefly follow the main stages of lunar evolution, focusing on the aspects that have the most influence on the present modeling set-up. Thereafter, we will give a description of the measurements that constrain our model and an overview of previous modeling efforts upon which we build the present research.

1.1. Formation of the Moon

In order to choose the conditions with which to initialize thermal evolution models, it is crucial to understand the primordial state of the planetary body in question, including initial temperature profile, distribution and abundance of HPE. In our case, estimations of the abundance of HPE within lunar interiors are tightly related to its formation. The most accepted hypothesis for the formation of our satellite is through a giant impact between early Earth and another proto-planet. However, open questions remain about what kind of impact and post-impact processes contributed to form the Moon. The giant impact formation of the Moon emerged as the leading hypothesis in the ”Origin of the Moon” conference in 1984, for it best explains the high angular momentum of the system, the small lunar core, the similar oxygen isotopic composition and hot start of the Moon (Canup et al., 2023). Since then, it became more and more established that giant impacts are efficient triggering events for the formation of natural satellites (Canup et al., 2023).

The first formulation of the giant impact hypothesis for lunar formation involved a Mars-sized impactor hitting the Earth during its last phases of accretion, with a velocity comparable to the escape velocity of the system. This formulation is referred to as ”Canonical Impact” hypothesis (Canup et al., 2023). The primary challenge to the ”Canonical Impact” is that the Moon appears strikingly similar to Earth in composition, even more so when estimating the respective primordial compositions. The following summary of the similarity between Earth and Moon compositions is based on from Canup et al. (2023), where a much more complete and complex review can be found. Refractory lithophile (Mg, Al, Ca, U, Si, Th) and weakly siderophile (V, Cr, Mn) elements are very similar in the bulk silicate Earth (BSE) with respect to the bulk silicate Moon (BSM). In contrast, volatile alkali (K, Na, Rb, Cs) are 5 to 6 times more depleted in the BSM, C and other elements of higher volatility are depleted by factors 5-200 while FeO appears significantly higher in the lunar mantle. Looking at the isotopic anomalies, commonly relied upon as the best tracers for sample parentage identification, the situation does not improve. Also the isotopic composition of many elements found on the Earth and Moon is only slightly different (Si, Ti, Ca, O, and W). Lastly, based on the available lunar samples, the BSM is thought to be much drier than the BSE.

In order to overcome the challenges of a ”Canonical Impact”, some more articulate hypotheses have been formulated and reviewed (Canup et al., 2023), which we will briefly describe. ”Hit and Run” impacts, characterized by a larger velocity and more tangential trajectory, can lower the impactor material to 40-60% of the lunar-forming disk, improving but not solving the isotopic similarities scenario. Other ”high angular momentum/high energy” impact scenarios have been proposed, including small fast impactor hitting a fast-rotating earth (factor of 2-3 faster than present-day angular momentum) in a retrograde trajectory or low-speed large impactor (>40% Earth mass).

These scenarios are potentially more consistent with the compositional similarities, forming disks of predominantly target material, but are all affected by the problem of extensive extraction of angular momentum post-impact. For instance, if this was a common satellite-formation mechanism, we would have observed planets that are thought to have kept their angular momenta almost unchanged (e.g., Mars) spinning much faster at present. Other explanations, such as an Earth-like composition of the impactor or complete post-impact disk equilibration seem highly uncertain (Canup et al., 2023).

Although no conclusive evidence has been produced to disentangle the exact process that formed the Moon, similarities between BSM and BSE compositions appear well-established and robust to measurements obtained with more recent technologies. For the purposes of this study, it is the latter aspect that is most relevant; specifically, it allows us to assume a BSM thorium composition comparable to that of Earth (0.0795 ppm, McDonough and Sun (1995)), similar to what is done in (Laneuville et al., 2018).

1.2. Lunar Magma Ocean Phase

The Lunar Magma Ocean (LMO) phase is thought to be responsible for lunar differentiation and crust formation. The LMO model of primordial lunar differentiation was proposed following the Apollo 11 mission in 1969, and developed with the continuous analysis of lunar samples. In particular, ferroan

anorthosites samples, which are comprised of >90% plagioclase and thought to be globally distributed, bore interstitial mafic minerals and geochemical signatures consistent with a large-scale melting event (Gaffney et al., 2023). The crystallization of a global magma ocean is considered the main cause of differentiation and heterogeneous distribution of radiogenics within the Moon and, as such, it provides key initial conditions to our simulations. Therefore, a brief description of the LMO phase and its crystallization process is provided in the following paragraphs.

Although several different positions exist on the timeline and detailed nature of the events occurring during the LMO phase, we aim to give a general overview of the topic. Firstly, the mineral composition and isochron aging of lunar samples indicate a major magmatic event occurred between 4.3-4.5 Ga (Gaffney et al., 2023). This evidence is compatible with the solidification of a deep magma ocean (order of hundreds of km). Whether the LMO was a global layer, or whether the Moon was depth-wise wholly or only partially molten is yet to be confirmed, since all available samples were collected on the nearside. Conclusive evidence on at least a subset of these interrogatives may come from the first farside samples just returned to Earth by the Chang'e 6 mission flown in June 2024.

Currently, the LMO is believed to have occurred as a global layer on the primordial Moon, and that lunar differentiation was caused by the fractional crystallization of the magma. Fractional crystallization is a process by which different minerals crystallize from the molten magma at different temperatures as it cools, causing a sequential separation of solid and liquid phases. The first phases to crystallize are Mg-rich olivine and orthopyroxene, then clinopyroxene; all of these mafic minerals are denser than the remaining liquid, meaning that they sink to the bottom of the melt (Gaffney et al., 2023). These three phases constitute a primordial cumulate mantle. After the crystallization of about ~75-80$\%$ of the LMO, anorthitic plagioclase starts to form; this phase is less dense than the surrounding Fe-rich melt, making it float and form a global anorthositic crustal layer (primordial lunar crust).

During the fractional crystallization, a crucial role is played by incompatible elements. Incompatible elements are characterized by high ionic radius and electric charge, meaning that it is energetically unfavourable for them to fit in the crystalline lattice of solidifying minerals. Thus, being "incompatible" with the solid phase, these elements tend to migrate to the receding melt and become increasingly concentrated in it. Therefore, the residual melt confined between cumulate mantle and floatation crust becomes increasingly enriched in elements such as Fe and Ti, and crystallizes to form what is referred to as ilmenite bearing cumulates after about 95$\%$ solidification (Gaffney et al., 2023). Lastly, after >99$\%$ crystallization, the residual melt is highly enriched in the most incompatible elements, including U, Th and KREEP elements (Potassium, Rare Earth Elements and Phosphorus). Such a layer, usually denoted urKREEP in lunar science, would crystallize last and be trapped between the crust and the mantle.

Following the LMO crystallization, the higher density of IBC and urKREEP with respect to the underlying cumulates is likely to drive re-mixing events, such as mantle overturn scenarios (Gaffney et al., 2023). Mantle overturn can be imagined as a natural consequence of the crystallizing LMO. We have seen how IBCs (high in Fe content) solidify later than mafic minerals, meaning that IBC are located at shallower depths than mafic cumulates, although they are denser than such minerals. Thus, the mantle is in a gravitationally unstable state during the last stages and upon complete crystallization of the LMO. This configuration is prone to trigger a relatively fast process of IBC and urKREEP sinking, referred to as lunar mantle overturn (Li et al., 2019).

However, concerning mantle overturn, two pieces of evidence must be kept in mind in the interest of the following discussion; firstly, most volcanic activity throughout lunar history has occurred on the nearside (~97$\%$ of all mare basalts occur on the nearside (Elardo et al., 2020)), including the oldest eruptions (~4Ga ago, Hiesinger et al. (2023)). Secondly, the high correlation between the measured high-Ti regions and basaltic eruptions on the lunar surface (Figure 1.3 c,d) implies that the magma source includes the IBL.

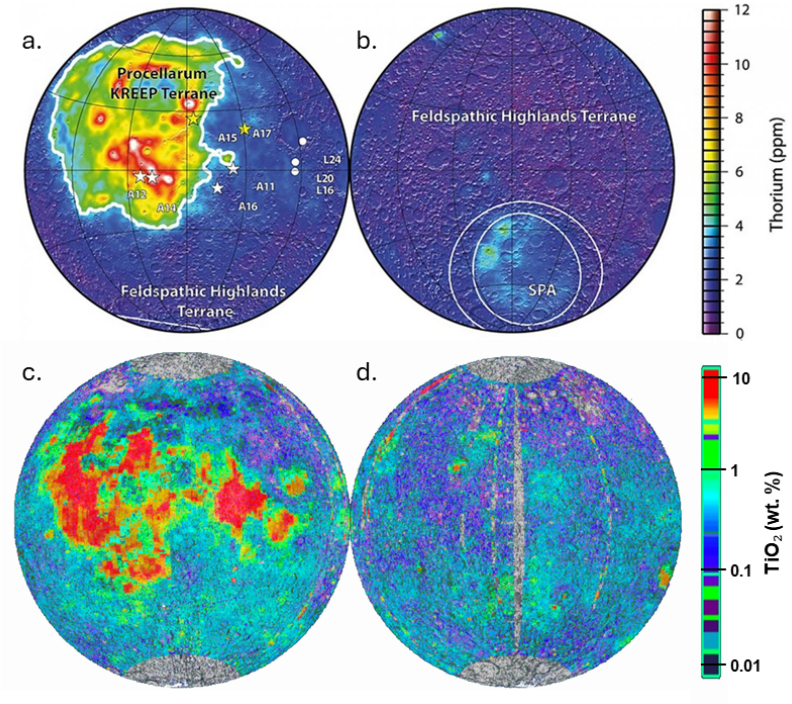

Figure 1.3: The distribution of thorium on the near (a) and farside (b) from the Lunar Prospector mission. Major terranes are highlighted, along with the landing locations of Apollo 11, 12, 14, 15, 16, 17 and Luna 16, 20, 24 missions (Credits: Laneuville, M. et al (2013) Journal of Geophysical Research: Planets). Titanium abundances of the near (c) and farside (d), obtained from NASA's Clementine spacecraft; the red color indicate titanium abundances that largely exceed that found on terrestrial rocks. Titanium concentrations correlate to any basaltic eruption, while thorium seems to have reached the surface only within Oceanus Procellarum region. Image credit: Lunar and Planetary Institute.

The asymmetric distribution of incompatible elements in available data (Figure 1.3), coupled with the early and asymmetrical onset of lunar volcanism, entails an early and efficient process of concentration of incompatible elements underneath the nearside crust. Mantle overturn seems to be a feasible candidate for bringing incompatible elements (Gaffney et al., 2023) from the subsurface to the lower mantle. However, this just shifts the question to the identification of a subsequent process that concentrated or kept the heavy incompatible elements in the nearside shallow mantle, of which a number of suggestions have been proposed (e.g., Zhang et al., 2022; Liang et al., 2024).

One of the problems with the asymmetry starting to form after LMO crystallization is related to the timing of these processes. In particular, HPE concentration below the nearside must have happened quickly and efficiently enough to almost completely inhibit farside eruptions from the very onset of lunar volcanism (~4Ga). On the other hand, if HPE migration happened during LMO crystallization, it would imply that incompatible elements could have migrated from farside to nearside before the first volcanic eruptions, explaining the asymmetrical onset of volcanism. However, this requires explaining why the nearside would start hotter than the farside and, thus, stay molten for a longer time-span. Although we do not provide any conclusive answer to such interrogatives, we implicitly use the hypothesis of asymmetrical crystallization (or, equivalently, very efficient asymmetry formation) to perform the present research. In particular, we initialize our thermal evolution simulation, from LMO crystallization, assuming that all asymmetries in the crustal structure are already emplaced.

1.3. Mare Volcanism

The main process of secondary crust formation on the Moon is often referred to as ”Mare volcanism”. The word ”mare” (latin for ”sea”) is commonly used for lunar basaltic eruptions that flooded impact basins. Due to the lower albedo of volcanic basalts, circular lava ponds on the lunar surface resembled water bodies to the first observer who named them (i.e. Galileo Galilei, 1610). Lunar volcanism is

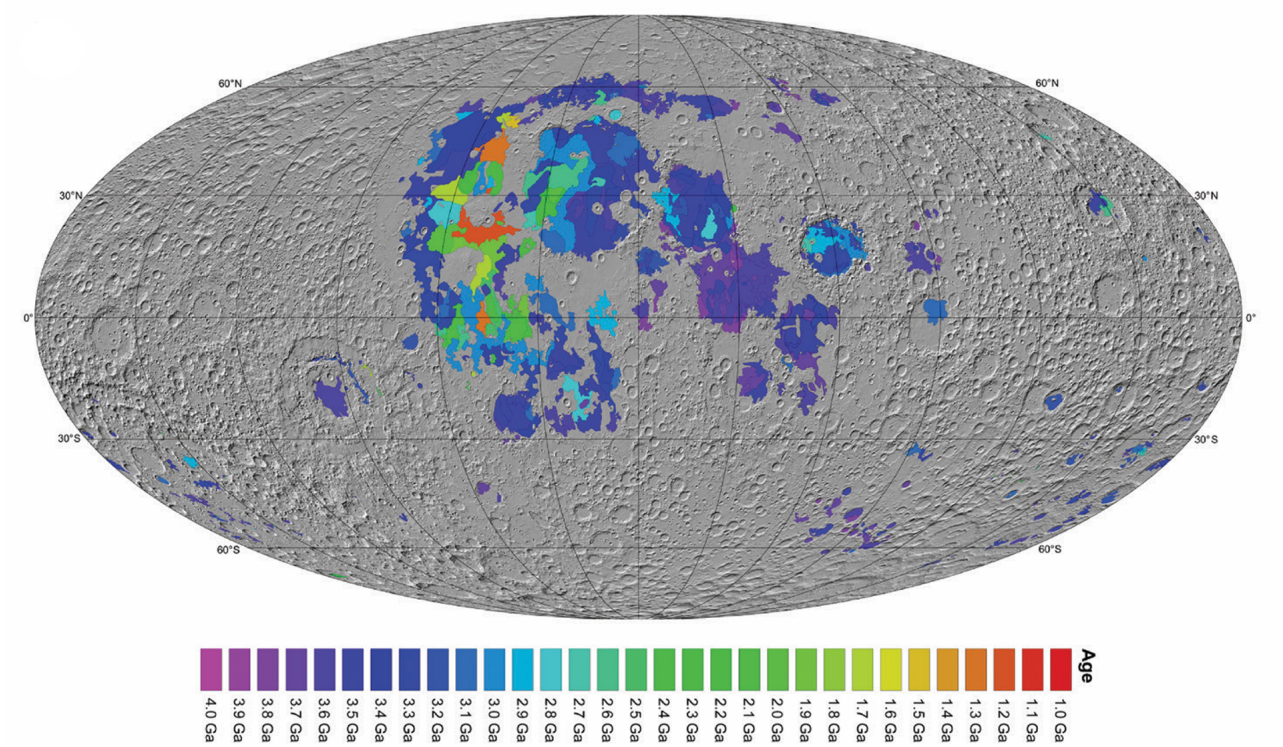

Figure 1.4: Chronology map of lunar maria based on crater size-frequency distribution (CSFD), taken from Hiesinger et al. (2023). This chronology is consistent with the isochron aging data proposed by Shearer et al. (2023).

one of the most apparent results of asymmetric evolution (Figure 1.1). Indeed, the main distinction between lunar terrane is based on its volcanic history: the nearside region where basalts flooded multiple basins and most of the spaces between them is what we refer to as PKT. As opposed to PKT, we use the acronym FHT to indicate regions on the Moon where primordial anorthositic crust has only been processed through impact gardening.

One of the aspects of interest for the present study is the magmatic history of the Moon, and its implications on thermal evolution. In particular, based on the studies by Shearer et al. (2023) and Hiesinger et al. (2023), lunar nearside magmatism has been active throughout most of its evolution, with visible basalts being dated between 1 and 4 Ga 1.4, with a major peak between 3.8 and 3.2 Ga. However, the onset of lunar volcanism may even predate the 4 Ga estimate, based on dating of basaltic clasts from lunar meteorites. Early activity is thought to be associated with cryptomaria, that is, old basaltic maria that got covered by impact ejecta to the point of being invisible at present (Hiesinger et al., 2023; Shearer et al., 2023). These estimates shift the lower bound of lunar activity to 4.35 Ga, immediately after the main magmatic event mentioned in Section 1.2. Farside activity, on the other hand, ceased much earlier, about ~2.5-3.0 Ga (Hiesinger et al., 2023).

1.4. Lunar Megaregolith

In section 1.2, we mentioned that the lunar crust formed as a light plagioclase layer floating above the residual magma ocean. Thereafter, secondary crust emplacement mainly occurred within the nearside PKT region, covering most of its surface (Section 1.3). The entirety of lunar surface outside mare regions was only processed through impacts and weathering, keeping the oldest surface record in the inner solar system (Hiesinger et al., 2023). In the present study, we are interested in the lateral and vertical structure of lunar crust. Therefore, we will briefly describe the state-of-the-art understanding of these aspects (more information can be found in the extensive review work by Plescia et al., 2023).

Following LMO crystallization (Pre-Nectarian and Nectarian, 4.2-3.8 Ga), ejecta from the formation of major lunar basins produced a thick layer of debris and fractured crust, often called megaregolith

(Plescia et al., 2023). This period roughly corresponds to the Late Heavy Bombardment (LHB, 4.1-3.8 Ga ago), and saw the formation of most lunar basins, including SPA, Crisium, Nectaris and about 60 others (Ji et al., 2022). Megaregolith material is thought to be ranging in size from giant boulders to micron-size grains, forming a deep breccia deposit. It is possible to divide the megaregolith into two sub-layers: an upper megaregolith, made of ejecta transported during LHB, and a lower megaregolith consisting of fractured but autochthonous crust (Plescia et al., 2023). Megaregolith layer thickness is highly debated in literature, ranging from a few to tens of kilometers (e.g., Thompson et al., 1979, Richardson and Abramov, 2020).

On top of the megaregolith, later reworking of basin-formation deposits and local volcanic material produced a thinner layer of smaller grain-size debris, that is classically referred to as lunar regolith. The thickness of this layer is thought to vary from a few meters to a kilometer, and is stratigraphically composed of countless overlapping blankets of ejecta, deposited throughout the evolution of the Moon (Plescia et al., 2023).

The lateral variability of regolith and megaregolith properties is highly unconstrained (layering, thickness, thermal conductivity, and so on; Plescia et al., 2023). In-situ measurements and remote sensing methods (e.g., Wieczorek et al. (2013)) indicate significant lateral heterogeneity in these quantities, suggesting that first-order modeling of properties variability in the outermost layers can be beneficial to thermal evolution models.

1.5. Research Objectives

The main motivation for investigating the effects of crustal structure on global thermal evolution models of the Moon comes from research gaps arising from both observations and modeling efforts. In this section, we will briefly introduce the main observables and modeling results that provide the basis for the present study. Thus, we will provide a description of how our research question follows from previous results.

1.5.1. Available Observables

Present-day heat flux measurements constitute the main observable considered in this study. Heat flux represents the amount of heat passing through a medium, and can be computed as: $k \cdot \nabla T$, expressed in W/m^2, where k is the thermal conductivity of the medium and ∇T is the thermal gradient between two points. Therefore, measuring this quantity on a planetary surface can provide information on the thermal state of the subsurface or its thermal properties, making it particularly interesting for numerical models of planetary interiors.

On the Moon, this quantity has been measured, both in-situ and remotely, in multiple instances: firstly, Apollo 15 and Apollo 17 (1970 and 1972, respectively) measured heat flux values in the order of 10-20 mW/m^2 (in-situ), by means of heat-flow probes (Langseth et al., 1976). Secondly, remote observations from Diviner Lunar Radiometer Experiment onboard LRO suggested a lower bound value of 3-6 mW/m^2 for surface heat flux close to the lunar south pole (i.e. Region 5, Paige and Siegler, 2016). More recently, a peak heat flux of 180 mW/m^2 was inferred by M. Siegler et al. (2023) from the modeling of Chang'E 1 and 2 remote-sensing data, at the Compton-Belkovich location. To put this last measurement into perspective, heat flux values in excess of 150 mW/m^2 are usually found at active volcanic regions on Earth (Davies & Davies, 2010). However, there is no clear evidence of active volcanism at the Compton-Belkovich region.

Two main caveats should be considered when interpreting the Region 5 and Compton-Belkovich estimates. Firstly, the amount of uncertainty related to the Diviner and Chang'E measurements is unclear in the respective studies (i.e. Paige and Siegler, 2016; M. Siegler et al., 2023). Secondly, they are not direct measurements and, therefore, are not as robust or reliable as the two Apollo measurements. Additionally, all mentioned estimates are affected by some observational bias, as they have been taken solely on the nearside, meaning that their relation to farside and global average values is difficult to estimate (Figure 1.5).

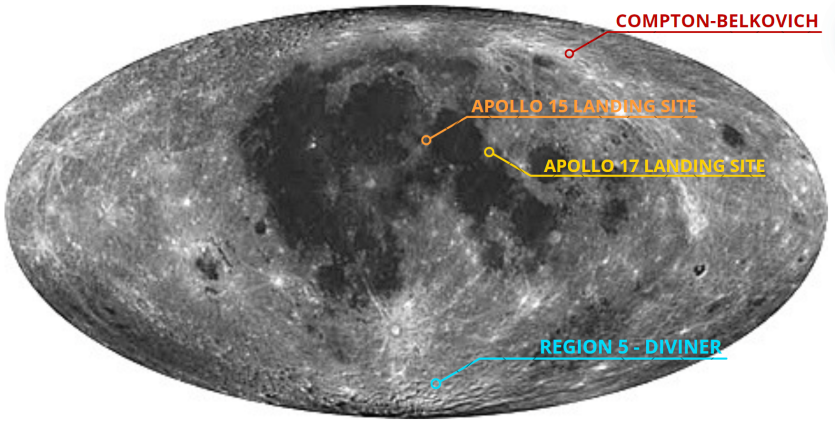

Figure 1.5: Mollweide projection of lunar map, highlighting the locations where measurements of interest have been taken. The landing locations of Apollo 15 and 17 are represented in orange and yellow, respectively. Compton-Belkovich region, where the Chang'E missions measured peak heatflux is highlighted in red. Lastly, the region in blue represents Region 5, north-east of Haworth crater, which corresponds to the Diviner measurement. All measurements are taken on the same hemisphere (nearside) and, in particular, the two Apollo datapoints fall at the edge of two maria, close to Oceanus Procellarum.

In any case, even though limited to the nearside, these measurements already show large variability in heat flux (3 orders of magnitude), which implies significant lateral variability in thermal state or thermal properties across the 4 locations. In particular, it is crucial to understand the scale at which each heat flux value is representative of a thermal state (whether local or regional), and how these relate to global average heat flux. In turn, addressing such aspects can shed light on the present-day subsurface temperature distribution and evolutionary path that produced the heat flux distribution we observe.

1.5.2. Previous Modeling Efforts

Due to the high variability between the four heat flux measurements described in section 1.5.1 (i.e. Apollo 15 - 18 mW/m^2; Apollo 17 - 14 mW/m^2; Region 5 - 3-6 mW/m^2; Compton-Belkovich - 180 mW/m^2), no model is yet capable of explaining the relative differences between all four in a single set-up. However, various studies have attempted to find a satisfactory explanation for the heat flux variability between the two Apollo sites, revisiting the measurement strategies and testing the effect of detailed terrain models (among others Warren and Rasmussen (1987), Grott et al. (2010), Siegler and Smrekar (2014)). The main findings of these three studies can be summarized as follows:

- The two Apollo heat flux measurements are not representative of the global average, due to their proximity to a radiogenically enriched terrane (PKT, Figure 1.3) and mare-edge heat flow focusing effects (Warren and Rasmussen, 1987; Grott et al., 2010).
- Plausible range for global average heat flux values is 10-14 mW/m^2 (Warren & Rasmussen, 1987).
- Plausible range for basal heat flux (i.e., heat flux at crust-mantle interface) is 7-13 mW/m^2 within the Apollo 15 and 17 landing site region (Imbrium-Serenitatis region, Siegler and Smrekar, 2014).
- Sub-surface radiogenic enrichment is identified as the main cause of the heat flux variability (Siegler & Smrekar, 2014).
- Crustal thickness variations, crustal thermal conductivity variations and near-surface radiogenic enrichment are found to have a secondary effect on heat flux variability (order of 5 mW/m^2, Siegler and Smrekar, 2014).

Nevertheless, the aforementioned studies were limited to regional and local scale (both spatially and depth-wise), due to the unavailability of any other heat flux observations at the time, and the limited computational power to perform large-scale 3D computations. These limitations are acknowledged in the above studies; for instance, the necessity to include regional and local scale findings within global

models of thermal evolution is explicitly mentioned in Siegler and Smrekar (2014). Moreover, the authors suggest to include crustal thickness and thermal conductivity distribution in a global evolution model, while ensuring consistency with the heat flux ranges they found. This approach, combining regional and global scale, can produce further constraints and new insight concerning the location and extent of a putative subsurface radiogenic anomaly.

To this end, more recent studies have been able to construct 3D global lunar evolution models to explain the difference between the two Apollo measurements (Laneuville et al., 2013), and even include Region 5 lower bound (Laneuville et al., 2018). These models provided a novel and insightful perspective on lunar thermal evolution, proving that a thermal asymmetry is likely to be still present below the PKT region. In addition, a number of scenarios for the depth and concentration of a circular HPE anomaly were tested, tightening the related constraints. In particular, some interesting results can be summarised as follows:

- An 80°-90° angular diameter KREEP region can explain at the same time Apollo 15, 17 and Diviner measurements
- Main HPE enrichment is to be found below the crust and not spread within it, to ensure consistency with timing of lunar volcanism
- Region 5 heat flux value is representative of all terranes sufficiently far from PKT anomaly
- FHT crust should be less enriched in HPE compared to the values in Figure 1.3

In the above studies, the crustal structure was simply treated as a constant thickness layer of uniform properties (with the exception of KREEP region HPE enrichment). This causes a degeneracy in the identification of specific locations on the Moon, which are only identified through their radial distance from the center of PKT. In addition, a perfectly symmetrical insulating layer (crust) during cooling can inhibit the formation of secondary thermal anomalies. It is also unclear whether these two models are consistent with the global and basal heat-flow predictions provided in Siegler and Smrekar (2014). Lastly, the best-fit models in both Laneuville et al. (2013) and Laneuville et al. (2018) produce a gravity anomaly of about -500 mGal and of the same size of the KREEP-induced thermal anomaly (angular diameter 80-90 deg). Multiple plausible explanations for the absence of such an anomaly in the gravity data are discussed, including compensation through crustal thinning, but not explicitly shown in the model outputs.

1.5.3. Research Question

Improving on the setup of Laneuville et al. (2018), this study proposes a global thermal evolution model that is consistent with the findings of regional models. In particular, the aim of the present model is to mimic the treatment of crustal thickness and thermal conductivity proposed in Siegler and Smrekar (2014), while extending it on a global scale. The models in Laneuville et al. (2013, 2018) did not include a laterally variable crustal thickness, which is a key differences with respect to the present setup. Indeed, a laterally variable crustal thickness allows to eliminate the location degeneracy and enables a more thorough understanding of the different terranes within their geographical context. Moreover, it is possible to update the crustal thickness inversion, informing it of the KREEP-induced thermal anomaly, to compensate the related gravity anomaly.

From a global modeling perspective, we expand the parameter space exploration performed in Laneuville et al. (2013, 2018), testing different sizes, depths, distribution, and abundance of HPE within the KREEP region. The current model is aimed at bridging the gap between regional and global scale, in order to provide a more complete overview of the asymmetrical evolution of the Moon and constrain it using the largest available set of geophysical constraints. For instance, numerous studies explicitly highlight the need to further investigate the distribution of radiogenics and crustal properties on the Moon. For instance, in Gaffney et al. (2023), with respect to investigating the geographical location and extent of a subsurface KREEP anomaly. In Warren and Rasmussen (1987), with respect to the effect of a megaregolith layer (subsurface porosity up to tens of km) often overlooked in models. Lastly, in Laneuville et al. (2018), where the regional representativeness of the Apollo heat flux measurements is said to be still unclear.

The main research question of the present study: ”What is the effect of crustal structure (radiogenics, thickness and thermal conductivity distribution) on 3D thermal evolution models of the Moon?” can be divided into two sub-questions, which are investigated in the following chapters:

- To what extent does the implementation of laterally variable crustal thickness in 3D evolution models improve our explanation of present-day measurements of surface heat-flux on the Moon? (Part II)
- Can present-day lunar heat flux and crustal thickness constrain megaregolith layer thickness and thermal conductivity of lunar crust? (Part III)

In the following chapters, we will delve into the theoretical background that provides the foundation of this work, the methods used to approach the research questions, the results of the study, the discussion and conclusions drawn from said results and, lastly, the verification and validation of all tools used during the completion of the present work.

2

Theoretical Background

In the following chapter, we discuss the theoretical concepts that underlay the study of planetary evolution, and their mathematical formulation. Thereafter, we describe the set of material parameters that are involved, showing how mathematics, geochemistry, and planetary science can be combined together to study the evolutionary history of the Moon. However, being all following concepts applicable to any terrestrial planet, we keep the description general and relevant to the study of multiple planetary bodies.

Understanding how planetary bodies evolved to display the surface features observed today requires a highly interdisciplinary approach, addressing constraints from different planetary datasets. Geology, geophysics, astronomy, petrology, chemistry are just a subset of scientific fields influencing the way we study and model the thermal and chemical evolution of planets. The necessity for such a broad set of constraints is due to the fact that planetary science is a data-scarce field. Therefore, all available constraints must be included, from earth-based or space-bound remote sensing to in-situ analyses. For instance, surface samples from the Moon, and meteorite samples from the Moon and Mars, which are uniquely available to analyze on Earth, have had immense value in providing insights not only into composition but also into the formation of these bodies. However, even in the case of the Moon, let alone further-away objects, it is the lack of data that ultimately limits our understanding of its deep interior and evolution.

The most fundamental process all planets undergo over billions of years is the thermo-chemical evolution of their interior. This large-scale process is dependent on the internal heat budget and thermophysical properties of each body, which highly influences mantle dynamics. Similar to a water-filled pot on a stove heated from below, the heat transport through silicate mantles is influenced by the movement of material in the interior of planets. Although the common experience and definition of solid rock is that of an immobile crystal lattice, this is not the case under all conditions. Here, the key difference is caused by the timescale of observation; we are looking at the behaviour of solid rocks throughout billions of years. In this context, we should imagine a planetary mantle as a highly viscous fluid, which is often simulated in laboratory experiments with dense sugary solutions (Davaille, 1999). Thus, planetary mantles can slowly flow (order of millimeters to centimeters per year) due to buoyancy differences caused by temperature or composition.

2.1. Dynamics and Thermal Evolution

In this section, we discuss how the interior structure and heat transport regime within a terrestrial planet affects its geologic history. Subsequently, we describe how such concepts can be applied to different bodies, how we can model them and what we can derive from the results.

2.1.1. Interior Structure

After the accretion of solar system planetesimals from the proto-planetary disk, larger bodies undergo the process of differentiation, with the smallest observed differentiated body being asteroid 4 Vesta

(~525 km in diameter; Neumann et al., 2014). This can be thought of as the means by which a rotating object subject to its own gravity can redistribute its mass to attain a more stable state. In general, the most stable state is that of an oblate (pole-flattened) spheroid with the most dense material (metal alloys) concentrated at its center and less dense material (silicates) surrounding it. In order to achieve differentiation, a planetesimal must be heated to the point of at least partially melting its metals and silicates, in order to allow the flow or percolation of denser compounds to the deeper interior (Tosi et al., 2014). At this stage, heating mostly occurs through three processes: the radioactive decay of short-lived isotopes (i.e., ^{26}Al and ^{60}Fe), the kinetic energy released from accretion or impacts between proto-planets, and the release of gravitational potential energy upon the onset of differentiation itself or any redistribution of mass (Tosi et al., 2014). Thus, the heat budget (and mass) of the body will control its differentiation process.

Interior dynamics and thermal evolution of a planet strongly depend on its interior structure and composition. The first properties usually inferred are the size and density of the three major reservoirs: core, mantle, and crust. Direct observation of the thickness and shape of these layers is only possible through seismic analyses, which are only available for Earth, Moon, and Mars. For other planetary bodies, the interior structure is estimated using more indirect observations; in particular, using low-order gravity field data (i.e., C_{20} and C_{22} coefficients), the figure (shape), and orbital precession rate it is possible to estimate the polar moment of inertia factor of a planet (Breuer & Moore, 2015). The moment of inertia provides information on the differentiation of a body, based on how much it diverges from that of a perfectly homogeneous sphere. Moment of inertia estimates, combined with planetary mean density, can provide first order information on the interior structure of a planet. However, two observables (moment of inertia factor and mean density) are not enough to produce a unique solution; for example, there is always a possible trade off between core size and density, which can not be disentangled without other data coming from complementary measurements (e.g., magnetic field or tidal interaction) (Breuer & Moore, 2015).

Additional constraints of critical importance for the inference of planetary interior structures are the compositions of the various layers (chemical and/or mineralogical). Knowing the general composition of a body can already improve the estimates of the various layer densities; for instance, core density estimates can depend on the available amount of light elements that can bond with iron to produce lighter core alloys (e.g. sulfur). In addition, experimental analysis of surface samples unlocks further information; through dating and source identification of samples it is possible to obtain information on the bulk composition of the body and the properties of its layers. The former information is crucial for choosing appropriate initial conditions for thermal evolution, as will be discussed extensively in the following sections, whereas the latter can further improve the understanding of the layered structure acquired during with the early stages of planetary formation and evolution.

2.1.2. Thermal and Chemical Convection

The interior dynamics of terrestrial planets are driven by thermal convection. When a planetary mantle (as any fluid) is heated from within or below, and cooled from above, it may become gravitationally unstable, meaning that colder material sinks into the mantle (downwelling) and hot material rises to shallower depths (upwelling). This process produces a circulation, mixing the mantle and increasing the efficiency of heat transport and eventually heat-loss to space; this is what we refer to as mantle convection. Heat loss through the surface competes with heating coming from the core and from within the mantle (due to the decay of radioactive isotopes).

In order for convection to occur, driving forces (buoyancy) need to overcome resisting forces, largely determined by the material viscosity, causing stresses and deformations that propagate to the surface. In turn, these can cause the appearance of specific geologic features on the surface (e.g., rifts, ridges, volcanic provinces, etc.), which can be observed interpreted as signatures of their source processes. For this reason, understanding planetary thermal evolution is crucial to interpret surface features in terms of interior dynamics and gain insight on their formation and evolution.

In addition to thermal buoyancy, convection can be affected by spatial variations in density, caused

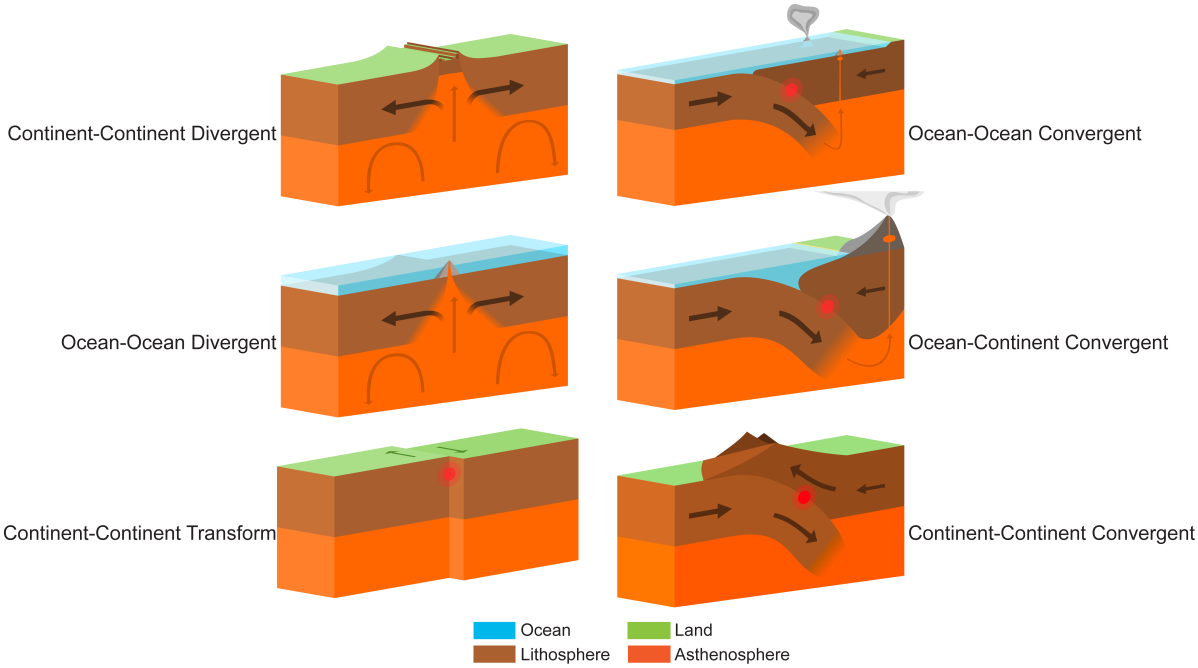

Figure 2.1: Sketch showing three types of diverging plates scenarios (left), and three types of converging scenarios (right). Image credit: Adapted from Wikimedia Commons user Domdomegg, CC BY.

by chemical differences and solid-solid phase transitions. An initially unstable chemical layering configuration (denser material above lighter material), for instance arising from magma ocean solidification, is prone to overturn and remix the interior, producing a spike in heat transport and then settling again in a more stable configuration. Alternatively, in a chemically stable layering, thermal anomalies must overcome the pre-existing density differences to enable advection of material. If whole-mantle convection is inhibited by strong chemical layering, convection can occur independently in chemically distinct layers; in this case the corresponding heat-transport is less efficient (Breuer & Moore, 2015). Similar enhancing or impeding effects are caused by isochemical phase changes of minerals, which change their crystalline structure (and, thus, density) when reaching specific temperature and pressure thresholds (Breuer & Moore, 2015).

2.1.3. Tectonic Regimes

On Earth, the plate tectonic regime, which uniquely characterises the planet's surface with respect to all other terrestrial bodies, is an expression of the underlying mantle dynamics. Viscous stresses caused by mantle circulation have fragmented the stiff lithosphere above into multiple plates. In addition, a rheologically weaker layer (asthenosphere) sits between the lithosphere and the deeper mantle, allowing the tectonic plates to move as if floating on top of the convecting mantle. Thus, mantle convection drives the movement of the plates (Figure 2.1), pulling them apart where mantle material up-wells and produces new lithosphere (e.g., mid-ocean ridge, Figure 2.1 left panels), and making them converge at regions where heavier oceanic lithosphere sinks into the mantle and gets recycled (downwelling, Figure 2.1 right panels). This recycling process allows for efficient heat transfer from interior to surface, leading to various forms of volcanism and topographic modification. In addition, crustal recycling brings water and HPE back into the mantle, allowing it to keep higher temperatures and decreasing its viscosity, ultimately enhancing convection. Therefore, the whole surface of Earth is distinctly characterised by its segmentation and signatures of the ongoing interior processes, with a geologically young oceanic crust (~200 Ma) and older continental crust (~2 Ga).

On the other hand, when observing the surfaces of other terrestrial planets, the first difference compared to Earth is the absence of any coherent plate boundaries or direct evidence of ongoing plate tectonics. Most terrestrial planets are characterised by a single global immobile plate, referred to as

"Stagnant Lid" (Breuer and Moore, 2015; Schubert et al., 2001), which is largely decoupled from the dynamic mantle underneath. In this case, the heat flow from mantle to surface is mainly conductive (through the lid). In stagnant lid planets, mantle cooling is less efficient than on Earth, and this has a large influence on the thermal evolution of planets. The main outcome of the stagnant-lid regime is the presence of much older surfaces, possibly never recycled (e.g. 4.3-4.5 Ga old crust on the Moon), which bear witness to most, if not all planetary history. On Mercury, Moon or Mars, which are thought to have operated in a stagnant lid regime over their entire history, giant basins and heavily cratered surfaces have been preserved over billions of years and can still be observed today.

2.1.4. Conservation Equations

The mathematical description of a mantle flow is analogous to that of a fluid continuum. Therefore, in order to simulate the thermal evolution of terrestrial planets, the system of conservation equations of mass, momentum, and energy needs to be solved. In addition, the system must be closed by including an equation of state, which describes how density varies under a temperature or pressure contrast. In the following, we list the basic equations used for modeling the interior dynamics of rocky planets.

Conservation of mass

For the scope of the present study, we will formulate the equation of mass conservation over a control volume. This means that, within our system or domain, mass will stay constant over time. Thus, the equation can be written as:

$$\frac{\partial \rho}{\partial t} + \nabla \cdot (\rho \boldsymbol{u}) = 0; \tag{2.1}$$

where ρ represents density and $\boldsymbol{u}$ is the three-dimensional velocity vector. As previously mentioned, we consider the flow incompressible, meaning that density changes (both in time and space) are assumed negligible except in the buoyancy term of momentum conservation (ρg). Therefore, in equation 2.1, the partial derivative of density with respect to time will be equal to zero and the scalar density term will not play a role in the field divergence, allowing to rewrite mass conservation in the following concise notation:

$$\nabla \cdot \mathbf{u} = 0. \tag{2.2}$$

Conservation of Momentum

For the momentum conservation equation (Navier-Stokes equations), we will use the Lagrangian formulation for an incompressible fluid, which can be written as:

$$\rho \frac{\mathrm{D}\boldsymbol{u}}{\mathrm{D}t} = -\nabla p + \nabla \cdot \boldsymbol{\sigma} + \rho g; \tag{2.3}$$

where we introduce pressure as p and the deviatoric component of the stress tensor as $\boldsymbol{\sigma}$. The only additional assumption made here is that the gravitational acceleration g is considered constant over the domain (mantle), which is a reasonable and common assumption even for Earth's mantle (Dziewonski & Anderson, 1981).

Conservation of Energy

In addition to mass and momentum conservation, the equation for the conservation of energy must also be solved. However, as opposed to mass that stays constant over time, we must include both source and sink terms in our energy balance. An energy sink is represented by the heat loss to space through the planetary surface, while energy sources are given by the heat produced by the decay of radiogenic isotopes and the heat input from the core. Under these conditions, we can write the conservation of energy as:

$$\rho \frac{\mathrm{D}e}{\mathrm{D}t} = -\nabla \cdot \boldsymbol{H} - p \nabla \boldsymbol{u} + \nabla(\boldsymbol{\sigma} \cdot \boldsymbol{u}) + \rho Q; \tag{2.4}$$

where e represents the internal specific energy, $\boldsymbol{H}$ the heat flux and Q is the heat production due to radioactive decay. Here we assume only conductive heat transport for the heat flux $\boldsymbol{H}$ at the surface

of the planet, thus it can be re-written using Fourier's law of thermal conduction:

$$\boldsymbol{H} = -k\nabla T; \tag{2.5}$$

where k is the thermal conductivity and ∇T is the temperature gradient. Equation 2.5 can be used in order to simplify the conservation of energy formulation, coupled with the following equations of state:

$$e = c_V T; \tag{2.6}$$

$$\rho = \rho_0 + \left.\frac{\partial \rho}{\partial p}\right|_T \Delta p + \left.\frac{\partial \rho}{\partial T}\right|_p \Delta T + \ldots; \tag{2.7}$$

where c_V is specific heat capacity at constant volume. In order to simplify equation 2.7, using the definitions of thermal expansion coefficient (α), isothermal compressibility (β) and truncating at the first order terms, we can rewrite it as:

$$\rho \approx \rho_0(1 - \alpha\Delta T + \beta\Delta p). \tag{2.8}$$

Full system of Conservation Equations (dimensional)

The full system of conservation equations in their dimensional form can therefore be summarized as follows:

$$\nabla \cdot \boldsymbol{u} = 0; \tag{2.9}$$

$$\rho\frac{\mathrm{D}\boldsymbol{u}}{\mathrm{D}t} = -\nabla p + \nabla \cdot \boldsymbol{\sigma} + \rho g; \tag{2.10}$$

$$c_V\rho\frac{\mathrm{D}T}{\mathrm{D}t} = \nabla \cdot (k\nabla T) - p\nabla \boldsymbol{u} + \boldsymbol{\sigma}(\nabla \boldsymbol{u}) + \rho Q; \tag{2.11}$$

$$\rho = \rho_0(1 - \alpha\Delta T + \beta\Delta p). \tag{2.12}$$

This set of conservation equations can be further simplified by introducing specific assumptions depending on the problem that is addressed. Moreover, in order to solve these equations numerically, appropriate parameter scaling (i.e., non-dimensionalization) and boundary conditions need to be employed. In the following paragraphs we will briefly describe the specific assumptions, non-dimensionalization of parameters, and boundary conditions applicable to planetary thermal evolution modelling.

Extended Boussinesq Approximation

The typical simplifying assumption used to model mantle flows is often referred to as the Boussinesq approximation. This approximation neglects density variations apart from the buoyancy term (ρg term in the momentum equation Eq. 2.3). With this approximation, we consider $\rho = \rho_0$ except in the term ρg, that essentially drives convection (buoyancy term). Similarly, all other material parameters are assumed constant in the mantle, with the exception of viscosity, as will be described in section 2.3.1. Moreover, assuming an incompressible mantle, the pressure-dependent term in equation 2.8 can also be neglected. Lastly, internal frictions in the fluid element (i.e. $\boldsymbol{\sigma}(\nabla \boldsymbol{u})$) are not considered.

When dealing with large planetary mantles (e.g., Earth, Venus or larger terrestrial bodies), the effects of compressibility may not be entirely negligible. Heating due to large pressure increases (order of hundreds GPa) will be important and, therefore, assuming a purely Boussinesq flow may lead to large errors. In order to loosen the tightness of the assumptions, an Extended Boussinesq Approximation (EBA) is usually considered. In this case, the adiabatic heating and cooling and the viscous dissipation terms are kept in equation 2.18, while the density remains constant apart from the buoyancy term. The Extended Boussinesq approximation has been used throughout the present work, and its application is shown in the final system of equations (Eq. 2.17-2.19).

Non-dimensionalization

Non-dimensionalizing the governing equation has a number of advantages. Firstly, it helps understanding the relative importance of the different terms used in the conservation equations. Secondly, it largely reduces the amount of parameters to be computed, lumping them into characteristic non-dimensional quantities such as the Rayleigh number, which describes the system in terms of convective vigor. This improves code readability and makes the input file less error-prone. Lastly, it improves the efficiency and numerical stability of the solution of the linear system of equations, since most quantities will lie in a 0 to 1 range.

Non-dimensionalization means to divide a dimensional quantity by a scaling factor, usually representative of a property of the domain or out of convention, sharing the same physical units of the target variable. Thus, if the scaling parameters (reference quantities) are appropriately chosen, all variables used will be dimensionless and roughly in the range 0 to 1. This is important for the numerical solvers, as multiplying large and small dimensional numbers may result in round-off errors.

In the following list, we will briefly describe the relations used to non-dimensionalize the main quantities involved. The apostrophe ($'$) will denote dimensionless quantities, while the subscript r will stand for reference parameter:

Quantity	**Non-dimensionalization**
Length	$\boldsymbol{x'} = \frac{\boldsymbol{x}}{D}$
Time	$t' = \frac{\kappa_r}{D^2} t$
Velocity	$\boldsymbol{u'} = \frac{D}{\kappa_r} \boldsymbol{u}$
Pressure	$p' = \frac{D^2}{\eta_r \kappa_r} p$
Temperature	$T' = \frac{T}{\Delta T} - T_0$
Heat production rate	$H' = \frac{D^2}{\kappa_r c_p \Delta T} H$
Viscosity	$\eta' = \frac{\eta}{\eta_r}$
Density	$\rho' = \frac{\rho}{\rho_r}$
Thermal Conductivity	$k' = \frac{k}{k_r}$
Thermal expansion coefficient	$\alpha' = \frac{\alpha}{\alpha_r}$
Pressure Specific Heat Capacity	$c'_P = \frac{c_P}{c_{Pr}}$

Table 2.1: Non-dimensionalization relations of main physical quantities involved. The apostrophe ($'$) indicates non-dimensional quantities and subscript r refers to the reference (scaling) parameters.

In Table 2.1, the only quantity that is treated differently is the temperature (T), which is not only scaled (with ΔT corresponding to a T_r) but also shifted so that the zero value corresponds to a specific temperature (T_0) within the domain, usually the surface temperature. Moreover, we denote the reference length as D, which usually corresponds to the thickness of the layer of interest (mantle + crust). Using the relations in table 2.1, we can rewrite the system of conservation equations in a more concise form, as follows:

$$\nabla' \cdot \boldsymbol{u}' = 0; \tag{2.13}$$

$$\frac{1}{\mathrm{Pr}} \frac{\mathrm{D}\boldsymbol{u}'}{\mathrm{D}t'} = -\nabla p' + \nabla' \cdot \left[\eta' \left(\nabla \boldsymbol{u'} + (\nabla \boldsymbol{u'})^T\right)\right] + RaT' \hat{\boldsymbol{e}}_{\boldsymbol{z}}; \tag{2.14}$$

$$\frac{\mathrm{D}T'}{\mathrm{D}t'} = \nabla' \cdot (k' \nabla T') + D_i (T' + T_0) \boldsymbol{u}'_{\boldsymbol{r}} + \frac{Di}{Ra} \boldsymbol{\Phi} + \frac{Ra_Q}{Ra}; \tag{2.15}$$

where $\hat{e}_{\boldsymbol{z}}$ is the unit vector corresponding to the direction of the gravitational acceleration, η represents viscosity, $\boldsymbol{u_r}$ is the radial component of velocity, and Φ represents viscous dissipation. Viscous dissipation can be further expressed as: $\boldsymbol{\Phi} = \boldsymbol{\sigma} : \dot{\boldsymbol{\epsilon}}/2$, where $\dot{\boldsymbol{\epsilon}}$ is the strain rate tensor. Moreover, all scaling

parameters are collected in four non-dimensional numbers: Rayleigh number (Ra), heat production Rayleigh number (Ra_Q), Prandtl number (Pr), and the dissipation number (Di). The Rayleigh number (Ra) is used to describe the vigor of convection in a bottom-heated domain (high Ra corresponds to vigorous convection). The heat production Rayleigh number (Ra_Q) represents the vigor of convection in an internally heated domain. Lastly, the Prandtl number (Pr) represents the relative importance of momentum diffusivity to thermal diffusivity. These numbers can be formulated as:

$$Ra = \frac{\rho_r g_0 \alpha_r \Delta T D^3}{\kappa_r \eta_r}; \quad Ra_H = \frac{\rho_r^2 g_0 \alpha_r H D^5}{k_r \kappa_r \eta_r}; \quad \mathrm{Pr} = \frac{\eta_r}{\kappa_r \rho_r}; Di = \frac{\alpha_r g_0 D}{c_{Pr}}. \tag{2.16}$$

In the case of planetary mantles, viscosity can attain values between 10^{18} to 10^{38} Pa s, many orders of magnitude more than $\kappa_0 \rho_0$, meaning that the inverse of the Prandtl number can be effectively treated as zero. This implies that the LHS of equation 2.14 can be neglected, which is the mathematical realization of the concept of a fluid with negligible inertia. In this case, material flows only when a non-zero forcing is present, but would cease to move instantaneously if the acting forces were lifted. In other words, the fluid retains no memory of past forcing. This formulation of the momentum conservation equation is usually referred to as Stokes flow or creeping flow. The final system that will be solved numerically, thus, becomes:

$$\nabla' \cdot \boldsymbol{u}' = 0; \tag{2.17}$$

$$\nabla' \cdot \left[\eta' \left(\nabla \boldsymbol{u}' + (\nabla \boldsymbol{u}')^T\right)\right] + Ra T' \hat{\boldsymbol{e}}_{\boldsymbol{z}} - \nabla p' = \mathbf{0}; \tag{2.18}$$

$$\frac{\mathrm{D}T'}{\mathrm{D}t'} - \nabla' \cdot (k' \nabla T') - D_i (T' + T_0) \boldsymbol{u}'_{\boldsymbol{r}} - \frac{Di}{Ra} \boldsymbol{\Phi} - \frac{Ra_Q}{Ra} = 0; \tag{2.19}$$

Rayleigh Number

In a planetary mantle, the competition between viscous forces and thermal buoyancy determines the ability to convect, and can be mathematically expressed by the non-dimensional Rayleigh number (Ra), as just described:

$$Ra = \frac{\rho g \alpha \Delta T D^3}{\kappa \eta}; \tag{2.20}$$

where ρ represents the density, g is the gravitational acceleration, α is the thermal expansivity, ΔT is the temperature contrast between the hot and cold boundaries of the layer of interest, D is the layer thickness, κ is the thermal diffusivity, and η is the viscosity. This number can be interpreted as the relative importance between parameters driving and those resisting convection. A high Rayleigh number would thus be reflecting a vigorously convecting system, whereas a small Rayleigh number would indicate sluggish or event absent convection. A mantle will become gravitationally unstable, marking the onset of solid state convection, after a certain threshold or critical Rayleigh number (Ra_{cr}) is reached. The threshold value varies depending on the system properties and the wavelength of the initial perturbation, and is usually in the order of ~10^3 (Tosi et al., 2014). For typical lunar values: mantle thicknes of 1350 km, 1750 K of ΔT, thermal expansivity and diffusivity of 2·10^{-5} 1/K and 9·10^{-7} m^2/s, mantle density of 3400 kg/m^3, surface gravitational acceleration of 1.62 m/s^2 and dry olivine viscosity (10^{21} Pa s), the Rayleigh number attains a value of ~50000, indicating that lunar mantle can sustain convection.

Boundary Conditions

When solving the field equations, a set of boundary conditions is needed. Here, we briefly describe a common set of boundary conditions used for simulating full 3D mantle convection. Firstly, as mentioned with respect to Table 2.1, the non-dimensional surface temperature is usually taken as the lower bound of the temperature range ($T'_{surf} = 0$). Thus, the surface temperature, which is constant in time, represents the boundary condition, for the outer edge of the domain.

Conversely, the core-mantle boundary (CMB) temperature represents the maximum of the temperature scale ($T'_{CMB} = 1$). The temperature at CMB can be assumed constant throughout the evolution or, considering for instance core-cooling through time, it can be computed as a t-dependent function

($T'_{CMB} = T'_{CMB}(t)$). A simple and commonly used core-cooling function (Steinbach & Yuen, 1994; Stevenson et al., 1983), consisting of a one-dimensional energy balance between mantle and core, can be written as:

$$c_c \rho_c V_c \frac{\mathrm{d}T_{\mathrm{CMB}}}{\mathrm{d}t} = -q_{CMB} A_{CMB}; \tag{2.21}$$

where the subscript c denotes core quantities, V is the volume, q_{CMB} represents heat flux at core mantle boundary and A_{CMB} is the corresponding area. Equation 2.21 is formulated under the assumption of an adiabatic core with constant heat capacity and density (Steinbach & Yuen, 1994; Stevenson et al., 1983).

Lastly, in order to ensure mass conservation, all domain boundaries must be impermeable to the flowing material. This condition is set by the relation:

$$\mathbf{u}_{wall} \cdot \mathbf{n} = 0; \tag{2.22}$$

where **n** is the vector normal to the surface of the domain boundary. This condition represents the concept that the velocity component perpendicular to the domain boundary is equal to zero at any boundary point, meaning that no material leaves the domain. Conversely, tangential velocity components can be non-zero, allowing flow along the domain boundaries. This last boundary condition is referred to as free-slip condition.

2.2. Gaia Solver

The main software tool employed in this work is the Gaia fluid solver (Hüttig & Stemmer, 2008b; Hüttig et al., 2013; Plesa et al., 2016), developed and maintained at DLR - Institute of Planetary Research. Gaia is a finite-volumes numerical solver that uses fixed mesh in arbitrary geometries. The code is optimized to solve Stokes-flow with large spatial variations in viscosity (tens of orders of magnitude), appropriate for simulating planetary mantle convection.

Gaia is written in library-independend C++, it employs finite-volume method to discretize the governing equations (2.17-2.19) on grids of arbitrary geometry, as long as they are Voronoi grids (Hüttig & Stemmer, 2008a; Plesa, 2011). This means that it is always possible to generate poligonal grid cells such that two adjacent nodes are equidistant from the cell side between them, for every node in the grid. Typical grid geometries used in Gaia are: 2D and 3D cartesian box, 2D cylinder, 3D spherical shell, 3D sphere, 2D spherical annulus (Plesa et al., 2016). For the present study, we used a 3D sherical shell geometry, with radially aligned grid nodes.

The temporal discretization is treated with a fully implicit second order scheme. The user can then choose between a flexible time-step, fulfilling the Courant-Friederichs-Lewy, or a fixed time-step. The former method has been used consistently throughout this study.

Gaia simultaneously solves the velocity and pressure field, including the velocity components (u_x, u_y, u_z) and pressure p in a single system of equations. A selective Jacobi preconditioner is applied to the velocity part of the system's matrix, for more information the reader is referred to Hüttig et al. (2013). The software brings multiple iterative solvers that the user can choose from: BiCGS, BiCGS(l), Jacobi, and TFQMR, with the BiCGS(4) method being the most common choice for typical mantle convection scenarios (Plesa et al., 2016). The BiCGS(4) method has been used throughout this work.

For large-scale simulations, such as those performed in the present study (~3 million nodes), we employ parallel computing or, in other words, a Message Passing Interface (MPI). This method consists in the efficient decomposition of the domain in into multiple equal volumes, each being mapped to one computational core. In order to allow for data exchange between processors, Gaia uses so called halo-cells, or ghost-cells, which are additional cells surrounding each volume and forming an overlapping area shared between volumes. Each sub-domain has a halo-cell border that corresponds to active cells in the neighboring sub-domain. Effective domain decomposition in 3D spherical geometries is

ensured through a Thompson-points based method, or Thompson problem (Thomson, 1904). For this work, we use the parallelized version of Gaia on the DLR CARO high performance computer centre.

2.3. Material Properties

In the following sections, we will provide a detailed description of some key material properties and their treatment in the context of this work. In particular, we will focus on the properties that are most relevant in the study of planetary evolution, along with their treatment from a numerical modeling perspective. In addition, we will briefly describe the more general implication and concepts that arise from the study of these quantities and their effect.

2.3.1. Rheology and Viscosity

In general, rheology is a branch of physics that deals with how materials flow, mostly liquids and gases, but also solids under specific conditions. Within the field of geodynamics, the term rheology is used to indicate the physical behaviour (flow) of materials under different applied stresses and at different timescales. When studying mantle rocks, the timescale of forcing and subsequent deformation is of paramount importance. At high frequency, that is, forcing periods in the order of minutes to hours (e.g. earthquakes, impacts, etc...), the mantle responds almost elastically. An elastic response, which intuitively can be associated with a rubber-like behaviour, is characterised by the absence of permanent deformations with respect to the initial state. Conversely, at very low frequency (forcing period larger than 1000 years) and sufficiently high pressure and temperature, planetary mantles flow like viscous fluids, almost entirely plastically.

Unfortunately, conditions for planetary mantle flow are difficult to reproduce in laboratory experiments, leaving the field subject to extrapolation approaches. However, it is known that the main role in influencing mantle flow is played by temperature, pressure, stress, grain size, and composition (Breuer & Moore, 2015). As mentioned above, the physical quantity used to represent rheology is the viscosity (η), which describes the ability of rocks to deform under applied stresses, considering factors such as pressure, temperature, rock composition, and deviatoric stresses (i.e. higher viscosity means less dislocation for the same applied stress, and vice-versa).

Therefore, the mathematical formulation of viscosity must include its dependency on temperature, pressure, stress, grain size, and composition, in order to lump all material properties that affect rheology into the viscosity parameter. Viscosity can be defined as the proportionality factor relating stress and strain rate: $\tau = 2\eta\dot{\epsilon}$; where the strain rate $\dot{\epsilon}$ can be expressed as (Tosi et al., 2014):

$$\dot{\epsilon} = A\tau^n \exp\left(-\frac{E + V_a p}{RT_m}\right); \tag{2.23}$$

where A is an experimentally determined prefactor, T_m is the mean convective fluid temperature, R the universal gas constant, E the activation energy, V_a the activation volume, and p the pressure, making the numerator of the exponential an activation enthalpy ($H_a = E + V_a p$). In particular, E is the energy necessary to form vacancies that atoms can fill by flowing, plus the energy barrier that must be overcome for the atom migration to happen (Tosi et al., 2014). The term $V_a p$ represent the tendency of pressure to hinder these processes, increasing the total necessary enthalpy.

The parameter usually referred to as the stress exponent (n) represents the mode of creeping flow at play. There are two main flowing modes in planetary mantles: *diffusion creep*, which usually dominates at lower stresses (Tosi et al., 2014), in which case the solid behaves as a Newtonian fluid, meaning that viscosity does not depend on shear stresses ($n = 1$). Conversely, in *dislocation creep*, the solid flows as a non-Newtonian fluid, where viscosity is also a function of shear stress ($n > 1$). The value of prefactor A not only depends on the material but also on the deformation type (diffusion vs. dislocation creep). Combining the definition of viscosity with Equation 2.23, we obtain a general formulation of viscosity (Tosi et al., 2014):

$$\eta = \frac{1}{2} A^{-1/n} \dot{\epsilon}^{(1-n)/n} \exp\left(\frac{E + V_a p}{nRT_m}\right). \tag{2.24}$$

The extent to which diffusion and dislocation creep modes contribute to mantle flow at different conditions (pressure and temperature) is unclear, even for Earth. Laboratory experiments indicate that dislocation creep dominates at low pressures (upper mantle), while diffusion creep drives lower mantle deformation (Schubert et al., 2001). However, this simplifying assumption is inconsistent with the study of post-glacial rebound, which indicates diffusion creep even for upper mantle (Breuer, 2009). Assuming a purely Newtonian flow, equation 2.24 can be simplified as follows:

$$\eta = \eta_0 \exp\left(\frac{E + V_\mathrm{a} p}{R T_m}\right); \tag{2.25}$$

where $\dot{\epsilon}$ has disappeared, and all remaining material parameters have been lumped in the prefactor η_0. Let us know focus briefly on the relation between temperature and viscosity, which is pivotal in the understanding of mantle dynamics. The inverse exponential relation of these two quantities acts as a thermostat that controls the cooling behavior of the mantle. In other words, whenever the mean temperature increases, there is a significant reduction in viscosity, which in turn increases the convective vigor and, thus, the efficiency of outward heat transport, leading to pronounced cooling of the interior. Conversely, cold temperature would result in a high viscosity, leading to less vigorous mantle convection and reducing heat transport towards the surface. This effectively causes the temperature to increase.

This feedback effect has many interesting implications for planetary evolution: on the one hand, it makes the final thermal state almost independent of the initial temperature profile, which is usually highly unconstrained. On the other hand, if one wants to gain information on the initial temperature profile, relating it to what we observe today may be particularly challenging.

In this paragraph, we will briefly list some reference values of the quantities within equation 2.24 valid for Earth and planetary mantles, as thoroughly reviewed and summarised in Breuer and Moore (2015), in order to give some insight in their order of magnitude. Planetary mantles can be very different in mineralogy and composition, although having formed from the same building blocks. However, the general rheology of silicate rocks seems to be dominated by olivine, which is thought to be a main component of most planetary mantles.

At reference temperature and pressure of 1600 K and 12 GPa, with 540 kJ mol^{-1} activation energy and 15 cm^3 activation volume, the viscosity of dry olivine is ~10^{21} Pa s (Breuer & Moore, 2015) . This reference viscosity value can largely vary with, for instance, the amount of iron and, indeed, it is about ten times lower for the iron-rich Martian mantle. Moreover, the presence of volatiles has a great influence on viscosity, while also being particularly complex to constrain. For example, water-saturated olivine (referred to as wet olivine), has a viscosity 2 to 3 orders of magnitude lower than dry olivine (Breuer & Moore, 2015).

2.3.2. Heat Sources

As was discussed in this chapter, temperature contrasts between a planet's interior and its surface are the main drivers of mantle dynamics, enabling the slow creeping flow of rocks over geological timescales. In this chapter, we will discuss the internal sources that supply the energy necessary to power not only convection, but also other processes such as volcanism and magnetic field generation. Firstly, we will briefly describe the processes that provided energy to the solar system bodies in their first few million years of evolution (i.e. Accretional Heating and Core Formation, Breuer and Moore, 2015). Thereafter, a discussion of Tidal Dissipation and Radioactive Heat Sources will be provided. These last two sources can continuously supply energy throughout the evolution of a planetary body, making their modeling particularly relevant to this work. Thus, we will give a more detailed description of radiogenic heating and how it is treated in numerical models, as this is the main source of energy throughout lunar evolution.

Accretional Heating

Accretional heating can be considered one of the largest energy sources for a planet (Breuer & Moore, 2015). During the accretion process, impactors of various sizes and velocity collide with the young planetesimals, burying most of their mechanical energy in the interior of the accreting bodies. During

this process, a planet develops an initial temperature profile, with very high temperatures throughout the interior (e.g. about 2000 K for a Mars-sized body, Breuer and Moore, 2015) and high temperature differences across the thermal boundary layer in the top-most few hundred kilometers (order of hundreds of kelvin).

Depending on the size of the accreting body, its composition, and the amount of heat stored (i.e. not re-radiated to space), the accretion temperature profile can rise above the melting temperature of metals and silicates, even close to the surface. In this case, as we briefly mentioned for the Moon in section 1.2, a partial or global magma ocean can form. However, the accretion temperature distribution may also be influenced by the degree of differentiation of the planetesimals or, for rapidly forming bodies, by the decay of very short-lived radiogenic isotopes such as ^{26}Al.

Core Formation

In principle, planets are thought to form as an undifferentiated mixture of metals and silicates, but evolve to concentrate heavier elements (metals) at their center, in an iron-rich core, and leave lighter silicates in a rocky mantle above. However, the timing of this process remains partly unclear, some studies argue that differentiation can be contemporaneous with accretion, while others provide ranges between 0.5 and 1 Ga for its completion (Breuer & Moore, 2015).

For a rotating spheroid, a differentiated configuration is more gravitationally stable than an undifferentiated one. This means that when iron (and other heavier elements) sink towards the center, gravitational energy is released and converted to heat by viscous dissipation, which efficiently raises the interior temperature. The total energy supplied by the differentiation of a homogeneous body into a fully differentiated 2-layer planet can be estimated as the difference in potential energy between the two configurations (Schubert et al., 1986).

Assuming thermal equilibrium between core and mantle, that is, assuming an homogeneous distribution of energy, this simple calculation yields a mean temperature of 1000 K for Earth and 300 K for Mars. However, the thermal equilibrium assumption may not hold for a rapidly formed core (Breuer & Moore, 2015). In this case the core would be superheated with respect to the mantle, depending on the planet rheology and segregation mechanics, which can have important implications on the magnetic field generation.

Tidal Dissipation

Another important energy source is the tidal interaction between a planet and its host star, or between a planet and its satellites. For satellites or planets moving in elliptical orbits, the gravitational attraction varies periodically. If the interior of a body reacts viscoelastically to this periodic forcing, deforming and returning to its initial configuration in an oscillatory manner, tidal energy can be dissipated as heat.

In some peculiar cases, tidal heating can be particularly large (e.g. Galilean moons and mainly Io), and even exceed the energy released by radioactive decay. The rate at which tidal energy is dissipated depends on the time variation of the tides, the interior structure, and rheology (i.e. mainly the temperature) of the dissipating body (Breuer & Moore, 2015). This concept has important implications for the thermal evolution of planetary bodies, coupling it with the rotational and orbital dynamics of the host system through the dissipation rate.

Considering the case of the Earth-Moon system, the influence of tidal heating is thought to have played a role in the early stages of the system's evolution (Breuer & Moore, 2015).

Radioactive Heat Sources

Accretional heating and core formation are processes that provide vast amounts of energy, but mainly during the early history of the solar system. Tidal dissipation does not have similar constraints, being able to generate heat continuously, but only under very specific orbital and rotational dynamics of the dissipating body. Considering for example the Earth-Moon system, all of the processes above can not be responsible for tectonics or magmatism after the first few hundred million years of evolution (Breuer

& Moore, 2015).

Instead, long-lived radioactive elements, mainly ^{238}U, ^{235}U, ^{232}Th and ^{40}K, with half-lives of the order of billion of years, become the predominant source of energy during subsequent evolution. This is particularly important for the modeling of planetary thermal evolution; energy sources that quickly stop to significantly contribute to the energy budget can be lumped up to constitute the initial conditions of the model. In addition, as was briefly mentioned above and as we will demonstrate later in the study, perturbations in the initial conditions of a thermal evolution model (even if large), only play a relatively small role for the present-day state.

Radiogenic heat production, and, most importantly, the distribution of radioactive heat sources during the evolution has a pivotal role in the current state of a body (e.g. on the Moon, Siegler and Smrekar, 2014). Similarly, in the case of Earth, radiogenic heat production powers volcanism and convection, with roughly half of Earth's thermal output being due to the radioactive decay (Breuer & Moore, 2015). The rest comes from the process of secular cooling, that is, the slow loss of formation energy that all planets undergo. The ratio between these two components of a planet's heat output is referred to as Urey ratio.

From a mathematical perspective, the total heat production rate Q_0 at present-day can be computed from the individual heat generation rates of each radioactive isotope, using the following relation (Breuer, 2009):

$$Q_0 = C_0^U \left(Q^U + \frac{C_0^{Th}}{C_0^U} Q^{Th} + \frac{C_0^K}{C_0^U} Q^K \right); \tag{2.26}$$

and the mean heat production rate as a function of time $Q(t)$, can be similarly computed as:

$$\begin{aligned} Q = {} & 0.9928 C_0^U Q^{U^{238}} \exp\left(\frac{t \ln 2}{\tau_{1/2}^{U8}} \right) \\ & + 0.0071 C_0^U Q^{U^{235}} \exp\left(\frac{t \ln 2}{\tau_{1/2}^{U^{235}}} \right) \\ & + C_0^{Th} Q^{Th} \exp\left(\frac{t \ln 2}{\tau_{1/2}^{Th}} \right) \\ & + 1.19 \cdot 10^{-4} C_0^K Q^{K^{40}} \exp\left(\frac{t \ln 2}{\tau_{1/2}^{K^{40}}} \right); \end{aligned} \tag{2.27}$$

where Q indicates the heat production rate, C represents the concentration, and τ stands for the half-life time. The numerical values needed to compute the above quantities are listed in table 2.2

Isotope	**Specific heat production rate** Q [W kg^{-1}]	**Half-life of the isotope** $\tau_{1/2}$ [year]
^{238}U	9.46×10^{-5}	4.47×10^{9}
^{235}U	5.69×10^{-4}	7.04×10^{8}
U	9.81×10^{-5}	
^{232}Th	2.64×10^{-5}	1.40×10^{10}
^{40}K	2.92×10^{-5}	1.25×10^{9}
K	3.48×10^{-9}	

Table 2.2: Specific heat production rates and half-lives of various isotopes (Breuer, 2009).

Looking at Table 2.2, it may be noted how the half-lives of the different isotopes vary significantly (roughly three orders of magnitude range). This means that the decay of each isotope will have a

different effect on the thermal evolution of a terrestrial planet. Another way to more intuitively visualize this is plotting the heat production rate of each isotope separately through time (Figure 2.2)

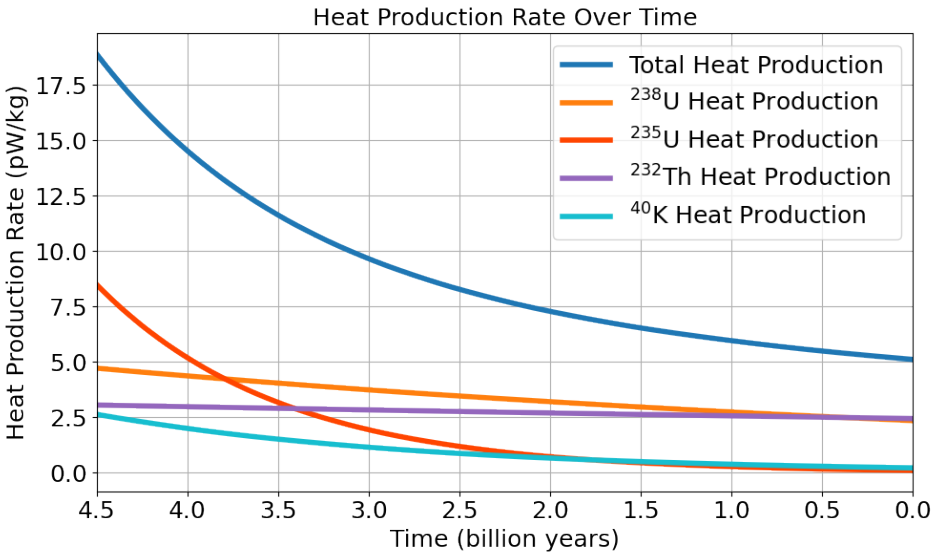

Figure 2.2: Heat production rate of different radioactive isotopes as a function of time. Concentrations are typical values for the Moon, taken from Laneuville et al. (2013), with BSM uranium concentration of 25 ppb, thorium to uranium ratio of 3.7 and potassium to uranium ratio of 2500.

From Figure 2.2, it becomes clear how ^{235}U and ^{40}K play a much bigger role during the first 1 to 1.5 billion years of evolution, having the smallest half-lives. Conversely, ^{238}U and ^{232}Th maintain their heat production rates almost constant through time, meaning that heating from the decay of these two isotopes likely continues to power mantle heating at present-day.

2.4. Crustal Structure

The crust of a planet has a crucial role in its thermal evolution. Firstly, not only does it record the amount of differentiation that a body experienced, but in some cases also the timing of magma ocean crystallization (e.g. on the Moon). Moreover, due to the difference in density and material properties between crust and mantle (crust is lighter, less thermally conductive, more viscous), the crustal layer acts as an insulating blanket. It keeps mantle material warm, while also storing an important fraction of HPE (10 to 40% in our lunar models).

As was stated in section 1.5.3, the present work aims at constraining the effect of the structure and composition of the crust on the thermal evolution of the Moon. Variations in crustal thickness and thermal conductivity, along with the abundance and distribution of HPE, prominently affect the thermal state of the mantle (Siegler & Smrekar, 2014). Therefore, understanding the structure of the lunar crust is pivotal for this study. In particular, we combine our geodynamic models with two models related to crustal structure: a recently developed model of crustal thickness distribution (Broquet & Andrews-Hanna, 2024a), and a model of crustal porosity (Wahl et al., 2020). Both these models come from the analysis of gravity data from the GRAIL mission. In the following sections, we briefly summarize the theory behind the generation of these two datasets, focusing primarily on gaining a general understanding of them, which is important for the interpretation of our results.

2.4.1. Crustal Thickness

When a spacecraft orbits a celestial body, it is accelerated when passing above a mass anomaly. Such anomaly can originate from the shape of the planet (e.g., crater or volcano) or from the interior structure, including variations in the relief of the crust-mantle interface. Therefore, the gravity field inherently contains information on the interior structure and shape of a planet, with a degree of degeneracy between possibly competing phenomena related to these two properties.

In order to estimate the crustal thickness of a planet, one needs to combine gravity and topography data. A first step is to correct the ”free-air” (i.e. raw) gravity field for the contribution coming from laterally variable shape of the planet (the so-called Bouguer correction) (Andrews-Hanna et al., 2014). The resulting dataset is referred to as Bouguer anomaly, and represents a residual gravity field which is not produced by topographic elevation (Figure 2.3). What remains is representative of the interior structure of the body: negative gravity anomalies (areas in blue in Figure 2.3) correspond to a locally lower depth-wise amount of mass, while positive anomalies suggest the opposite (areas in red are positive mass anomalies).

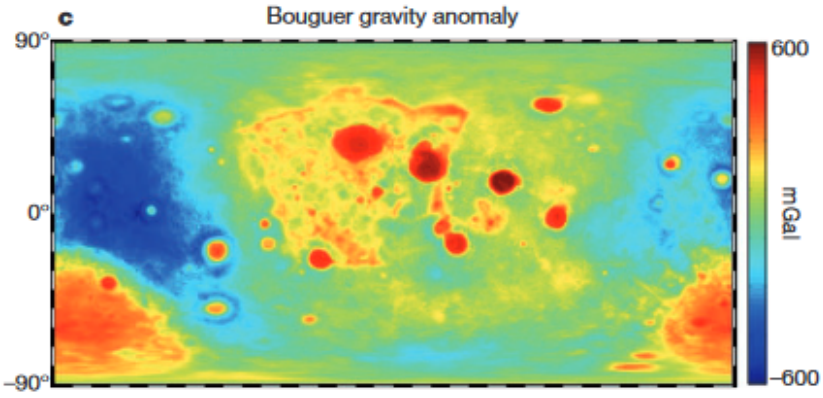

Figure 2.3: Simple cylindrical projection of Bouguer gravity anomaly from Andrews-Hanna et al. (2014).

After correcting the residual gravity for all other known contribution (e.g., mass estimates of basaltic mare eruptions on the Moon), one can assume that the residual gravity anomalies are due to the crustal thickness distribution. In other words, a positive gravity anomaly corresponds to mantle material (more dense and, thus, more massive) being closer to the surface (locally thin crust), while a negative anomaly suggest thicker crust. Thus, it is possible to invert Bouguer gravity anomalies for crustal thickness. Naturally, this system is highly degenerate, because laterally variable crustal density (due to e.g., magmatic intrusions, porosity and/or compositional variations), which are likely to exist, can also fit observations. Moreover, the planetary gravity field is mostly independent from the average crustal thickness, and this quantity can thus not be constrained using gravity and topography alone (Wieczorek et al., 2013).

For this reason, multiple crustal thickness models can be produced depending on the type of assumptions taken (i.e., on the average crustal thickness, density contrast between crust and mantle including spatial variations of this contrast). Seismic measurements, which reveal the subsurface structure of a planet, can provide valuable anchor points for crustal thickness models. In our case, we refer to the model by Broquet and Andrews-Hanna (2024a), in which the crust is divided in a feldspathic bottom layer overlain by basaltic mare wherever mare basalts are observed. The advantage of this model is the additional dataset related to the local thickness of mare basalts, which is put to use in the current study.

2.4.2. Crustal Porosity

Porosity is a crucial parameter for the estimation of the bulk properties of a material. In particular, it has a large effect on thermal conductivity, which we are interested in for the present study. A crustal layer characterized by high porosity rock conducts heat less efficiently than a non-porous layer, providing better thermal insulation to the underlying mantle. Similar to Siegler and Smrekar (2014), we aim at deriving lateral variations in crustal thermal conductivity by correlating it with corresponding variations in surface porosity estimated using gravity and porosity data (Wahl et al., 2020). It is possible to obtain information on the porosity of a planetary crust using topography-corrected gravity data, that is, the Bouguer anomaly. Porosity can be defined as a percentage value using the following formulation:

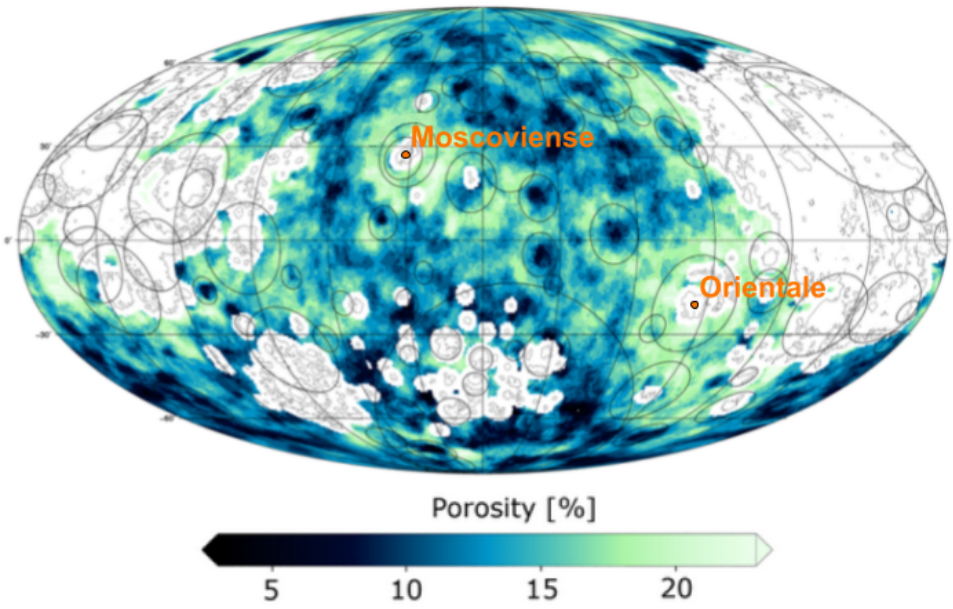

Figure 2.4: Percentage of porosity in the lunar upper crust adapted from Wahl et al. (2020). The map is shown using a Mollweide equal area projection, centered over the lunar farside at 180◦ E, 0◦ N. Impact basin main rims with diameters larger than 200 km are outlined by black circles and the mare, which were not considered, are outlined with thin black lines. Regions, where analyses were not performed are shown as white.

$$\phi = (1 - \frac{\rho_{\text{bulk}}}{\rho_{\text{grain}}}) \cdot 100 \tag{2.28}$$

where porosity ϕ is computed as the complement to one of the ratio between bulk density and grain density (which must be known independently). Inversion of topography and gravity data can provide estimates of lateral variations in the bulk density of the crust. Crustal thickness variations are typically related to longer-wavelength (>50 km) gravity anomalies, whereas smaller-scale anomalies are typically assumed to originate from crustal density variations (Jansen et al., 2017; Wahl et al., 2020). In Wahl et al. (2020), gravity is analyzed within small circular windows of 3 deg radius, which are moved across the surface, in order to generate a final bulk density grid with 0.75 deg grid-size (~22.5 km at the equator, Wahl and Oberst, 2019). Of the whole gravity field dataset, in the spherical harmonics domain, this method utilizes the information provided by the high-degree coefficients, corresponding to wavelengths comparable to the window size. This method is representative of the first few kilometers of crust (~4 km, Wahl and Oberst, 2019).

At this spatial resolution, the gravity field has much better correlation with topography data with respect to the global field, meaning that if the correct bulk density is guessed for a window, the resulting Bouguer anomaly would be zero. Thus, it is possible to infer bulk density by minimising the Bouguer gravity/topography correlation within a small-scale window and, by sliding the window across the surface, one produces a global bulk density map.

In regions where mare basalts cover the crust, the stratigraphic structure is much more complex, with denser lava sitting on top of a lighter feldspathic crust. To avoid loosing accuracy or bias the data due to the presence of basalts, mare-covered regions are left out of this method. Lastly, the grain density is taken from Huang and Wieczorek (2012), which converted lateral variation in the composition of lunar rocks measured by Lunar Prospector gamma ray spectrometer to grain density using a mineralogical norm. Porosity can then be estimated using equation 2.28, which yields global porosity maps similar to that in figure 2.4.

Part II

Manuscript

Present-day thermal state and surface heat flux of the Moon

Sabatino Santangelo[1,2], Ana-Catalina Plesa[1], Adrien Broquet[1], Doris Breuer[1], Bart Root[2]

[1]German Aerospace Center (DLR), Institute of Planetary Research, Rutherfordstr. 2, 12489 Berlin, Germany
[2]Delft University of Technology, Kluyverweg 1, 2629 HS Delft, The Netherlands

Key Points:

- Lunar thermal evolution
- Present-day surface Heat flux
- Abundance and distribution of Heat-Producing Elements
- Spatial crustal thickness distribution

Corresponding author: =name=, `=email address=`

Abstract

The surface heat flux provides important constraints on the present-day thermal state of the lunar interior. Measurements, performed in situ during the Apollo program, and from orbit at the Compton-Belkovich by Chang'E 1 and Region 5 by the Diviner radiometer instrument indicate important lateral variations in surface heat flux ($\sim$ 5 - 180 mW/m^2). This variability can be partly explained by the presence of an anomalous region, enriched in U, Th, and KREEP (Potassium, Rare Earth Elements and Phosphorus) elements, located on the lunar nearside. However, the detailed structure and properties of this KREEP layer have remained uncertain.

Here, we model the interior dynamics and thermal evolution of the Moon after magma ocean solidification using the fluid solver GAIA. We account for a spatially variable crustal thickness, derived from gravity and topography data. We vary the extent of the KREEP layer that underlies the PKT (Procellarum KREEP Terrane) region and consider higher heat producing elements abundances in the KREEP and crust compared to the mantle.

We find that measurably lower heat flux values at Region 5 compared to Apollo 15 and 17 require KREEP material to extend at least partly beneath mare Serenitatis, with thorium abundances below 3 ppm for a 30 km thick equivalent KREEP layer. In this case, the Apollo 15 measurement would be representative of the PKT average heat flux, while Apollo 17 would lie on its edge. On the other hand, a smaller KREEP region would make Region 5 and Apollo 17 representative of the same terrain (non-KREEP) and have the same heat flux. This is incompatible with Diviner measurements, although uncertainties associated with these measurements are unclear. Heat flux measurements that will be performed by the Farside Seismic Suite at Schrödinger crater will provide key information that would help to exclude one of these two scenarios, and thus potentially constrain the extent of the KREEP layer underneath PKT region.

Plain Language Summary

Observations of lunar surface features, along with measurements by various missions including Apollo, show striking differences between lunar near- and farside. The lunar nearside is characterized by large patches of dark volcanic material, which floods giant basins that formed about 4 billion years ago. In contrast, the farside is almost entirely devoid of volcanic material, appearing lighter in color and punctured by a much larger amount of small craters. In addition, subsurface temperature measurements and models suggest a concentration of radioactive material below the nearside surface, which increases the local temperatures in the subsurface. Understanding the reasons behind the lunar asymmetry and its present-day status is crucial to aid future lunar exploration and gain insight in the formation of planetary bodies.

The Moon formed in a molten magma ocean state, produced by the aftermath of a giant impact between early Earth and another proto-planet. Upon solidification and subsequent cooling, lunar material was distributed in three main layers: a metal core, a dense basaltic mantle and light anorthositic rock crust. During this process, the lunar asymmetry likely originated.

In this study, we use large-scale computer simulations of lunar interior dynamics (i.e. flow of rock under high pressure and temperature), to model the 4.5 billion year long cooling of the Moon. Throughout the simulation, we investigate the effect of the radioactive material asymmetry and spatial variations of the crust layer thickness on lunar evolution, aiming at better explaining present day observations. To do so, we test multiple configurations of these asymmetric properties, trying to match estimates of subsurface temperature collected by various space missions.

In contrast with what previously thought, we find evidence for the radiogenic material to be concentrated in a region up to 1500 km in diameter, but characterized by lower concentration of radioactive isotopes. In addition, our results show that the initial amount of radioactive material present on the newly formed Moon may be even lower than on Earth. Lastly, our model suggest that the concentration of radioactive material may also be spatially variable on the nearside, with a gradual decrease and non-circular shape across the lava flooded regions.

1 Introduction

High-resolution gravity field measurements from GRAIL, along with in-situ heat flux and seismic data from Apollo, surface composition data from Clementine and Lunar Prospector, and lunar sample analysis, have greatly enhanced our understanding of the Moon's thermal evolution (Zuber et al., 2013; Langseth et al., 1976; Garcia et al., 2019; McEwen & Robinson, 1997; Lawrence et al., 1999; Jaumann et al., 2012). Its asymmetric nature is particularly evident in the uneven distribution of thorium and volcanic basalts at present-day, predominantly observed on the nearside Procellarum KREEP Terrane (PKT), as opposed to Farside Highlands Terrane (FHT) and South-Pole Aitken basin (SPA) (Wang et al., 2016; Broquet & Andrews-Hanna, 2024b; Jolliff et al., 2000). Possible explanations including asymmetric crystallization of the lunar magma ocean (LMO), mantle overturn or differences in crustal thickness between near and farside have been proposed.

Heat flux measurements are key indicators of thermal state of the subsurface, serving as primary constraint for thermal evolution models. Available heat flux measurements and estimates can be summarized as follows: 18±3 mW/m^2 were measured at the Apollo 15 and 12±2 mW/m^2 at the Apollo 17 landing sites, a peak heat flux of ∼180 mW/m^2 was recently inferred from the Chang'E 1 and 2 data at the Compton-Belkovich location, and a lower bound for the lunar heat flux of only ∼6 mW/m^2 suggested, for the so-called Region 5, by LRO measurements (Warren & Rasmussen, 1987; Siegler et al., 2023; Paige & Siegler, 2016). Due to the lack of farside heat flux data and surprisingly high variability among nearside measurements and estimates, no agreement has yet been found towards a consistent model.

Previous modeling efforts, both on regional and local scale, tried to address the difference between the two Apollo datapoints (Siegler & Smrekar, 2014; Laneuville et al., 2013), and region 5 (Laneuville et al., 2018). Results of the regional-scale model by Siegler and Smrekar (2014) show that an asymmetric subsurface distribution of radiogenic isotopes, following the fractional crystallization of LMO, can explain the difference between the Apollo values, while crustal thickness variations have minor influence. Based on the Apollo values, this model further constrains the crust-mantle interface heat flux (7-13 mW/m^2) and global average heat flux (∼12 mW/m^2). However, the extent to which the Apollo values are representative of surface heat flow (whether local, regional or global) remained an open question in the above studies.

In this respect, the models proposed by Laneuville et al. (2013) provide crucial insight, suggesting an ongoing thermal anomaly caused by radiogenic enrichment (referred to as KREEP layer) in the PKT region. Furthermore, effects of a circular KREEP anomaly on the thermal evolution are addressed, resulting in long-standing nearside volcanic activity and magnetic field generation. Still, the axi-symmetric structure of these global models (centered on the KREEP anomaly) limits their ability to estimate surface heat fluxes across the different lunar terranes.

In this work, we build on the approach in Laneuville et al. (2013, 2018), but include both heterogeneous HPE (Heat Producing Elements) and crustal thickness distribution, coming from gravity and topography data (Broquet & Andrews-Hanna, 2024a). This is

the first study that combines a global scale geodynamic model with spatial variations of the lunar crust to evaluate their effect on the thermal state of the lunar interior during the evolution and at present-day. We test different KREEP layer configurations, to investigate the effects on present-day heat flux distribution. Plausible scenarios, selected based on the current heat flux constraints, are discussed together with strategies to exclude (or confirm) them with upcoming lunar missions.

Considering the lack of widespread heat flux data on the Moon, the main advantage of global modelling is the ability to address the spatial extent to which each measurement is representative, which is limited in regional models (Siegler & Smrekar, 2014). Moreover, global scale models can use available local heat flux estimates as anchor points to reconstruct a global heat flux distribution. By including a laterally variable crustal thickness we can perform direct comparisons between different lunar terranes, and test different KREEP configurations chosen based on the extent of the KREEP region.

2 Methods

We model the thermal evolution of the Moon in full 3D spherical geometry, using the mantle convection code Gaia (Hüttig & Stemmer, 2008a, 2008b; Hüttig et al., 2013). In particular, we solve the conservation equations of mass, linear momentum, and thermal energy, assuming purely Newtonian rheology and negligible inertial terms, due to the high viscosity of lunar mantle. Additionally, we consider adiabatic heating and cooling (i.e., extended Boussinesq approximation), core cooling, and decay of heat-producing elements (HPE).

In order to investigate its effects on lunar thermal evolution, we include a laterally variable crustal thickness distribution, which is fixed in time, as modelled from gravity and topography data by Broquet and Andrews-Hanna (2024a) (Figure 1a).

We vary input parameters such as the initial temperature profile, mantle reference viscosity, KREEP region size, KREEP distribution with depth, KREEP enrichment, crustal enrichment, and bulk abundance of HPE. All parameters are varied with respect to a reference model, which is similar to the 0LW model of Laneuville et al. (2013). More information about the governing equations and reference model setup can be found in Part I - Section 2, and a detailed list of reference model parameters can be found in supporting material S1. Similar to Laneuville et al. (2013), we use fixed Th/U and K/U ratios, equal to 3.7 and 2500, respectively. Our reference KREEP region is centered in Bray-ley crater (20°N, 35°O) and has radius of about 1200 km.

Given the different treatment of the crustal thickness, which is constant and equal to 40 km in (Laneuville et al., 2013), we adjust the crustal and KREEP enrichments to keep the relative concentrations unchanged with respect to Laneuville et al. (2013) (crust roughly 20 times and KREEP region 120 times more enriched than mantle). In Figure 1b, a sketch of our model, showing the homogeneous mantle overlain by a variable crust-mantle relief, and including the different amounts of heat sources between mantle, crust, and KREEP.

As shown in Figure 1b and analogous to the 0LW model of Laneuville et al. (2013), in our reference case the HPE enrichment in KREEP region is homogeneously distributed within the crust. Although it is more likely for the radiogenic enrichment to be found at the bottom of the crust or between crust and mantle, we make this choice in our benchmark model for a better comparison to the results in Laneuville et al. (2013), and to have a simpler initial setup. The effect of changing the depth of the KREEP enrichment is discussed in Section 3.

In this study, we also vary the geographical extent of the KREEP region, with a small KREEP case of ∼800 km radius, medium case (Reference) of ∼1200 km radius,

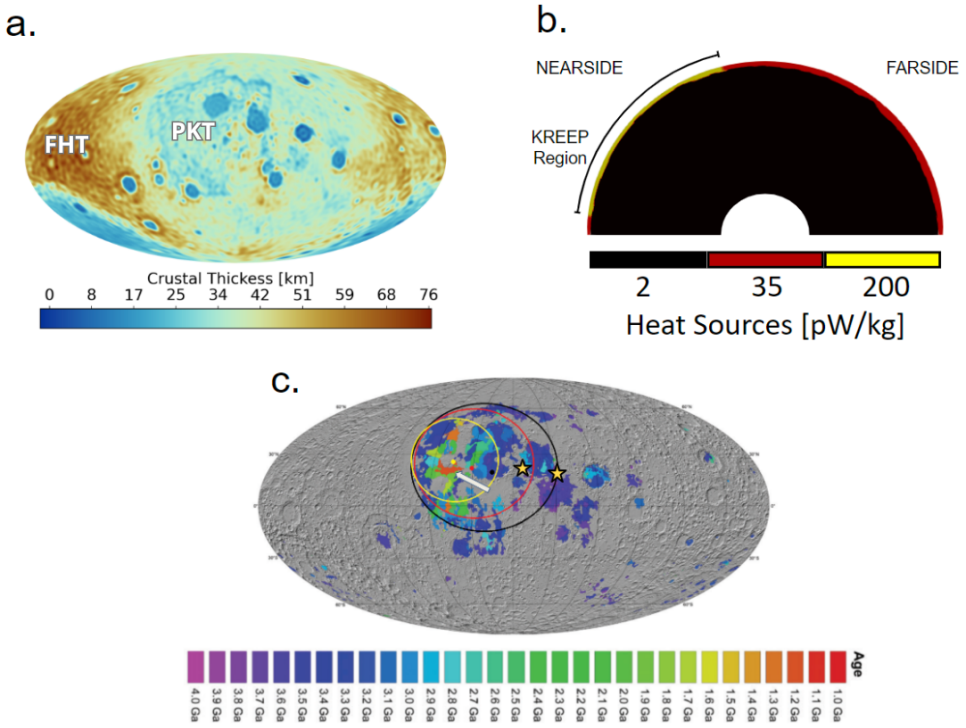

Figure 1. a) Crustal thickness distribution showing Procellarum KREEP Terrane (PKT) and Farside Highlands Terrane (FHT). b) Reference model heat sources distribution in the mantle, crust and KREEP. c) Chronology map of mare basalts, modified from Hiesinger et al. (2023). Differently coloured circles and dots represent the outlines and centers of different KREEP sizes tested here, while stars represent the landing sites of Apollo 15 and Apollo 17.

and large case of ∼1500 km radius (Figure 1c). However, in order to simulate a realistic KREEP region geometry for such different sizes, the centre point of the region must shift accordingly. This choice is based on two considerations: firstly, the youngest mare basalts, which record the most recent lunar eruptions, should always be within, if not centered on, the KREEP induced thermal anomaly (Laneuville et al., 2013; Hiesinger et al., 2023). Secondly, the geographical regions that can be considered as expressions of the KREEP anomaly are non-concentric. In particular, a large KREEP case (black circle in Figure 1c) best correlates with the thin-crust anomaly observable in Figure 1a. Our medium sized KREEP region (red circle in Figure 1c) is related to the thorium anomaly, similar to the model from Laneuville et al. (2013), which we use as benchmark. Lastly, the small KREEP case (yellow circle in Figure 1c) can only be centered on the youngest mare eruptions, in order to keep them within the high-temperature anomaly that most likely is their cause.

We use present-day surface heat flux as the main constrain for our models. In addition to the measured heat flux values listed in Section 1, we compute the surface average and crust-mantle interface heat flux within Imbrium-Serenitatis region. We directly compare these extra results to previous estimates by Warren and Rasmussen (1987) and Siegler and Smrekar (2014).

3 Results

In order to address the effect of a laterally variable crustal thickness on thermal evolution models, we construct three main models: a reference model, which includes a variable crustal thickness and a higher enrichment in HPE in the crust and KREEP compared to the mantle (panels b, e, and h in Figure 2), a model analogous to the 0LW model in (Laneuville et al., 2013), which has constant crustal thickness but KREEP and crust enrichment in HPE (panels a, d, and g in Figure 2), and a model that has no KREEP enrichment but includes laterally variable crustal thickness (panels c, f, and i in Figure 2).

Using the constant crustal thickness configuration, we are able to replicate the results of Laneuville et al. (2013). We find comparable convection planform in the interior, with three major upwellings almost equally spaced; the strongest being caused by the KREEP anomaly (Figure 2d). In terms of surface heat flux (Figure 2a), we also find values outside of the KREEP region of $\sim$11 mW/m^2, compatible with the Apollo 17 measurement (14 $\pm$ 2 mW/m^2).

In Laneuville et al. (2013), the Apollo 15 landing location falls well within the KREEP region and is representative of average KREEP region values. This is solely due to the choice of KREEP centre location or, in other words, the relative distance between KREEP centre and Apollo 15 landing site. Conversely, our choice of reference KREEP centre location (Brayley crater) causes the Apollo 15 landing site to be on the edge of the region. Thus, modeled heat flux values at Apollo 15 site are lower than average KREEP region values, which means that we need a slightly higher KREEP enrichment (1.22 ppm U instead of 0.82 ppm U used in Laneuville et al. (2013)) to fit the Apollo 15 measurement.

We find heat flux values of about 30 mW/m^2 at the KREEP region center (20°N, 35°O), compared to the 25 mW/m^2 found in Laneuville et al. (2013). We note that in the aforementioned study, similar to our constant crustal thickness case (Figure 2a), surface heat flux variability solely depends on the location with respect to the KREEP anomaly. Specifically, three surface heat flux outcomes are possible: within, on the edge, or outside the KREEP region ($\sim$30, $\sim$18, and $\sim$11 mW/m^2, respectively), which are represented by the thermal profiles in Figure 2g.

When looking at the case without KREEP enrichment (rightmost column in Figure 2), we see the effects of crustal thickness variation, without any KREEP enrichment. The asymmetrical thermal blanketing effect of the crust causes thin crust regions (e.g. nearside and SPA) to attain measurably lower heat flux with respect to the FHT (Farside Highlands Terrane) covered by a thicker crust (differences up to 5 mW/m^2). The effect of the crustal thickness asymmetry is particularly visible in the interior temperature distribution (Figure 2f), showing a colder nearside (thin crust), as opposed to a warmer farside (thick crust). Lastly, the hottest region in this case is related to the thickest lunar crust (FHT), which is reflected in the thermal profiles (Figure 2i).

In our reference case (central column in Figure 2), we see the combination of both effects, yielding slightly lower KREEP region heat flux ($\sim$30 mW/m^2) compared to the constant crustal thickness case, due to a thinner nearside crust than the model in panel a, and a larger heat flux variability (8-15 mW/m^2) for regions not affected by KREEP (SPA and FHT, respectively). The surface heat flux variability is caused by the asymmetrical blanketing effect of the crust, which causes positive thermal anomalies to propagate in the topmost layers even below the farside (Figure 2e), as opposed to a perfectly symmetrical blanketing (Figure 2d). We also observe more diverse thermal profiles at the locations of interest (Figure 2h), with mantle below FHT being warmer than that of the two Apollo sites and closer to that of the KREEP region.

The input parameters that have the biggest effect on present-day surface heat flux are: KREEP region size and radiogenic enrichment, Bulk Silicate Moon (BSM) HPE abun-

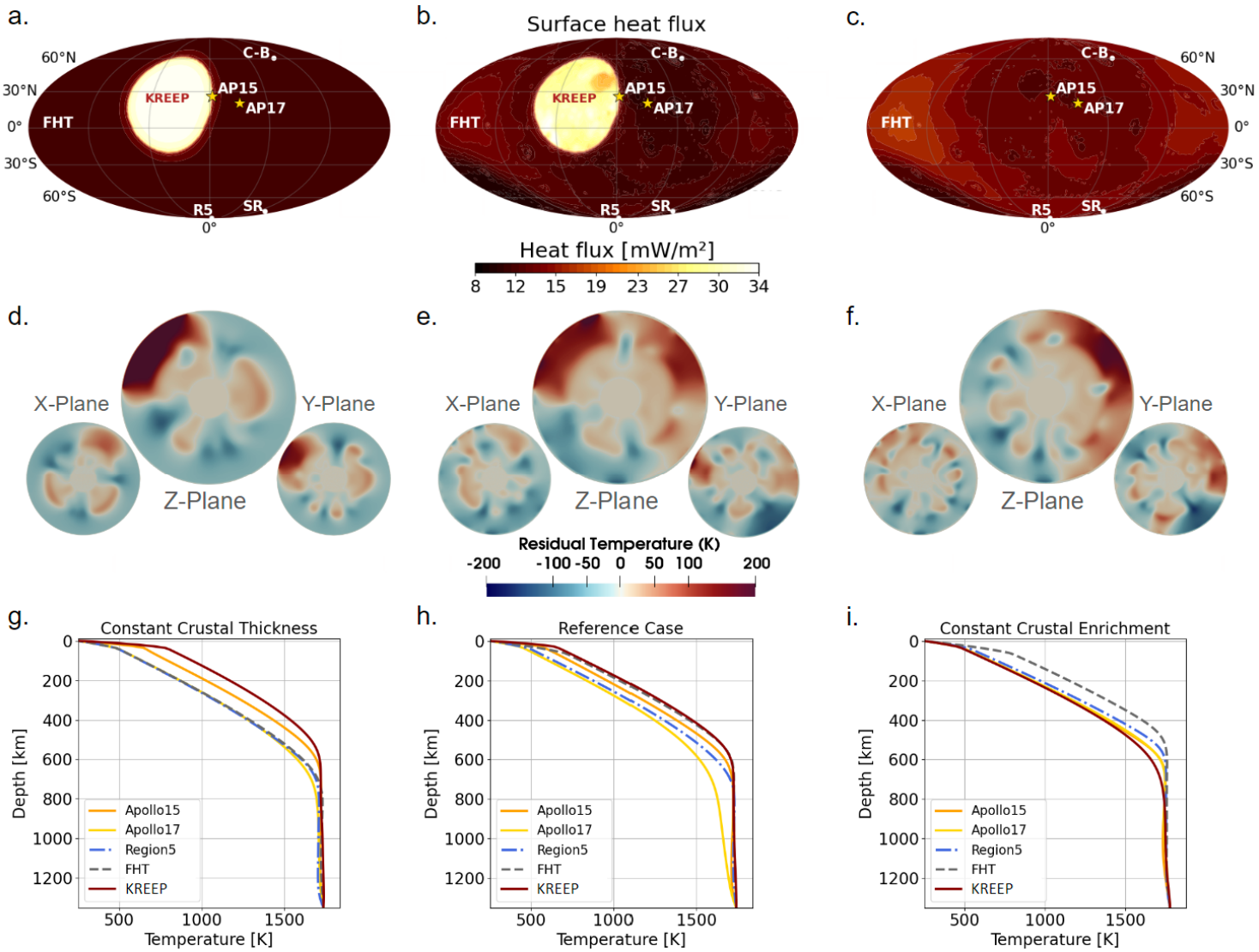

Figure 2. The three topmost panels display the present-day surface heat flux map, while also indicating KREEP and FHT regions, the landing sites of Apollo 15 and Apollo 17 (AP15 and AP17), Compton-Belkovich region (CB), Region 5 (R5) and Schroedinger crater. The three central panels show the interior temperature variation distribution as three sections perpendicular to each other, while the three bottom panels contain temperature profiles for different locations of interest at present day. Panels a, d and g refer to a model with laterally variable HPE enrichment and constant crustal thickness, analogous to the 0LW model from Laneuville et al. (2013). Panels b, e and h represent our reference case, including both laterally variable radiogenic enrichment and crustal thickness. Panels c, f and i correspond to a case with laterally variable crustal thickness but homogenous crustal enrichment in HPE.

dances, and crustal radiogenic enrichment. Our models are required to match the heat flux values measured by the two Apollo missions (18 ± 3 and 14 ± 2 mW/m^2 for Apollo 15 and Apollo 17, respectively, following the corrected estimated by Warren and Rasmussen, 1987). Moreover, we investigate the conditions for which it is possible to lower the background heat flux to values comparable to Region 5 estimates (about 6 mW/m^2).

We find that, if Apollo 15, Apollo 17 and Region 5 heat flux locations lie outside of the KREEP region (∼800km radius, smaller KREEP in Figure 3 a., b.), they are indistinguishable from one-another and comparable to the global average. For an 80° angular size KREEP region, with 1.22 ppm U in KREEP, 0.2 ppm in the crust and BSM Uranium abundance of 25 ppb, we find a best fit to the Apollo measurements. However, being Apollo 15 on the edge of the KREEP region, and both Apollo 17 and Region 5 outside of it, we find no measurable difference between the heat flux values at these latter two locations. The case of a larger KREEP region size (108° in Figure 3 a. and b.), with Apollo 15 being within the region, Apollo 17 on its edge and region 5 outside of it, uniquely allows for three measurably different heat flux values, and yields a best fit for 20 ppm BSM U concentration. Lastly, having the KREEP layer below the crust does not yield significant differences in present-day surface heat flux, but shows warmer temperatures in the KREEP region during the thermal history (about 500 K hotter at 60 km, Figure 4), which could explain the observed prolonged magmatic activity therein (Hiesinger et al., 2023). At the same time, models employing the KREEP below the crust show a larger difference in the viscosity profiles between the far- and nearside, which has been proposed to explain the difference in relaxation of lunar impact basins (Ding & Zhu, 2022).

4 Discussion

Previous studies have provided insights into the regional effects of key input parameters, such as HPE distribution and laterally variable crustal thickness, on present-day surface heat flux on the Moon (Siegler & Smrekar, 2014). Other works have focused on the effect of BSM Uranium abundance, size, enrichment and depth-wise location of the KREEP region on the global thermal evolution of the Moon (Laneuville et al., 2013, 2018). In this work, we built on the results of these two studies and combined their HPE distribution parameters with a laterally variable crustal thickness distribution. We provide, for the first time, a global scale thermal evolution model that is able to incorporate surface, average, and crust-mantle boundary heat flux constraints for a variety of lunar terranes.

None of the effects considered here can explain the high heat flux estimate in the Compton-Belkovich region (Siegler & Smrekar, 2014). This suggests the presence of a specific and highly localized feature (e.g., a potential magmatic intrusion) in this region. For comparison, we note that heat fluxes in excess of 150 mW/m^2, on Earth, can only be found at currently active volcanic regions, and with uncertainties in the range 30-60 mW/m^2 (Davies & Davies, 2010).

The effect of crustal thickness variations on thermal evolution modeling is highly dependent on the HPE enrichment assumed for the primordial lunar crust and on the crustal thickness model considered. In our case, using crustal enrichments of about 0.8 ppm thorium, consistent with the results of Yamashita et al. (2010) and Jolliff et al. (2000), and recent estimates of crustal thickness distributions that enhance the farside-nearside asymmetry (Broquet & Andrews-Hanna, 2024a), we find that a non-negligible contribution to the surface heat flux comes from the crust (order of 5 mW/m^2). On the other hand, when considering lower thorium abundances in the crust (¡0.5 ppm), similar to what is used in Laneuville et al. (2018), the effect of the crust becomes less significant.

The depth distribution of the KREEP layer (i.e., within the crust or below the crust) controls the thermal state of the lunar upper mantle. Intuitively, placing the heating layer (KREEP) below the crust corresponds to placing it under a low conductivity thermal blanket. Whereas, placing the KREEP anomaly within the crust means putting it into direct contact with the deep space (heat sink), facilitating the related energy loss. Indeed, Figure 4 shows that a KREEP layer placed below the crust keeps the upper mantle hotter throughout the enitre evolution (panels c. and d.) with respect to a KREEP within the crust case. Since this effect has important implications for the magmatic his-

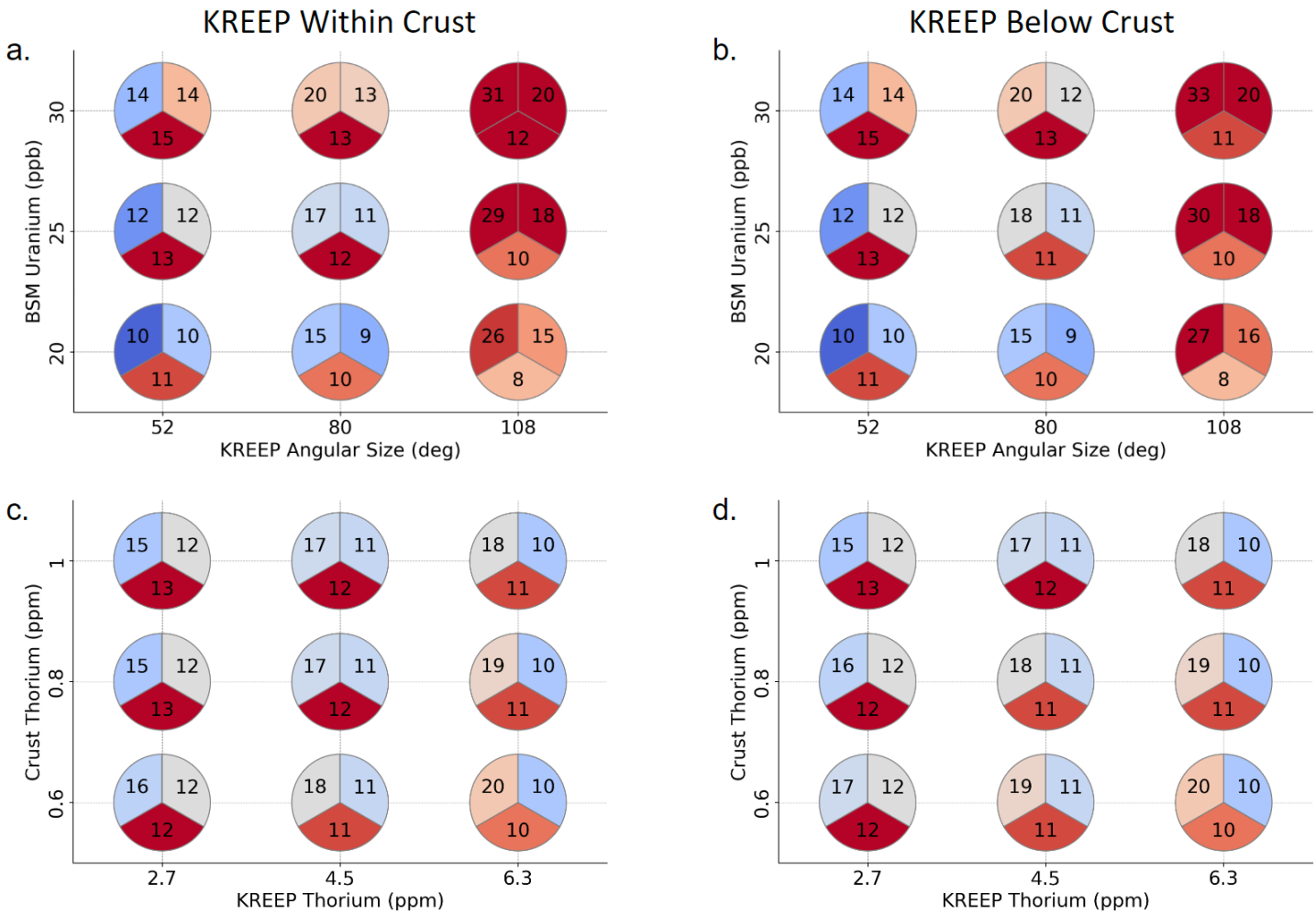

Figure 3. Results of model simulations varying KREEP region size versus BSM Uranium concentration, and varying KREEP enrichment versus global crustal enrichment. The leftmost column shows results for KREEP material spread within the crust, while the two right panels correspond to a KREEP layer located between crust and mantle. For each simulation, we show a pie chart with three heat flux datapoints; Apollo 15 landing site (top left), Apollo 17 landing site (top right) and Region 5 (bottom). A divergent colormap is used to represent the level of agreement between the modelled heat flux and measured values, with red indicating higher values than measured, blue for lower values than measured, and white for a negligible difference.

tory of the Moon (Hiesinger et al., 2023) and the viscous relaxation of nearside basins (Ding & Zhu, 2022), we favour models with the KREEP layer placed below the crust. This aspect is particularly relevant to maintaining the prolonged volcanic activity observed on the Moon (from about 4 to 1 Ga ago on the nearside, Hiesinger et al. 2023).

In this study we investigate three different sizes of the KREEP layer. The smallest size KREEP cuts halfway through Imbrium basin (about 800 km in diameter, Figure 1c). This scenario is interesting, as it gives a possible explanation for the peculiar character of the Imbrium basin, which shows a clear ring structure on its eastward side, while no ring is visible on the westward side (Broquet & Andrews-Hanna, 2024b; Liang et al., 2023). One of the possible explanation for the different evolution of the two sides of Imbrium basin is related to viscous relaxation, which is facilitated by high temperatures (¿1200 K) and low viscosities (lower than 10^{19} Pa s) at the base of the crust (Ding & Zhu, 2022). As shown in Figure 4, the small highly enriched KREEP yields the lowest viscosity in the early stages of lunar evolution. Since the KREEP region only affects the westward side of the basin, the low viscosity would facilitate the relaxation of this side only. Conversely, the eastward side would have viscosities above 10^{20} Pa s at the base of the crust, leaving this region only partially relaxed.

In the small KREEP scenario, the locations of Apollo 15, Apollo 17, and Region 5 all lie outside of the KREEP region, and show similar surface heat fluxes and thermal state. The resulting heat fluxes, in this case, are compatible with observations only if the two Apollo values would lie on the edges of their respective errorbars (15-16 mW/m^2). It should be noted here that, given the overlap in their values, the two Apollo measurements could be representative of the same terrane or, in other words, of a similar subsurface thermal state. However, this scenario would also require the uncertainties of the Region 5 estimate to be of the same order of the measurement itself.

Additionally, a small, higher enriched KREEP region below the crust (Figure 4b) is more consistent with the crustal annulus relaxation conditions within the PKT region, proposed by Ding and Zhu (2022): viscosity should attain values below 10^{19} Pa s at crust-mantle interface (∼30 km) and the thermal gradient should exceed 30 K/km (we find 40 K/km). Lastly, this KREEP region scenario is centered on the longest-lived volcanic eruptions on the Moon (Figure **??**, (Hiesinger et al., 2023)), which can be correlated to the center of the subsurface thermal anomaly (hottest point of the circular anomaly, (Laneuville et al., 2013)).
In case of a medium-sized KREEP region (about 1200 km in diameter), the configuration is optimal to match the Thorium map, with Apollo 15 being representative of the region's edge, and Apollo 17 representative of the global crust. In this case, lower values for KREEP thorium enrichment and BSM concentrations are plausible, reducing the density anomaly in the KREEP region, which might be otherwise inconsistent with the crustal thickness models, and showing surface average heat flux and BSM composition values similar to the estimates of (Warren & Rasmussen, 1987). However, the value in Region 5 never attains values lower than Apollo 17, again hinting at other reasons for anomalously low heat flux at the nearside south pole or at large uncertainties in the measurement.

The only configuration that allows for three different surface heat flow values for the locations considered here is that of the largest size of the KREEP region, with Apollo 15 representing the average KREEP heat flux, Apollo 17 the heat flux at the edge of the KREEP region, and Region 5 the nearside terrane outside of the KREEP region (Figure 3b). Whereas, this scenario requires a lower KREEP enrichment (∼3 ppm thorium) and possibly BSM uranium abundances below 20 ppm, it is still consistent with the results of Warren and Rasmussen (1987).

In brief, a larger KREEP region of low enrichment is optimal to fit the Region 5 estimate, an intermediate sized KREEP region of intermediate enrichment is optimal to

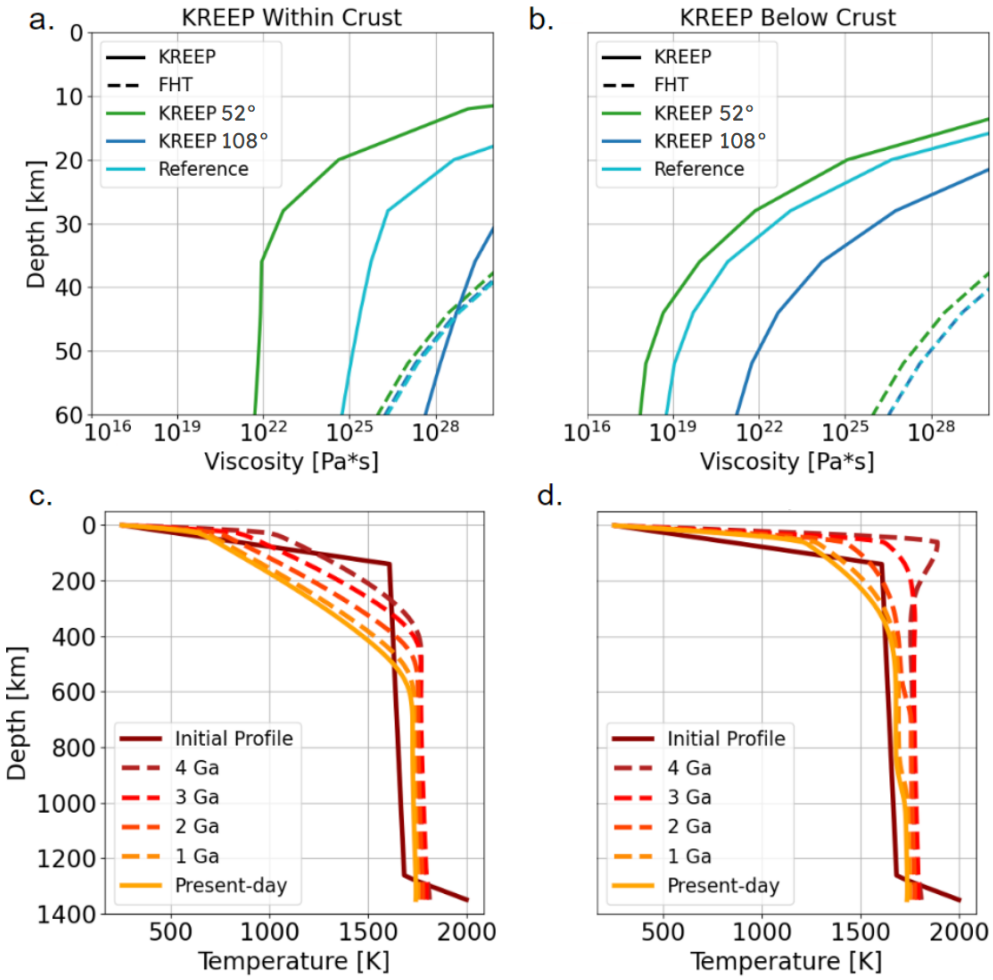

Figure 4. Panel a. shows a depth-wise portion of the viscosity profiles (from surface to 60 km depth) in the FHT and KREEP regions, when the KREEP enrichment is spread within the crust, for three scenarios: smaller and more enriched KREEP (case KREEP 52°), larger and less enriched KREEP (case KREEP 108°), and an intermediate case (Reference case). Hence, panel a. show three different models, each represented by two curves: FHT region (dashed) and KREEP region (solid) viscosity profiles, for a small, intermediate and large KREEP angular size. The FHT viscosity profile for the large KREEP case (dark blue dashed curve), is partly overlain by the Reference case FHT curve, partially hiding it. Panel c. shows thermal profiles throughout the whole mantle at different times up to present-day, for the Reference model only. Panels b. and d. are analogous to a. and c., but for a KREEP layer placed below the crust rather than spread within it. All viscosity profiles are taken at 3.9 Ga ago, during late heavy bombardment, which is most relevant for basin formation and subsequent relaxation (Ding & Zhu, 2022).

explain the two Apollo measurements, while overestimating Region 5 values, and a small, highly enriched KREEP region can only fit one heat flux value for both Apollo measurements, but is more consistent with basin relaxation and prolonged volcanic activity.

One possible implication of the aforementioned results is that the assumption of a homogeneously enriched, circular KREEP region is too simplistic to capture the high complexity and lateral variability of the quantities at play. A more complex KREEP region geometry, and possibly including an HPE enrichment gradient as a function of the distance from the centre, may be necessary to further constrain the present-day thermal state of the Moon and its evolution.

Excluding the small and medium case scenarios solely based on the Region 5 value would is not advisable, due to the absence of an errorbar or quantified uncertainty related to the estimate. Until new measurements are taken or new information is provided regarding the Region 5 estimate, we can only consider the result and implications of the different scenarios under the respective best-fit conditions.

New evidence may soon come from the ongoing and upcoming lunar missions: the Chang'e 6 farside sample return (May-June 2024) can already provide indirect constraints on farside highlands composition, and specifically HPE abundances, which can be immediately included in the present model. Furthermore, the NASA CLPS-CP-12 (scheduled for launch in 2026; Schonfeld, 2023) will provide both seismic and heat flux measurements at Schrödinger crater, whose location is close to Region 5. If the heat flux at Schrödinger crater shows a value comparable to the Region 5 estimate, then a larger surface heat flux variability is needed and, in this case, we would favor a large KREEP scenario. Conversely, if the Schrödinger estimate would be comparable to the Apollo 17 measurement, then our models favor a KREEP size smaller than 1500 km in diameter (small and moderate KREEP size scenarios in Figure 3).

We note that the addition of any in-situ datapoint, ideally located outside of any HPE anomaly as is the case for the Schrödinger crater, will narrow down the current scenarios allowing for a better characterization of the HPE anomaly on the Moon. Our models indicate a surface heat flux value of 11-12 mW/m^2 within Shrödinger basin, for all cases in Figure 4b. Thus, either confirming or refuting this estimate will help improve our understanding of the present-day thermal state of the Moon.

5 Conclusion

In the present study, we presented a global thermal evolution model consistent with global and local scale constraints for the thermal state of the lunar interior. We evaluated the effects of a laterally variable crustal thickness on the evolution and present-day heat flux on the Moon. We found that the difference in surface heat flux between nearside and farside is significant (order of 5 mW/m^2) for crustal enrichments of $\sim$0.5-1 ppm thorium, while being limited for lower crustal enrichment (0.2-0.3 ppm thorium).

Based on the spatial variability of the surface heat flux at Apollo and Region 5 sites, we favour a model with a large KREEP region (about 1500 km radius), located below the crust with a thorium content lower than 4.5 ppm. However, given the large uncertainties associated with the heat flux estimates, other scenarios are possible. Future heat flux measurements such as the one from NASA CLPS-CP-12 in the Shrödinger basin will provide a unique opportunity to test the scenarios proposed here.

Acknowledgments
We would like to express our sincere gratitude to TU Delft for supporting this research in collaboration with the German Aerospace Centre, and for the funding provided through

the Erasmus+ programme. This assistance has been invaluable in enabling the successful completion of this research.

References

Broquet, A., & Andrews-Hanna, J. (2024a, January). The moon before mare. *Icarus*, *408*, 115846. Retrieved from http://dx.doi.org/10.1016/j.icarus.2023.115846 doi: 10.1016/j.icarus.2023.115846

Broquet, A., & Andrews-Hanna, J. (2024b, March). A volcanic inventory of the moon. *Icarus*, *411*, 115954. Retrieved from http://dx.doi.org/10.1016/j.icarus.2024.115954 doi: 10.1016/j.icarus.2024.115954

Davies, J. H., & Davies, D. R. (2010). Earth's surface heat flux. *Solid Earth*, *1*(1), 5–24. Retrieved from https://se.copernicus.org/articles/1/5/2010/ doi: 10.5194/se-1-5-2010

Ding, M., & Zhu, M. (2022, March). Effects of regional thermal state on the crustal annulus relaxation of lunar large impact basins. *Journal of Geophysical Research: Planets*, *127*(3). Retrieved from http://dx.doi.org/10.1029/2021JE007132 doi: 10.1029/2021je007132

Garcia, R. F., Khan, A., Drilleau, M., Margerin, L., Kawamura, T., Sun, D., ... Zhu, P. (2019, November). Lunar seismology: An update on interior structure models. *Space Science Reviews*, *215*(8). Retrieved from http://dx.doi.org/10.1007/S11214-019-0613-Y doi: 10.1007/s11214-019-0613-y

Hiesinger, H., van der Bogert, C., Michael, G., Schmedemann, N., Iqbal, W., Robbins, S., ... Head, J. (2023, December). The lunar cratering chronology. *Reviews in Mineralogy and Geochemistry*, *89*(1), 401–451. Retrieved from http://dx.doi.org/10.2138/rmg.2023.89.10 doi: 10.2138/rmg.2023.89.10

Hüttig, C., & Stemmer, K. (2008a, December). Finite volume discretization for dynamic viscosities on voronoi grids. *Physics of the Earth and Planetary Interiors*, *171*(1–4), 137–146. Retrieved from http://dx.doi.org/10.1016/j.pepi.2008.07.007 doi: 10.1016/j.pepi.2008.07.007

Hüttig, C., & Stemmer, K. (2008b, February). The spiral grid: A new approach to discretize the sphere and its application to mantle convection. *Geochemistry, Geophysics, Geosystems*, *9*(2). Retrieved from http://dx.doi.org/10.1029/2007GC001581 doi: 10.1029/2007gc001581

Hüttig, C., Tosi, N., & Moore, W. B. (2013, July). An improved formulation of the incompressible navier–stokes equations with variable viscosity. *Physics of the Earth and Planetary Interiors*, *220*, 11–18. Retrieved from http://dx.doi.org/10.1016/j.pepi.2013.04.002 doi: 10.1016/j.pepi.2013.04.002

Jaumann, R., Hiesinger, H., Anand, M., Crawford, I., Wagner, R., Sohl, F., ... Oberst, J. (2012, December). Geology, geochemistry, and geophysics of the moon: Status of current understanding. *Planetary and Space Science*, *74*(1), 15–41. Retrieved from http://dx.doi.org/10.1016/j.pss.2012.08.019 doi: 10.1016/j.pss.2012.08.019

Jolliff, B. L., Gillis, J. J., Haskin, L. A., Korotev, R. L., & Wieczorek, M. A. (2000, February). Major lunar crustal terranes: Surface expressions and crust-mantle origins. *Journal of Geophysical Research: Planets*, *105*(E2), 4197–4216. Retrieved from http://dx.doi.org/10.1029/1999JE001103 doi: 10.1029/1999je001103

Laneuville, M., Taylor, J., & Wieczorek, M. A. (2018, December). Distribution of radioactive heat sources and thermal history of the moon. *Journal of Geophysical Research: Planets*, *123*(12), 3144–3166. Retrieved from http://dx.doi.org/10.1029/2018JE005742 doi: 10.1029/2018je005742

Laneuville, M., Wieczorek, M. A., Breuer, D., & Tosi, N. (2013, July). Asymmetric thermal evolution of the moon. *Journal of Geophysical Research: Planets*, *118*(7), 1435–1452. Retrieved from http://dx.doi.org/10.1002/jgre.20103

doi: 10.1002/jgre.20103

Langseth, M. G., Keihm, S. J., & Peters, K. A. (1976). The revised lunar heat flow values.. Retrieved from https://api.semanticscholar.org/CorpusID:91317287

Lawrence, D. J., Feldman, W. C., Barraclough, B. L., Binder, A. B., Elphic, R. C., Maurice, S., ... Prettyman, T. H. (1999, September). High resolution measurements of absolute thorium abundances on the lunar surface. *Geophysical Research Letters*, *26*(17), 2681–2684. Retrieved from http://dx.doi.org/10.1029/1999GL008361 doi: 10.1029/1999gl008361

Liang, W., Andrews-Hanna, J. C., & Evans, A. J. (2023, December). The missing craters and basin rings beneath the lunar maria. *Journal of Geophysical Research: Planets*, *128*(12). Retrieved from http://dx.doi.org/10.1029/2023JE007876 doi: 10.1029/2023je007876

McEwen, A., & Robinson, M. (1997, January). Mapping of the moon by clementine. *Advances in Space Research*, *19*(10), 1523–1533. Retrieved from http://dx.doi.org/10.1016/S0273-1177(97)00365-7 doi: 10.1016/s0273-1177(97)00365-7

Paige, D., & Siegler, M. (2016). NEW CONSTRAINTS ON LUNAR HEAT FLOW RATES FROM LRO DIVINER LUNAR RADIOMETER EXPERIMENT POLAR OBSERVATIONS. In (47th ed.).

Schonfeld, J. (2023). Summary of the contracted deliveries of nasa payloads to the moon via commercial lunar payload services (clps). In *2023 ieee international conference on systems, man, and cybernetics (smc)* (p. 863-866). doi: 10.1109/SMC53992.2023.10394001

Siegler, M., Feng, J., Lehman-Franco, K., Andrews-Hanna, J. C., Economos, R. C., Clair, M. S., ... White, M. N. (2023, July). Remote detection of a lunar granitic batholith at compton–belkovich. *Nature*, *620*(7972), 116–121. Retrieved from http://dx.doi.org/10.1038/s41586-023-06183-5 doi: 10.1038/s41586-023-06183-5

Siegler, M., & Smrekar, S. (2014, January). Lunar heat flow: Regional prospective of the apollo landing sites. *Journal of Geophysical Research: Planets*, *119*(1), 47–63. Retrieved from http://dx.doi.org/10.1002/2013JE004453 doi: 10.1002/2013je004453

Wang, X., Zhang, X., & Wu, K. (2016, June). Thorium distribution on the lunar surface observed by chang'e-2 gamma-ray spectrometer. *Astrophysics and Space Science*, *361*(7). Retrieved from http://dx.doi.org/10.1007/s10509-016-2816-y doi: 10.1007/s10509-016-2816-y

Warren, P. H., & Rasmussen, K. L. (1987, April). Megaregolith insulation, internal temperatures, and bulk uranium content of the moon. *Journal of Geophysical Research: Solid Earth*, *92*(B5), 3453–3465. Retrieved from http://dx.doi.org/10.1029/JB092iB05p03453 doi: 10.1029/jb092ib05p03453

Yamashita, N., Hasebe, N., Reedy, R. C., Kobayashi, S., Karouji, Y., Hareyama, M., ... Kim, K. J. (2010, May). Uranium on the moon: Global distribution and u/th ratio. *Geophysical Research Letters*, *37*(10). Retrieved from http://dx.doi.org/10.1029/2010GL043061 doi: 10.1029/2010gl043061

Zuber, M. T., Smith, D. E., Watkins, M. M., Asmar, S. W., Konopliv, A. S., Lemoine, F. G., ... Yuan, D.-N. (2013, February). Gravity field of the moon from the gravity recovery and interior laboratory (grail) mission. *Science*, *339*(6120), 668–671. Retrieved from http://dx.doi.org/10.1126/science.1231507 doi: 10.1126/science.1231507

Geophysical Research Letters

Supporting Information for

Present-day thermal state and surface heat flux of the Moon

S. Santangelo[1,2], A.-C. Plesa[1], A. Broquet[1], D. Breuer[1], B. Root[2]

[1]German Aerospace Center (DLR), Institute of Planetary Research, Rutherfordstr. 2, 12489 Berlin, Germany., [2]Delft University of Technology, Kluyverweg 1, 2629 HS Delft, The Netherlands.

Contents of this file

Symbol	Description	Value
R_p	Planet radius	1740 km
R_c	Core radius	390 km
D_K	KREEP layer thickness (below crust)	∼30 km
T_{surf}	Surface temperature	250 K
T_0	Reference temperature	1600 K
T_c	Core temperature	2000 K
P_0	Reference pressure	3 Gpa
η_0	Reference viscosity	10^{21} Pa s
E	Activation energy	$3 \cdot 10^5$ J mol^{-1}
V	Activation volume	$6 \cdot 10^{-6} m^3$
R	Universal gas constant	8.314 J mol^{-1} K^{-1}
c_p	Mantle specific heat capacity	1000 J kg^{-1} K^{-1}
k_c	Crust thermal conductivity	1.5 W m^{-1} K^{-1}
k_m	Mantle thermal conductivity	3 W m^{-1} K^{-1}
κ_0	Reference thermal diffusivity	$8.82 \cdot 10^{-7}$ m^2 s^{-1}
ρ_0	Reference density (mantle)	3400 kg m^{-3}
ρ_c	Crustal density	2500 kg m^{-3}
α_0	Thermal expansivity	$2 \cdot 10^{-5}$ K^{-1}
$c_{p,\text{ core}}$	Core specific heat capacity	800 J kg^{-1} K^{-1}
ρ_{core}	Core density	7400 kg m^{-3}
ΔT	Temperature variation across the mantle	1750 K
Q	Radiogenic heating	$1.896 \cdot 10^{-11}$ W/kg
g	Surface gravity acceleration	1.62 m s^{-2}
Ra	Reference thermal Rayleigh number	$5.37 \cdot 10^5$
Ra_C	Reference HPE Rayleigh number	$1.2 \cdot 10^6$

Part III

Crustal Conductivity Model

1

Methods

In the present chapter, we will describe the methods used to address the second sub-question mentioned in the Research Objective section (1.5.3), namely:

- Can present-day lunar surface heat-flux and topography constrain megaregolith layer thickness and thermal conductivity of lunar crust?

In previous sections, we have seen how coupling thermal evolution models with a laterally variable distribution of HPE and crustal thickness can enhance our understanding of lunar present-day state. However, our treatment of all other crustal properties remains laterally constant, preventing us from gaining insight into how different the lunar crust can be across the surface. In particular, one of the primary motivations for this study is to integrate insights from regional-scale modeling (e.g., Siegler and Smrekar, 2014) into a global geodynamic model. In order to do so, we initially included two of the three properties found to have the most effect on surface heat flux in Siegler and Smrekar (2014), namely HPE and crustal thickness distribution.

Thus, the goal of this chapter is to develop a consistent method to integrate our model with the third key parameter, that is, crustal conductivity, as a laterally variable quantity. It is important to note here that varying the distribution of crustal thermal conductivity will not directly affect the surface heat flux, but will change the thermal gradient that produces it. In other words, following the relation $H = -k\nabla T$; varying the thermal conductivity (k) will cause the temperature distribution (thermal gradient ∇T) to change proportionally in order to yield the same heat flux (H). This implies that all previous results based on heat flux values remain equally valid, but varying the k parameter allows to indipendently tune the subsurface temperatures to fit secondary constraints.

1.1. General Approach

We employ an approach similar to what is used in Siegler and Smrekar (2014) to model crustal conductivity based on porosity data from gravity (section 2.4.2). However, instead of focusing on depth variations throughout the crust, limited by our relatively low radial resolution in global scale (8 km resolution for a 39 km average crustal thickness), we let the thermal conductivity vary laterally. In other words, we compute one effective crustal thermal conductivity value for each surface location.

The input parameters influencing the conductivity value at each location are the following: anorthositic crust thickness, mare basalt thickness (Broquet & Andrews-Hanna, 2024a), crustal porosity (Wahl et al., 2020), bulk conductivity of lunar anorthosites and basalts (Halbert & Parnell, 2022; Henke et al., 2016; Warren & Rasmussen, 1987), and thickness of the porous (megaregolith) layer. The latter quantity is highly unconstrained in gravity analyses (Wahl et al., 2020; Wieczorek et al., 2013), possibly ranging from a few to tens of kilometers. From the perspective of crustal stratigraphy, such a layer can be

representative of what is referred to as megaregolith layer (section 1.4), which is also thought to lie in a similar thickness range Liu et al., 2022.

As extensively discussed above, we can use heat flux data to constrain the abundance and distribution of HPE on the Moon, for different KREEP layer configurations. Since we compute surface heat flux as k multiplied by ∇T, a trade-off exists between the temperature distribution and thermal conductivity in the crust. Indeed, simply varying the thermal conductivity in the crust will cause the thermal gradient to adapt, yielding the same present-day surface heat flux. Thus, we need an independent constraint on crustal temperature distribution. One such constraint comes from the analysis of crustal structure around lunar basins of diameters larger than 450 km (Ding & Zhu, 2022). In particular, the results of this study suggest an upper bound for nearside and a lower bound for farside viscosity, at the time of basin formation (~4.2-3.8 Ga ago). As described in section 2.3.1, viscosity is highly dependent on temperature, and can be explicitly computed as output of our model, allowing a direct comparison with the viscosity boundaries provided in Ding and Zhu (2022).

We select best-fit models based on the combined compliance of near- and farside early viscosity profiles (at 4 Ga) with the basin relaxation conditions in Ding and Zhu (2022). In this case, we vary the thickness and thermal conductivity of the farside porous (megaregolith) layer and the average crustal conductivity of nearside mare regions to address the respective constraints. Thus, we gain insight on which combinations of parameters produce more realistic conductivities in the two hemispheres, constraining the structure of lunar crust in terms of thermal properties.

1.2. Constraints

In this section, we further describe the concepts behind the formulation of the constraints that we satisfy in the second part of this study. As mentioned in section 1.1, the results of Ding and Zhu (2022) provide an upper bound for nearside and a lower bound for farside viscosity at a specific time during lunar evolution (i.e., between 4.2 and 3.8 Ga, for simplicity all results are taken at 4 Ga). Constraints provided in Ding and Zhu (2022) come from the analysis of the crustal structure around major lunar basins.

Upon a high-energy impact, the crustal thickness is locally reduced and, at the same time, a transient positive temperature anomaly is produced by the energy transfer. In a relatively cold crustal and sub-crustal environment, the basin structure is quickly ”frozen” in its original shape. Subsequently, at a much slower pace (tens of millions of years, Ding and Zhu, 2022), isostatic rebound uplifts the center of the cavity due to the buoyancy of the thinned crust. Thus, at present-day, we expect to see a thin uplifted central cavity, surrounded by an annulus of thicker crust. Indeed, the crustal annulus is defined in (Ding & Zhu, 2022) as a thick crust signature, visible in crustal thickness inversions, surrounding a basin. In other words, for a relatively cold subsurface, we expect a deeper crust-mantle relief surrounding large basins.

Conversely, if the crustal and subcrustal environment is relatively warm (>1200 K, Ding and Zhu, 2022) at the time of impact, and throughout the following few tens of millions of years, the basin structure may not remain frozen in its initial configuration. In particular, due to high crust-mantle interface temperatures and, thus, low viscosities, crustal annuli can flow laterally, smoothing out the Moho relief around basins.

The conditions under which one or the other scenario is most likely to occur has been studied in Ding and Zhu (2022). Nearside basins (e.g., Imbrium, Serenitatis) show less pronounced or absent crustal annuli, implying that the thermal state of nearside crust at the time of their formation allowed an almost total relaxation. Farside basins (e.g., Moscoviense, Freundlich-Sharonov), on the other hand, display sharp crustal annuli, suggesting much colder thermal states.

The main result of Ding and Zhu (2022) is the definition of thresholds for the presence or absence of annulus relaxation, which they formulate in terms of viscosity at crust-mantle boundary and thermal gradient in the immediate subsurface. For the complete relaxation of nearside basins, it is necessary

to reach crust-mantle interface viscosity values below 10^{19} Pa s, and thermal gradients in excess of 30 K/km in the immediate subsurface. Conversely, for completely unrelaxed annuli, Moho viscosities between 10^{26}-10^{28} Pa s and subsurface thermal gradients between 10 and 20 K/km are required.

Testing the conditions for presence or absence of basin relaxation, as given in Ding and Zhu (2022) is complex, requiring the retrieval of local viscosity estimates at crust-mantle boundary and at a specific moment in time (i.e., around 4.2-3.8 Ga). However, our global scale, thermal evolution models allow us to directly address these constraints relevant to the early evolution of the Moon.

1.3. Porosity Data

The first step in the computation of an effective thermal conductivity map is to obtain a porosity map from the combination of gravity and porosity data. In this case, we chose the dataset provided in Wahl et al. (2020), which constitutes a recent and more refined interpretation of GRAIL data, building on the methods in Wieczorek et al. (2013). The raw data obtained from the original publication was interpolated on a regular latitude-longitude grid with 1° resolution, using a standard cubic method, to produce Figure 1.1:

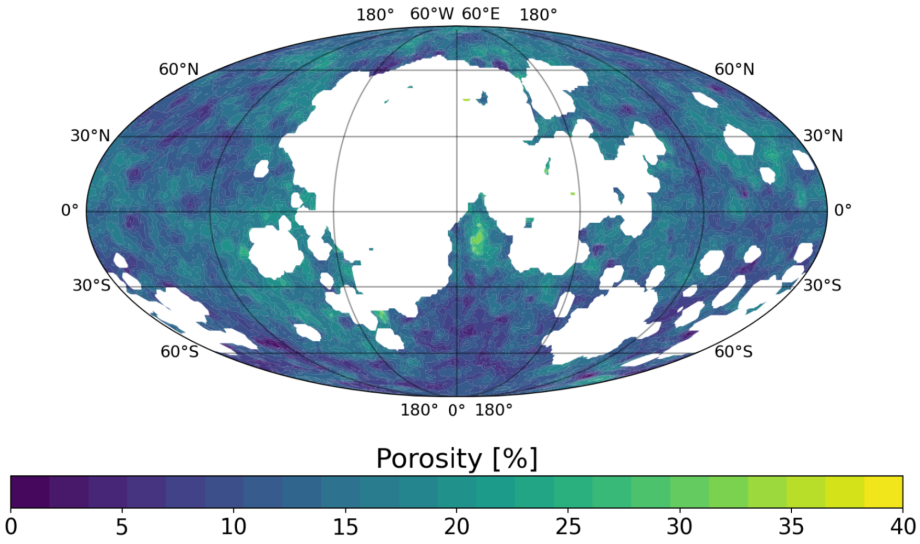

Figure 1.1: Porosity map adapted from Wahl et al. (2020) data, expressed in percentages (equation 2.28). The porosity range goes from about 0% to 36.5%. The regions outlined in white correspond to surface areas that are overlain by basaltic material, making the gravity inversion highly uncertain. For more information on how the porosity map is computed, we refer to section 2.4.2.

Looking at Figure 1.1 and 2.4, we can observe how large basins, most of which are flooded with basalts (regions in white), have fractured the crust and increased the porosity of the surrounding terrain. Thereafter, subsequent smaller-size impactors have compacted the deeper crust, while producing the finer outermost regolith blanket. Therefore, we see higher porosity around large basins (e.g., Orientale, Moscoviense, Smythii), and lower porosity in the highly cratered farside and polar regions. Low porosity regions appear as darker dots, corresponding to smaller, more recent impact sites.

1.4. Conductivity From Porosity

In order to use porosity as a proxy for thermal conductivity, an empirical relation is needed to correlate the two quantities, preferably derived for samples as close as possible to lunar crust. Extensive work has been undertaken to find this correlation for chondritic asteroids material, mostly based on the analysis of meteorite samples (e.g. Grott et al., 2019; Henke et al., 2016). We tested four different models, which we will refer to as K_i for $i = 0, ..., 3$:

$$K_0 = \frac{0.11(1-\phi)}{\phi}; \qquad \text{(Grott et al., 2019, Eq. 5)} \qquad (1.1)$$

$$K_1 = k_b \exp\left(-\frac{\phi}{0.08}\right); \qquad \text{(Henke et al., 2016, Eq. 18)} \qquad (1.2)$$

$$K_2 = k_b\,(1 - 2.216\phi)\,; \qquad \text{(Henke et al., 2016, Eq. 19)} \qquad (1.3)$$

$$K_3 = k_b \exp\left(1.2 - \frac{\phi}{0.167}\right); \qquad \text{(Henke et al., 2016, Eq. 21)} \qquad (1.4)$$

where ϕ is the porosity, defined as $1 - \rho_b/\rho_g$, with ρ_b the bulk density and ρ_g the grain density (equation 2.28), and k is thermal conductivity. We note that, in this case, what we refer to as bulk represents a material that has exactly zero porosity, which never occurs naturally. In simple terms, each model comes from a different fit of similar datasets for chondritic asteroids, but models K_1, K_2 and K_3 are adapted to represent physical quantities characteristic of lunar material (Figure 1.2).

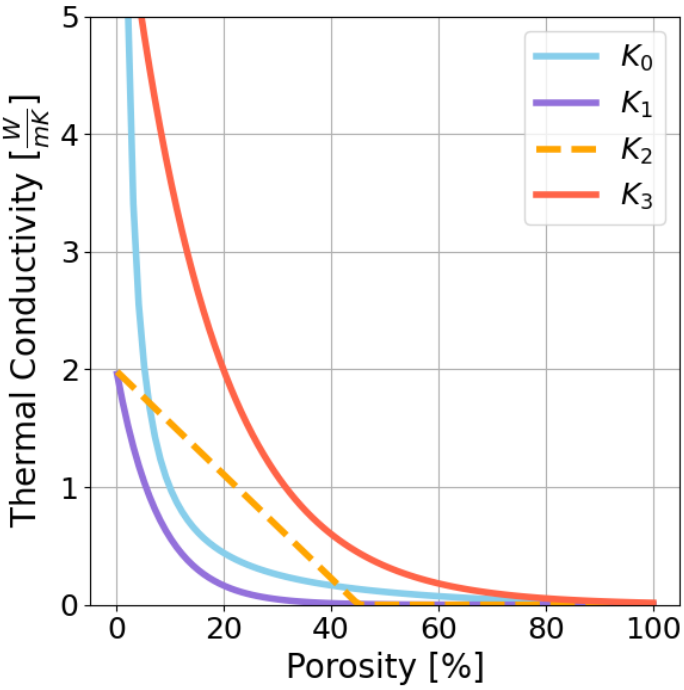

Figure 1.2: Summary plot of different thermal conductivity models as a function of porosity. Model K_0 is taken from Grott et al. (2019), while models K_{1-3} are taken from Henke et al. (2016)

Each model has specific advantages, depending on the material of interest and the porosity range. Model K_0 is an empirical fit to thermal conductivity values of chondritic material, and does not depend on any specific property of the material, including only one purely empirical parameter. Model K_1 fits data specific to H and L chondrites (Henke et al., 2016), but it depends on the k_b parameter, which is an extrapolated value for zero porosity material (equal to 4.3 W/(mK) for H and L chondrites). Here, we will use a value for compact lunar anorthositic crust. The work by Warren and Rasmussen (1987) provides an estimate of this value for primordial lunar crust of 1.8 W/(mK), while Henke et al. (2016) found values of about 1.7 W/(mK) for anorthite ($CaAl_2Si_2O_8$) and about 2 W/(mK) for plagioclase, of which anorthite is one of the constituents.

Similar to the previous case, model K_2 depends upon k_b. This model is a linear rather than exponential fit and provides reasonable values for different materials at medium to low porosities (Henke

et al., 2016). Lastly, model K_3 is intended for highly porous material, which should not attain zero thermal conductivity before reaching porosities close to 100% (Henke et al., 2016). Considering that we are interested in the anorthositic crust material, with a porosity range of about 0 to 35%, we can firstly exclude the two models that diverge at porosities close to zero, being more suited for materials that do not reach such low values. Thus, we are left with models K_1 and K_2, which yield similar values in our range of interest. In particular, our porosity never reaches 40%, allowing us to use model K_2 despite it reaching zero thermal conductivity for porosities slightly higher. Therefore, we test both models, considering K_1 a lower and K_2 an upper bound for our crust conductivity values. Concerning the bulk conductivity value, to be used in Equations 1.2-1.4, we consider a range of 1.6-2 W/(mK) for lunar crust when tuning our model.

1.5. Basalt Regions

In the previous section we described the treatment of thermal conductivity of our porous layer, that is, relevant for all locations in Figure 1.1 where a porosity value is available. We are then left with many basalt-covered regions (white areas), where we cannot use a porosity to conductivity correlation. However, one of the advantages of the crustal thickness model we chose (Broquet & Andrews-Hanna, 2024a), is that it provides both the global thickness of anorthositic primordial crust and the thickness of the overlaying basalts (Figure 1.3). Therefore, we can use basalt thickness data to estimate the local amount of this material present in the gaps of Figure 1.1. We use the thickness of the basalt layer and of the crust to locally calculate an effective thermal conductivity at each location, using a compact basalt thermal conductivity of 2.6 W/(mK) that we discuss in more detail below.

However, the stratigraphic structure of these regions is known to be much more complex, likely comprised of multiple layers of volcanic material separated by compacted ejecta (regolith) of much lower conductivity (Gong et al., 2016). On the other hand, it is reasonable to assume that such a complex structure is characterised by a lower thermal conductivity value compared to our simple model. Thus, we can use the above mentioned approach as an upper bound initial guess to be later constrained using the differential viscous relaxation of farside and nearside, as described in section 1.1.

Now, in addition to the basalt thickness data, the described approach needs an estimate for bulk thermal conductivity of basalt and underlying anorthosite. For the latter value, we already discussed a plausible range in section 1.4, which is also applicable in this case; as for the former quantity, we refer to the results in Halbert and Parnell (2022), where lunar basalt simulants are found to have an average thermal conductivity of about 2.6 W/(mK) at typical upper crust temperatures (250-290 K).

1.6. Conductivity Model

As a last step in computing a global thermal conductivity map, we describe how the various datasets come together into one final product. Firstly, we note how, despite the high level of correlation between the basalt thickness data in Figure 1.3 and missing basalt-covered regions data in Figure 1.1, the two datasets do not perfectly overlap. In particular, basalt thicknesses below 0.1 km are not considered in the dataset in Figure 1.3, while the corresponding porosity is also unavailable in Figure 1.1 data. Therefore, after computing the effective crustal thermal conductivity at all locations where either basalt thickness or porosity data exist, an interpolation of the data is necessary to avoid gaps in the final dataset.

Moving on to the computation of effective conductivity, this is approached in the simplest manner. The layer characterised by the porosity in Figure 1.1 is assumed to have a constant thickness, which is varied between 4 and 10 km across different models. Below this layer, we assume anorthositic crust of constant conductivity but laterally variable thickness. At each latitude-longitude location, we compute an effective thermal conductivity, using the following equation:

$$\frac{d_{cr}(\Lambda,\lambda)}{k_{Eff}(\Lambda,\lambda)} = \frac{d_P}{k_P(\Lambda,\lambda)} + \frac{d_{cr}(\Lambda,\lambda) - d_P}{k_b}; \tag{1.5}$$

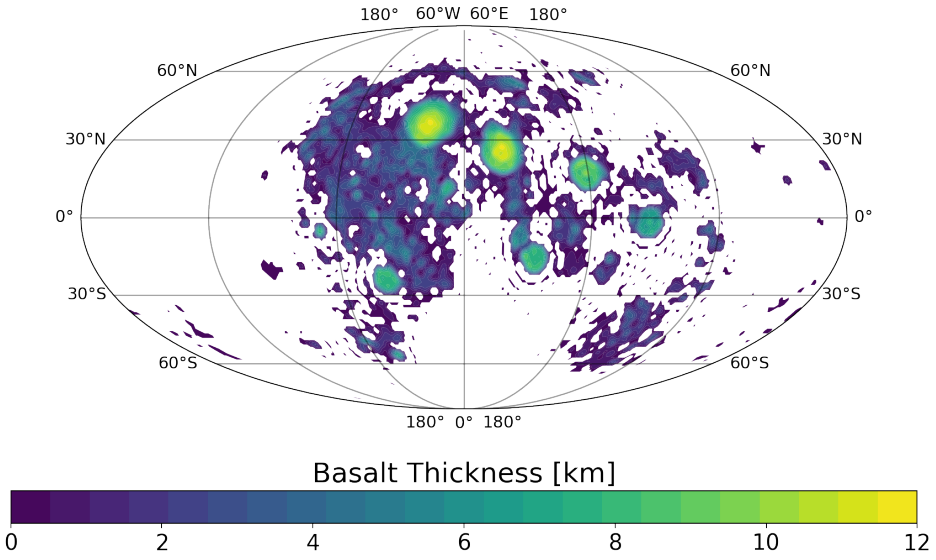

Figure 1.3: Basalt thickness map, in km, adapted from Broquet and Andrews-Hanna (2024a) data. The data has a minimum of 0.1 km outside of any major basin, a maximum of about 12 km in the two largest basins in Figure (Imbrium on the left and Serenitatis on the right).

where d represents thickness, Λ and λ are longitude and latitude, subscript cr stands for crust, that is, the whole crustal layer (thickness of which is in Figure 2.4.1), P stands for porous layer, $_{Eff}$ for effective value, and b stands for bulk (compact) anorthositic crust value. In equation 1.5, we solve for k_{Eff}, which is a function of surface location through the laterally variable crustal thickness ($d_{cr}(\Lambda, \lambda)$) and thermal conductivity of the porous layer ($k_P(\Lambda, \lambda)$). Thus, we compute the effective crustal conductivity at each surface location as the combination of a porous layer of fixed thickness (d_P) and underlying compacted anorthosite, which has a different thickness at every location. This equation is formulated for each location where a porosity datapoint is available.

On the other hand, every location that does not correspond to any datapoint in Figure 1.1, while corresponding to a point where basalt thickness is defined (Figure 1.3), is treated slightly differently. In this case, subscripts P in equation 1.5 can be virtually substituted with subscripts B for basalts, where now k_B is the thermal conductivity of basalt and $d_B(\Lambda, \lambda)$ is also function of surface location, modifying the equation as follows:

$$\frac{d_{cr}(\Lambda, \lambda)}{k_{Eff}(\Lambda, \lambda)} = \frac{d_B(\Lambda, \lambda)}{k_B} + \frac{d_{cr}(\Lambda, \lambda) - d_P(\Lambda, \lambda)}{k_b}. \tag{1.6}$$

The combination of equations 1.5 and 1.6 provides an almost complete thermal conductivity map for the Moon's crust. We are only left with the interpolation of thermal conductivity data for the few regions of no porosity data and basalt thickness below 0.1 km, which we perform using the 2D cubic interpolation function of the griddata package in python. The resulting complete thermal conductivity maps are shown in Figure 1.4, for porous layer boundary thicknesses of 4 and 10 km, and for the two chosen porosity-conductivity models K_1, K_2:

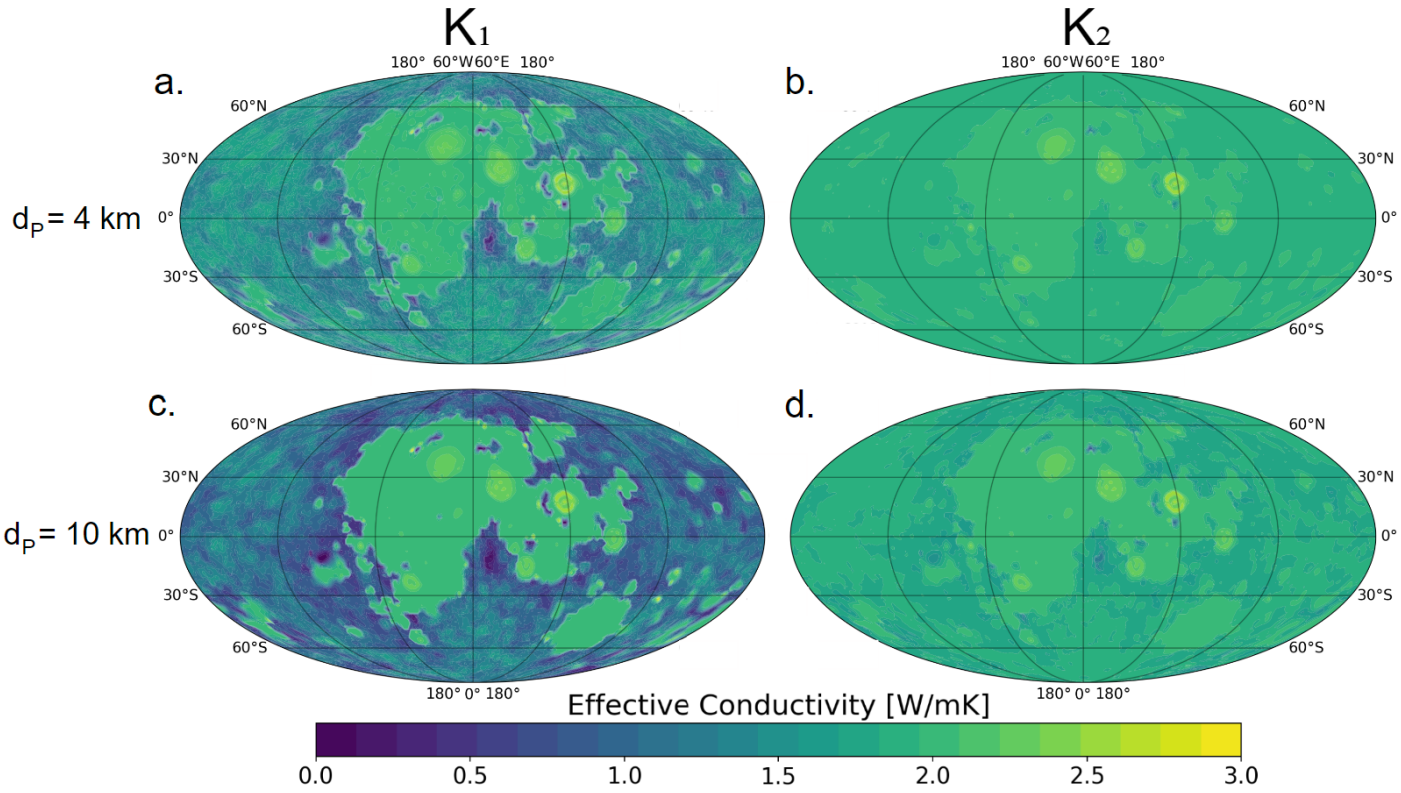

Figure 1.4: Effective crustal thermal conductivity maps. Areas outside of maria have been treated as the combination of a porous layer of thickness d_P and an underlying layer of anorthosite of variable thickness depending on the local crustal thickness. Maria regions have been treated analogously, with the only difference that the porous layer is substituted by a basaltic layer of variable thickness depending on the data described in section 1.5. Panels a. and c. are computed using model K_1, while b. and d. using model K_2 (section 1.4). The porous layer thickness (d_P) for each panel is given by leftmost label.

2
Results

In this section, we describe the main results obtained by including the laterally variable conductivity model onto the setup discussed in Part II. First, we focus on the findings related to the nearside KREEP region, and later we present the analysis of the thermal state of the farside FHT region. The results for the KREEP and FHT regions are focused on the different treatment of basalt-covered regions compared to highlands, as explained in Section 1.6, Equations 1.5 and 1.6.

No porous megaregolith layer is modeled underneath basalts, due to the lack of porosity data, meaning that the parameters of the porous layer (thickness and cconductivity) do not affect basalt regions. In other words, looking at Figure 1.4, the conductivity in the basalt regions is the same across all plots. Therefore, we will discuss the effect of each model in Figure 1.4 only for the FHT region. Conversely, the parameters of interest for the KREEP region are the average KREEP region thermal conductivity, which we vary in the range ~1.6-2 W/(mK), as well as the combination between size and HPE enrichment of the KREEP layer (Part II - Figure 4). Lastly, as discussed in Part II - Discussion, all models shown in the following section are characterised by a KREEP layer below the crust. This choice was made because a KREEP layer located below the crust largely affects the viscosity at the crust-mantle interface .

In the following sections, we identify as basalt or basalt-covered regions the surface areas of the Moon characterized by the absence of porosity data (Figure 1.1) and discussed in Section 1.5. Conversely, when describing or discussing the KREEP region, we refer to the region described in Part II - Method, which is located within the basalt-covered regions. Lastly, in this case we use the FHT region denomination to identify all locations where porosity data are plotted in Figure 1.1. This note is meant to avoid confusion with the naming of the various terranes, but the terminology used here is consistent with all previous sections.

2.1. KREEP Region

In the following paragraphs, we describe the effects of including our conductivity model onto our preferred models from Part II, with a focus on the KREEP region. We will show the results obtained for our Reference model with KREEP below the crust (i.e., the model described in Part II - Figure 4d), and for the two end-member models for KREEP geometry-enrichment (i.e., models in Part II - Figure 4b). In addition, we display the two end-member models corresponding to our average KREEP region conductivity range of ~1.6–2 W/(mK).

Firstly, we describe the effects of a laterally variable thermal conductivity on the interior temperature distribution below the KREEP region (Figure 2.1). The left panel in Figure 2.1 shows our Reference KREEP below the crust model that differs only in terms of crustal thermal conductivity compared to the right panel. The only prominent feature in the plot is the KREEP thermal anomaly, and the main effect of our thermal conductivity model is to decrease the intensity of such anomaly while the heat flux at surface remains unchanged. In particular, the maximum temperature variation attained in the reference

case is about 635 K, while it reduces to about 450 K using a variable thermal conductivity. This is explained by the average KREEP conductivities between the two models: we compute the surface heat flux as $H = k \cdot \nabla T$, where k in our Reference model is constant with a value of 1.5 W/(mK), wheras in the right panel of Figure 2.1, for the laterally variable k, the average KREEP conductivity lies at about 2 W/(mK). A higher thermal conductivity decreases the thermal gradient in the subsurface compared to a lower k. Since the surface heat flux is similar in both cases, the thermal gradient in the variable crustal thermal conductivity case decreases to 75% of its value in the Reference case, which leads to the temperature decrease between the two panels in Figure 2.1.

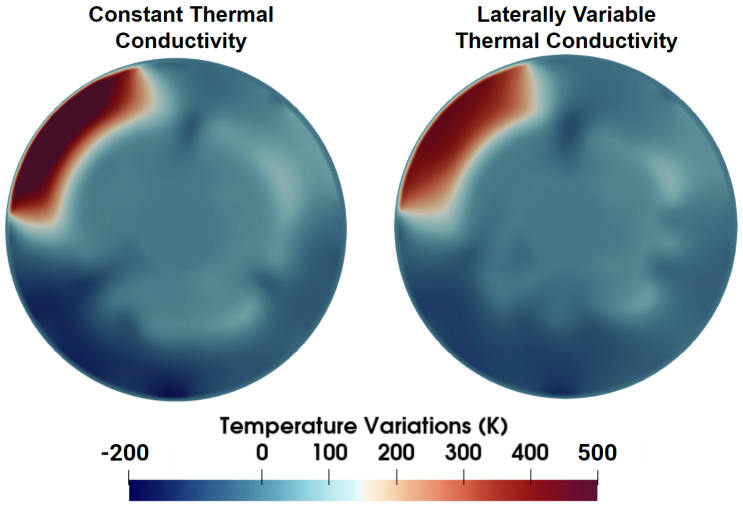

Figure 2.1: Interior distribution of present-day temperature variations about an average depth-wise temperature profile. The panel on the left shows a cross section of the Moon (160°E/340°E longitude great circle) where the KREEP thermal anomaly is the only prominent feature. On the right, an analogous cross section, with the only difference of being computed including a laterally variable thermal conductivity model (K1 model with 4 km porous layer, Section 1.6).

The same effect can also be visualized in terms of thermal profiles below the KREEP region (Figure 2.2). In the plot, the effect of different average conductivity values on the subsurface thermal anomaly is immediately visible, with a decrease in the subsurface temperature spike for increasing conductivity values. It must be noted again that throughout these different simulations, the heat flux at the surface remains unchanged from its values shown for our reference case, making these different simulations equally consistent with the heat flux constrains mentioned in Part II.

We now move to the analysis of the effects of a laterally variable thermal conductivity model on basin relaxation constraints, as described in the first paragraphs of Section 2 (Ding & Zhu, 2022). We are mainly interested in evaluating the viscosity values at the crust-mantle boundary and at 0.5 Ga from the beginning of the simulation (4 billion years ago), as a proxy for the time of major basins formation. It should be kept in mind that we use a laterally variable crustal thickness, meaning that the crust-mantle interface sits at about 30-40 km on the nearside, while being about 70-80 km thick on the farside (Part II - Figure 1). The viscosity profiles for a set of simulations are shown in Figure 2.3.

Firstly, it should be noted how the difference between the reference case (solid light blue curve) and the simplest version of a laterally variable thermal conductivity case (k_{Avg} = 2 W/(mK), solid turquoise curve) is large, with almost two orders of magnitude increase in viscosity at 100 km (7^{18} for the Reference and 10^{20} Pa s for k_{Avg}= 2 W/(mK)). This is due to the effect of the larger thermal conductivity in the latter case (about 2 W/(mK) compared to the 1.5 W/(mK) Reference), which lowers the subsurface temperature anomaly. Secondly, in Figure 2.3 we can observe that the effect of varying the average conductivity in the KREEP region is significant, and consistent with what was found for Figure 2.2. In this case, a k_{Avg} similar to our reference k_{Const} = 1.5 W/(mK) lowers again the viscosity to a value of $2{\cdot}10^{19}$ Pa s at 100km. Lastly, the effect of KREEP size-enrichment combination is likely the dominant effect shown in Figure 2.3. As mentioned in Part II - Discussion, a small-sized higher enriched KREEP

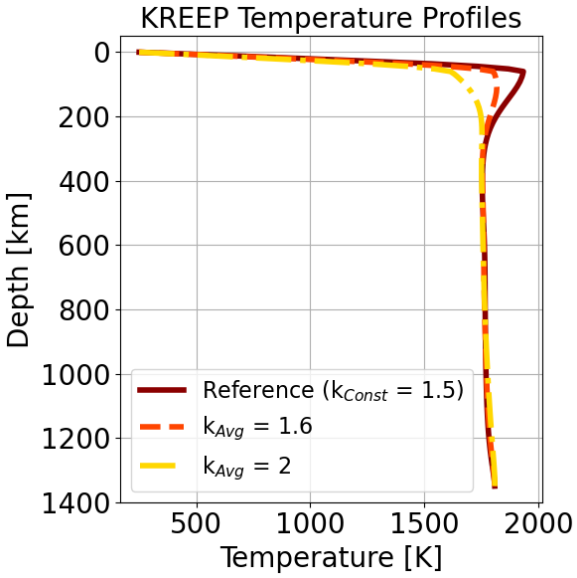

Figure 2.2: Thermal profiles as a function of depth for three different simulations, computed at 4 Ga ago. All simulations share a KREEP located below the crust, which is visible from the temperature increase in the first 100km depth. Our reference case (solid dark red curve) is characterized by constant crustal conductivity (k_{Const}) of 1.5 W/(mK). The remaining two curves represent simulations with laterally variable thermal conductivity and differ by the average KREEP region thermal conductivity value (k_{Avg}). k_{Avg} values of 1.6 W/(mK) (orange dashed curve), and 2 W/(mK) (yellow dashed curve) correspond to our endmember cases.

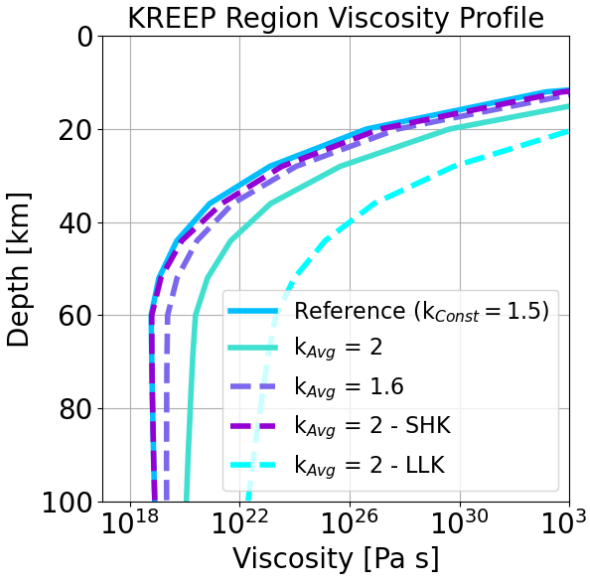

Figure 2.3: Viscosity profiles in the first 100 km of depth, computed at 4 Ga ago for 5 different simulations. Our reference case (solid light blue curve) is characterized by constant crustal conductivity (k_{Const}), while all other simulations are computed using our laterally variable thermal conductivity model. The solid turquoise curve represents a simulation where the variable conductivity is the only difference with respect to the reference. The dashed light purple curve differs from the former in terms of the average thermal conductivity value in the KREEP region (k_{Avg}). The remaining two dashed lines (dark purple and light blue) differ from the k_{Avg} = 2 W/(mK) simulation in terms of size and enrichment of the KREEP region: the former has a smaller-sized, higher enriched KREEP (SHK, described in Part II - Discussion), while the latter has a larger-sized lower enriched KREEP (LLK, described in Part II - Discussion)

layer (SHK) largely increases the subsurface temperature anomaly, hence causing a strong decrease in viscosity (roughly two orders of magnitude between k_{Avg} and k_{Avg} - SHK). Similarly, the effect of a large-sized low enrichment KREEP is noticeable in the plot ($3{\cdot}10^{22}$ Pa s at 100 km). For the SHK and

LLK models, it should be also kept in mind that, since the geometry and HPE enrichment in the KREEP is changing, so is the distribution of heat flux on the surface, according to the description of Part II - Figure 3, meaning that these two cases do not share the same heat flux at our locations of interest with the reference model, as opposed to the four models in Figure 1.4.

2.2. FHT Region

Moving on to the analysis of the thermal state below the FHT region after the implementation of the laterally variable thermal conductivity model, we can initially describe the interior temperature distribution throughout the same cross section shown in Figure 2.1. This is shown in Figure 2.4, where the diagrams appear inherently different only due to a different saturation of the colormap, which is necessary to capture temperature contrasts in the FHT compared to KREEP region. What is immediately noticeable in Figure 2.4 is that the secondary thermal anomaly below FHT is smaller in size and slightly weaker for our variable conductivity model with respect to the reference case. This is again due to the higher value of average conductivity, which attains values around 1.9 W/(mK) below FHT region in the right panel of Figure 2.4.

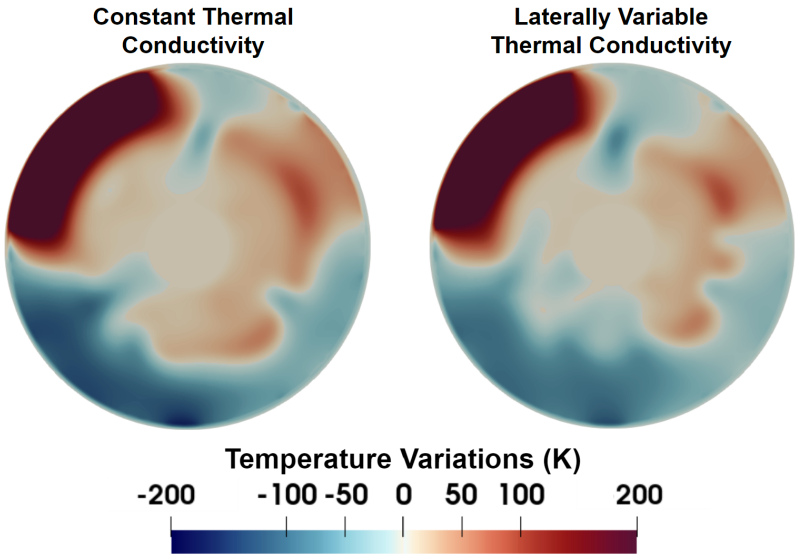

Figure 2.4: This figure shows the same results displayed in Figure 2.1, with the only difference being the color stretch. This is necessary to visualize the FHT region differences in temperature, which are invisible in the previous figure, and vice-versa for KREEP thermal anomaly contrast.

We now move on to the effects of using the four different thermal conductivity models described in section 1.6, and displayed in Figure 1.4. We will firstly describe their differences in terms of temperature profiles below the FHT region, with respect to the reference model (k_{Const}) in Figure 2.5. Firstly, we can observe how the K_1 - 4 km model appears having an almost coincident temperature profile with respect to the reference case, due to a very similar average conductivity in the FHT region (1.57 for K_1 - 4 km and 1.5 W/(mK) for the Reference). In addition, we see the effect of the nonlinearity in the equivalent conductivity relation (Eq. 1.5), with the porous layer thickness having much stronger influence for K_1 cases (lower k on average), while being almost insignificant for K_2, where the average porous layer k value is closer to the bulk anorthosite value (Figure 1.2). Lastly, Figure 2.5 provides yet another perspective into the general relation between crustal k and subsurface temperatures. For crustal k values above the Reference 1.5 W/(mK) (green curves) the interior loses heat more efficiently (T-profiles lower than reference), while values below the reference trap more heat and keep the interior warmer (K_1 - 10 km curve).

To conclude, we provide the viscosity profiles corresponding to the temperature profiles in Figure 2.5, in Figure 2.6. We note that in this region, the depth at which the crust-mantle interface occurs is about 75 km. In Figure 2.6, similar to what described for Figure 2.5, K_1 model with a thin porous

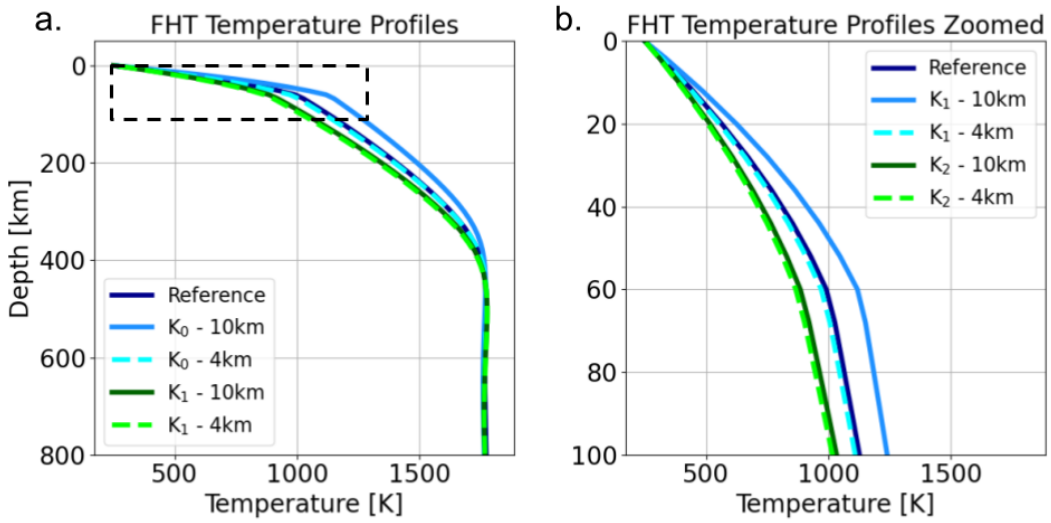

Figure 2.5: Depth-wise temperature profiles below FHT region at 4 Ga ago, for the different thermal conductivity models shown in Figure 1.4 with respect to a constant crustal conductivity reference case (dark blue solid curve). Panel b. corresponds to the portion of panel a. enclosed in the black dashed box, and otherwise analogous. The depth is only displayed until 800 km in panel a. and 100 km in panel b. for ease of visualization. All profiles in panel a. continue until CMB. The dashed curves represent models where the global porous layer is 10 km thick, while solid curves correspond to a 4 km thick layer. K_1 (shades of blue) and K_2 (shades of green) identifiers refer back to the porosity to conductivity models described in section 1.4. K_1 models yield average conductivities in the range 1.25-1.55 W/(mK), while K_2 yield values between 1.85 and 1.93 W/(mK)

layer shows negligible differences with respect to the reference (order of 10^{24} Pa s at 100 km), while the corresponding thick porous layer model differs largely (one order of magnitude lower), due to its higher temperature profile. Alternatively, the K_2 models (green curves) show two orders of magnitude increase in viscosity at 100 km with respect to the reference (order of 10^{26} Pa s), while being almost equivalent between one another, consistent with Figure 1.4.

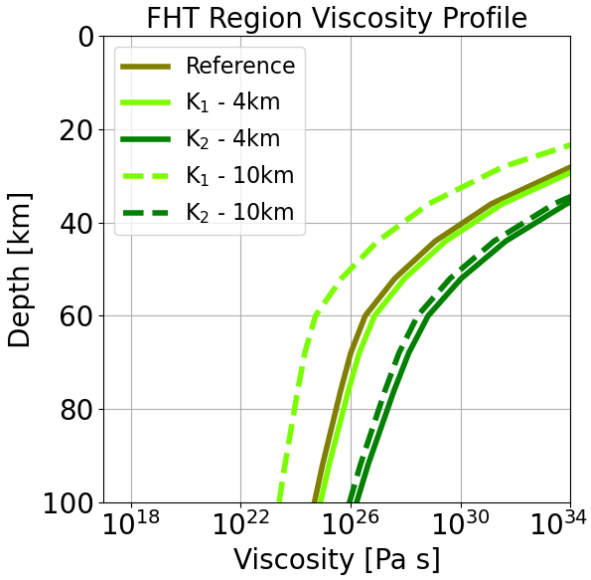

Figure 2.6: Viscosity profiles below FHT region at 4 Ga ago, shown until a depth of 100 km. The solid olive green curve represents the reference case. Dashed curves correspond to a 10 km thick porous layer, while solid lines to a 4 km thick one. Light green curves correspond to K_1 model, while dark green ones to K_2, as described for Figure 2.5 and in section 1.2.

3

Discussion

Following the structure of Section 2, we will firstly discuss the findings related to the effect of our lateral thermal conductivity models on the KREEP region. Subsequently, we will procede with the FHT region in an analogous way.

3.1. KREEP Region

The main effect of modeling the thermal conductivity in the KREEP region as equivalent to a layer of compact basalt (k_B = 2.6 W/mK, Halbert and Parnell, 2022) on top of a compact anorthositic layer (k_b = 1.6-2 mW/mK, Henke et al., 2016) is to increase the crustal conductivity in the KREEP region compared to the Reference case (1.5 W/mK). This causes a more efficient heat loss to space and a weaker present-day thermal anomaly below the KREEP region, with a maximum temperature of ~450 K compared to the ~635 K in the Reference case. A weaker thermal anomaly corresponds to a proportionally weaker density anomaly, which is beneficial to explain the absence of a significant gravity anomaly associated with the KREEP region (Laneuville et al., 2013).

Varying the average KREEP region conductivity within the mentioned range (k_{Avg} = 1.6 - 2 W/(mK)) has important effects (Figures 2.2 and 2.3). This has the effect of changing the shape of the thermal profiles below the KREEP center (Figure 2.2), with the spike in temperature associated with the presence of KREEP below the crust (40-60 km in depth) decreasing for increasing k_{Avg}. The presence of a spike in temperatures 4 Ga ago is consistent with the findings in Hiesinger et al. (2023) and Shearer et al. (2023), which suggest a peak in magmatic activity relatively early in lunar history (3.8-3.2 Ga). Therefore, we favour the endmember model with k_{Avg} = 1.6 W/(mK).

Moving on to the discussion of the viscosity profiles (Figure 2.3), our aim is to match the conditions for complete annulus relaxation of basins, as provided in Ding and Zhu (2022):

- Viscosity values < 10^{19} Pa s at crust-mantle interface
- Surface thermal gradient values > 30 K/km at crust-mantle interface

Looking at the models in Figure 2.3, we favour the laterally variable conductivity model with lower thermal conductivity in the KREEP region (k_{Avg} = 1.6 W/(mK)), which reduces the viscosity to values of the order of 10^{19} Pa s, closer to the Reference case value of $7{\cdot}10^{18}$ Pa s. This implies that the effective thermal conductivity in the KREEP region is lower than both that of compact basalts and compact anorthosite. Hence, it is likely that either mare basalts are characterized by their own non-negligible porosity, as volcanic products, or that a more complex layering of volcanic material and regolith-like ejecta dominate the region's conductivity, or a combination of both effects. However, thermal gradient values for the k_{Var} = 1.6 W/(mK) attain values of about 35 K/km in the KREEP region, consistent with the relevant constraint in Ding and Zhu (2022).

In addition, Figure 2.3 shows the results of applying the k_{Avg} = 2 W/(mK) thermal conductivity model to the different KREEP size/enrichment scenarios in Part II - Figure 4a,b. As previously discussed for

constant thermal conductivity models (Part II - Discussion), the SHK (Small, Highly enriched KREEP) model matches best the viscous relaxation conditions by Ding and Zhu (2022), with a viscosity of the order of 10^{19}-10^{18} Pa s at 40-60 km depth, and a KREEP region thermal gradient of ~40 K/km. This is mainly due to the higher KREEP enrichment of the SHK model. However, the small size of KREEP in this case (cutting at about half of Imbrium basin) is not consistent with the basin relaxation data from a geographical perspective. In Ding and Zhu (2022), it is argued that at least as far as mare Serenitatis basins annuli are viscously relaxed. In order to have a KREEP region extending underneath Serenitatis, with viscosities comparable to those of our SHK model, the consistency with surface heat flux distribution would be disrupted. Therefore, a more complex KREEP region geometry and treatment of its properties may be needed, possibly including a pressure and temperature dependent thermal conductivity in the crust.

3.2. FHT Region

As opposed to the KREEP region, crustal annuli are not relaxed on the farside highlands, meaning that the related conditions provide opposite bounds in terms of viscosity and thermal gradient (Ding & Zhu, 2022):

- Viscosity values > 10^{26} Pa s at crust-mantle interface
- Surface thermal gradient values < 20 K/km at crust-mantle interface

Our Reference case is only consistent with the thermal gradient constraint, having FHT viscosity values below 10^{26} Pa sat 80 km depth and surface thermal gradients of the order of 17 K/km (Figure 2.6). Thus, we favour K_2 models, both of which show viscosities above 10^{27} Pa s at 80 km depth. In addition, the two K_2 models are also characterized by colder thermal profiles (Figure 2.5) and surface thermal gradient values of about 15 K/km.

Favouring the K_2 models has two main implications for the understanding of lunar crustal structure. Firstly, as opposed to what discussed for the KREEP region (Section 3.1), a higher conductivity on average is required to lower the temperatures below the FHT region. Hence, the K_2 model, which is characterized by higher conductivities (Figure 1.2) appears more realistic. This result is somewhat counterintuitive, since the presence of a thick basalt layer on the nearside and highly porous material on the farside would suggest higher conductivity in the former and lower conductivity in the latter region. However, we find favourable the model that has relatively higher conductivity on the farside and lower on the nearside. Secondly, for the K_2 models, the influence of the porous layer thickness is not large (Figures 2.5 and 2.6), and favouring the thin porous layer still.

3.3. Crustal Properties

In the present section of this study, we addressed the following research question:

Can present-day lunar heat flux and crustal thickness constrain megaregolith layer thickness and thermal conductivity of lunar crust?

In particular, heat flux and crustal thickness are translated to thermal gradient and crustal annuli structure through our laterally variable thermal conductivity model configuration. Concerning the megaregolith layer thickness, assuming that our K_1 model is representative lunar subsurface (Figure 1.2; Henke et al., 2016), we exclude the presence of a porous layer as thick as 10 km. This is due to the exceedingly low viscosity of the K_1 - 10 km model at crust mantle boundary (~80 km depth in Figure 2.6). Conversely, a porous layer of about 4 km thickness is consistent with the findings of Ding and Zhu (2022).

Assuming that the K_2 linear model in Figure 1.2 is representative of lunar subsurface, we see a poor correlation between porous layer thickness and crustal thermal conductivity. This is shown by the similarity between the two rightmost maps in Figure 1.4b,d. However, the K_2 models show a viscosity

of about 10^{28} Pa s at crust-mantle interface, which is more consistent with the results of Ding and Zhu (2022) for completely unrelaxed basins. From this, we can conclude that, for a K_2 model, even if a porous layer up to 10 km thick exists, it does not influence the crustal thermal conductivity. We find a best fit for ~2 W/(mK), typical value for compact anorthositic material. Therefore, when modeling FHT crust, this layer behaves more like a compact anorthositic slab rather than a highly porous megaregolith layer underlain by anorthosites in terms of thermal conductivity.

Concerning the basalt-covered regions, we expected to see a best-fit for thermal conductivities higher than the 1.5 W/(mK) value previously assumed. However, the results in Figure 2.3 show that to allow viscosities of ~10^{19} Pa s, we need effective conductivity closer to the initial 1.5 W/(mK) value. As previously mentioned, this implies either high-porosity basaltic material or a behaviour dominated by a more complex stratified structure of basalts and regolith material.

In addition to the aforementioned possibilities, the effect of a temperature and pressure dependent thermal conductivity must also be discussed. According to parameterizations such as that in Tosi et al. (2013), thermal conductivity decreases with temperature and increases with pressure. Therefore, this effect could also lower the thermal conductivity values in regions characterized by high temperatures close to the surface, such as the KREEP region. In this case, it would be possible to comply with the viscosity constraints in Ding and Zhu (2022) even with basaltic material having conductivity in excess of 2.5 W/(mK).

3.4. Outlook

There are several possibilities to increase the complexity of our thermal evolution model setup. One additional step is to include an explicit treatment of melting, which allows a quantitative estimate of melt produced, melt tracking and analysis of different magmatic styles (i.e. different extrusive to intrusive melt ratio and depth of intrusive melt entrapment). This would also allow us to assess the robustness of the model in reproducing realistic amounts of extrusive melts across different lunar terranes, expanding on the results of Laneuville et al. (2013, 2018).

Tidal deformation constitutes another independent constraint that can be taken into account in the model, since accurate measurements of this quantity are available for the Moon (Williams & Boggs, 2015; Williams et al., 2014). A first-order assessment of tidal deformation can be produced as an additional post-processing step based on the present-day output of thermal evolution models; however, full treatment of tidal effects requires the computation of deformations at each simulation timestep, with subsequent feedback of the tidal energy into the system.

Additionally, seismic analyses also provide independent constraints on the present-day thermal state of the Moon (Kawamura et al., 2017). In particular, seismic velocities modelled at shallow depths on the nearside can constrain the temperatures below the KREEP region, whereas the depth and spatial distribution of deep moonquakes place strong constraints on lower mantle temperatures, which should not exceed the brittle-ductile transition temperature (~1300 K, Kawamura et al., 2017).

On the other hand, without having to increase the complexity of the present thermal evolution model setup, it can be coupled with the crustal thickness model by Broquet and Andrews-Hanna (2024a). This would require to update the crustal thickness model using the results of a chosen best-fit thermal evolution model and re-initializing the same thermal evolution with an updated crust, until a convergence is potentially found. Such an iterative approach applied to global scale thermal evolution modeling has never been proposed, prompting us to investigate its effects on our results.

Lastly, it is crucial to anchor the initial conditions of the present setup combining it with data coming from LMO crystallization models. One important characteristic of global scale models is a relatively poor radial resolution, due to its dominant impact on the computational expense. Therefore, all analyses of KREEP layer thickness and radiogenic enrichment are approached by diluting the HPE in thicker layers (10-30 km with 3-6 ppm thorium) equivalent to thin, highly enriched KREEP layers (<10 km with 12-18 ppm thorium), consistent with surface thorium measurements (Figure 1.3, Lawrence et al., 1999). 1-D LMO crystallization models predict thicknesses and enrichment of the KREEP of 1.6-2 km and 18 ppm

thorium, assuming a global, constant thickness layer. Reproducing these results for a global KREEP extent in our model and evaluating the divergence of nearside heat flux values compared to the Apollo measurements can provide insight into the concentration of HPE below the nearside. Potentially, this investigation can produce new evidence to explain the nature of the anomalous nearside thorium observations, whether caused by an asymmetrical interior distribution of HPE or due to the farside structure inhibiting their surface exposure.

4

Verification and Validation

In the following sections, we will describe the methods used to verify and validate all results obtained during the present study. Firstly, we will focus on the verification, that is, ensuring that the results obtained are not affected by uncertainties arising from method choices or software tools used. Thereafter, we will move to Validation, which means demonstrating how our setup accomplishes its intended purpose of consistently modeling lunar thermal evolution. In other words, we will use our tools to reproduce other models and results from literature, thereby ensuring the fidelity of our methods and the repeatability of our results.

4.1. Verification

In the present section, we will provide the results of sensitivity analyses on the effect of initial temperature profile, reference viscosity and grid resolution on our results. Subsequently, we will move to post-processing code verification, where we will show the strategies put in place to ensure the robustness of results against errors in the coding pipelines.

4.1.1. Sensitivity Analysis

Initial Temperature Profile

Firstly, we focus on the choice of the initial temperature profile, which corresponds to the initial condition for the temperature field, meaning one temperature value for each domain cell. This information is fed to the software as a 1D average temperature profile to assign to the initial time-step. From a physical perspective, it is particularly complex to constrain the interior temperature distribution upon crystallization of the magma ocean, since the first stages of evolution are still poorly understood. However, thanks to the ”thermostat” effect, described in section 2.3.1, this choice has negligible effects on the present-day state of the system. The feedback effect between viscosity and temperature buffers oscillations and lets different initial conditions converge towards similar ”equilibrium” conditions.

In order to quantitatively assess the influence of initial temperature profile on the thermal evolution, we tested three different conditions, namely a ”cold”, ”intermediate”, and ”hot” case. The specific profile choices are based on the three cases provided in Laneuville et al. (2013), and repeated in figure 4.1

In our case, the initial temperature profiles is simplified, meaning that we define it as a 3-layered piece-wise linear function. Therefore, we only input 4 quantities to define a profile: temperature and radius at the interface between the upper thermal boundary layer and the adiabatic layer, and analogously for the lower thermal boundary layer. Surface and CMB temperatures are already set through the boundary conditions (section 2.1.4). Nevertheless, we approximated the the three profiles in figure 4.1, under our simplified conditions, and evaluated their influence on present-day thermal state (figure 4.2).

Looking at figure 4.2, the feedback effect is immediately noticeable. For our cold case, the temperature in the lower mantle increases with time, opposite to the hot case and somewhat counterintuitively,

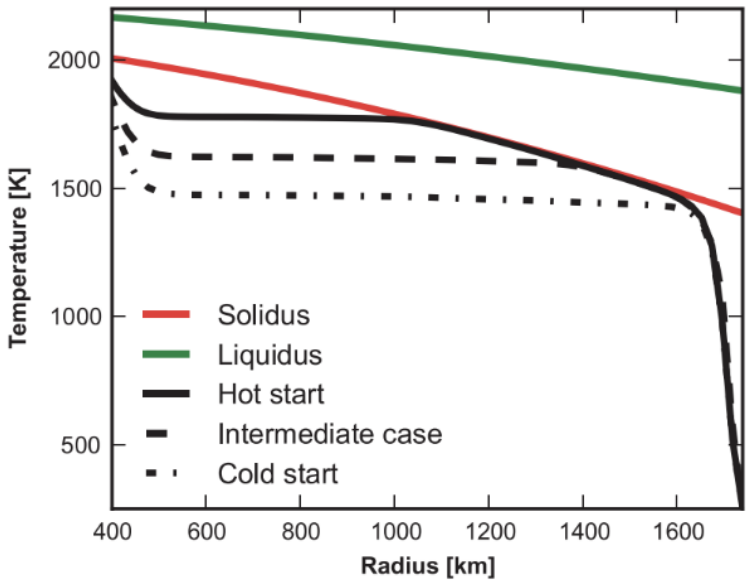

Figure 4.1: Initial temperature profiles from Laneuville et al. (2013), where the surface corresponds to 1740 km in radius and a temperature of 250 K. The three initial temperature profiles used in this case (curves in black) are more complex than what assumed in the current study, having the same thermal gradient in the first ~100 km and then following the mantle solidus (red curve) to different depths before becoming adiabatic.

to reach a temperature similar to our intermediate guess. Therefore, starting from a mean mantle temperature difference of about 200 K (~12%), we find mean and maximum present-day differences of about 50K and 100K, respectively (~4 and 7.6%).

In terms of our primary observable, surface heat flux, we find a similar difference, consistently lower than 10% and within 1 mW/m^2 across all lunar terranes. We consider differences up to 1 mW/m^2 acceptable, as differences below this threshold can not be satisfactorily distinguished from numerical noise. Surface heat flux values at the locations of most interest to the present study are summarized in table 4.1:

	Cold Start	Reference Case (Intermediate)	Hot Start
Apollo 15	16	17	18
Apollo 17	10	11	12
KREEP	29	30	31
Region 5	11	12	12
FHT	14	14	15
Average	13	14	15

Table 4.1: Present-day surface heat flux values, in mW/m^2, at 5 locations of interest: Apollo 15 and 17 landing sites, KREEP center, Region 5, and Farside Highlands Terrane. In addition, the last row represents average surface heat flux values. Each column correspond to a simulation with different initial temperature profile.

Reference Viscosity

Another parameter that is highly unconstrained in planetary interior modelling is the reference viscosity Breuer and Moore, 2015. This parameter corresponds to the viscosity of mantle material at a reference temperature and pressure, and is usually taken to be equal to that of dry olivine (1e21 Pa s). In most

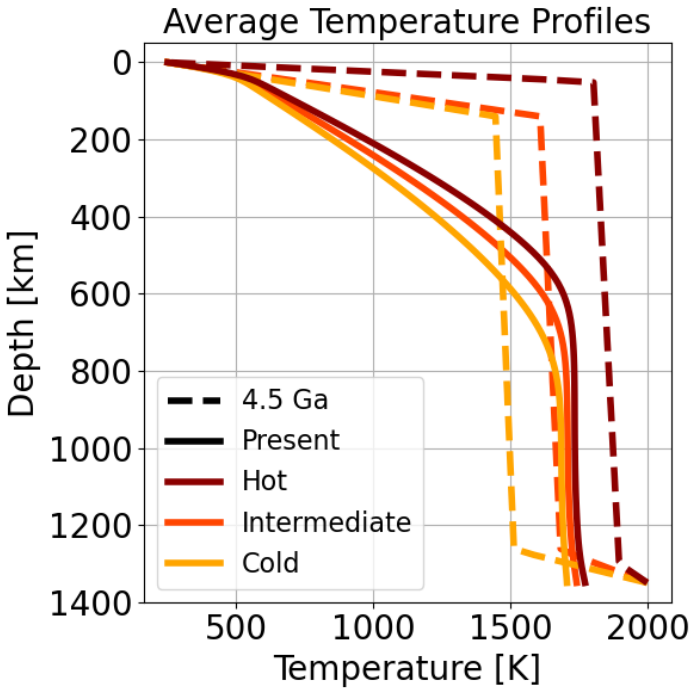

Figure 4.2: Initial average temperature profiles, and corresponding present-day profiles, for cold, intermediate and hot start cases. Dashed lines show initial profiles, and solid lines are at present day.

cases, olivine is assumed to dominate the rheology of silicate mantles. However, small differences in mantle composition or volatile content can cause reference viscosity shifts orders of magnitude strong. For example, a difference of ~9 wt% FeO between Earth and Martian mantle causes a reference viscosity difference of a factor 10 Breuer and Moore, 2015. Similarly, water-saturated olivine has reference viscosity two orders of magnitude lower than under dry conditions Tosi et al., 2014.

In the case of lunar mantle, both composition and water content remain highly debated, introducing a possible source of uncertainty if a model is not robust to changes in reference viscosity. To this end, we performed a similar investigation to what described in the previous section for initial temperature profiles. The present-day average temperature profiles resulting from three simulations characterized by different reference viscosity values are shown in figure 4.3

As can be noted from figure 4.3, the effect of having different reference viscosity values is preponderant in lower mantle (above 600 km), with a lower viscosity value causing better mixing and a more efficient cooling of the lunar mantle. Vice-versa, a higher reference viscosity lowers convective vigor and causes a warmer present-day deep mantle. However, temperature differences at surface are not appreciable in figure 4.3, suggesting that heat flux values are only negligibly different. Indeed, surface heat flux values across the three simulations in figure 4.3 show values less than 0.5 mW/m^2 different for all locations of interest.

Grid Resolution

The grid resolution chosen for our models can also have important undesired effects on the outcome of our simulations. Since all our models share the same grid, any bias arising from it would not be detectable unless a test is performed. Therefore, we produced a higher resolution (finer grid) version of our reference case (Part II - Figure 2b), to ensure that all results are independent of the grid resolution.

Our reference grid geometry is that of a full spherical shell (an example is shown in figure 4.4), and the cross section of each cell is a circular corona sector. The nodes are distributed in a radial geometry, meaning that all nodes in a depth-wise profile lie on the same straight line. A peculiarity of our grids is that throughout the first ~80 km (maximum crustal thickness) the resolution is higher than the rest of the mantle. This is done to capture crustal thickness variations, which would otherwise be too coarsely

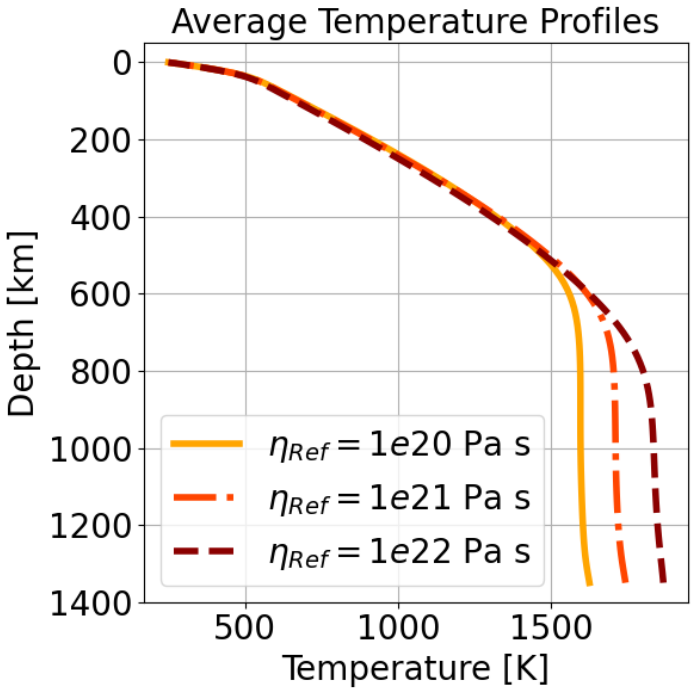

Figure 4.3: Present-day temperature profiles for three simulations characterised by different reference viscosity (η_{Ref}) values.

represented and, thus, unrealistic. For our reference grid, we have a resolution of 8 km in the first 80km and 16 km at greater depths. For our more refined grid case, we have a resolution of 4 km in the crust and 10km deeper.

Let us now look at the results comparison between reference (Ref) and high resolution (HR) grid. Firstly, we display the average temperature profiles of the two simulations throughout the evolution, to show their continuous agreement in time (figure 4.5).

Figure 4.5 shows perfect agreement (indistinguishable difference) between the two simulations at all times and depths. This implies that increasing the grid resolution does not affect our average temperature distribution and, possibly, suggests that there is room for optimization using an even less refined grid. However, the latter statement would require an extensive test campaign to be demonstrate, which was not within the scope of the present project.

In addition to the average profiles, which do not capture any lateral variations of temperature throughout the domain, we provide a cross section of the full 3D temperature field as further proof (figure 4.6). The cross section on display cuts through the KREEP region and FHT, roughly at the 160°/340° longitude great circle.

Figure 4.5 also shows sufficient agreement between the two simulations, keeping the planform of convection and distribution of local minima and maxima unchanged. However, the two cross sections are not identical, showing slight differences at the edges of upwellings and downwellings, showing that the higher resolution grid better captures steep thermal gradient regions, as expected. In order to quantify the small differences in the temperature distribution, we can once again use present-day surface heat flux values, as thy represent the quantity we are most interested in. Across the five regions in table 4.1, plus surface average heat flux, we find differences consistently lower than 0.5 mW/m^2.

4.1.2. Code Verification

The main software used in the present study (Gaia) was not developed nor modified within the project scope. This code is specifically designed for simulating planetary mantles, and has been verified and validated across multiple publications (e.g. Hüttig and Stemmer, 2008b; Plesa et al., 2013). However,

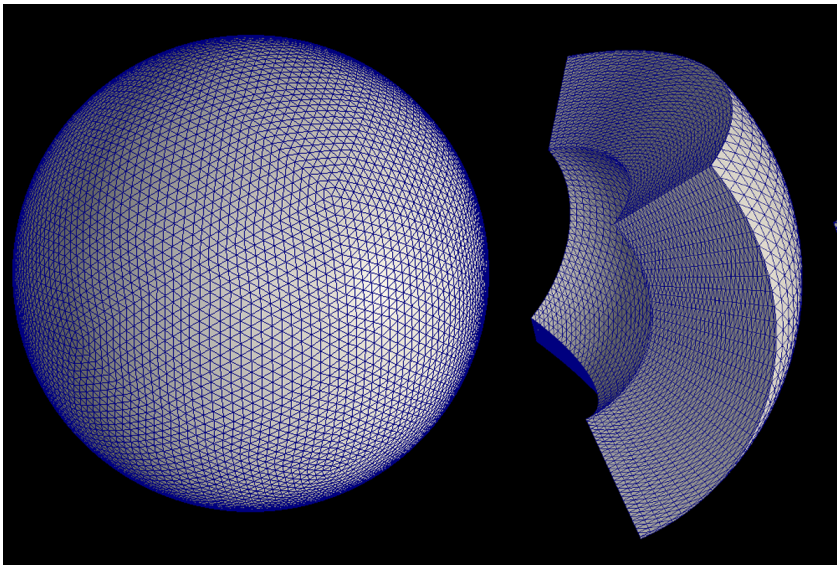

Figure 4.4: Visual representation of a finite volume spherical shell grid (left) and an example cutout (right), analogous to the geometry used in the present study. The picture was taken from Plesa et al. (2016).

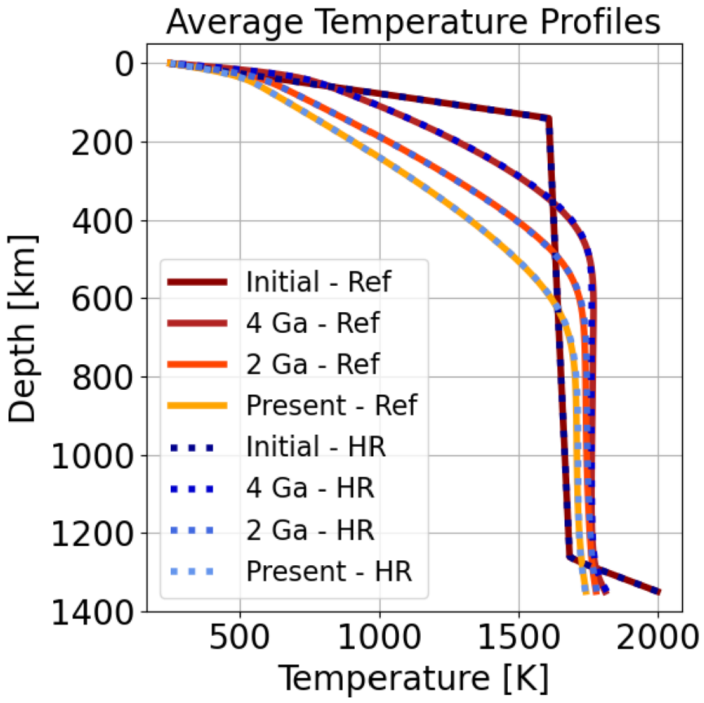

Figure 4.5: Average temperature profiles at different times throughout the evolution, for a reference grid case (Ref, red palette), and a higher resolution grid (HR, blue palette).

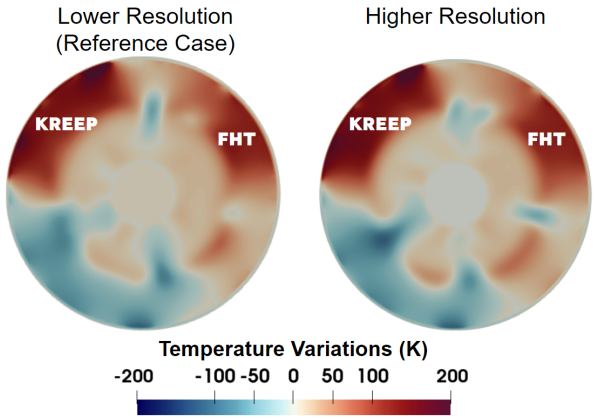

Figure 4.6: Temperature variations on a cross section of the spherical domain (160°/340° longitude great circle). The variations are computed about the local shell (depth) average, meaning that they represent the local difference with respect to the average temperature profile. The temperature distribution is saturated upwards for better representation (true minimum and maximum values are -110 and 280, respectively). The KREEP and FHT identifiers refer to the local surface terrane.

multiple post-processing codes have been used and developed during the current project, with the aim of performing specific analyses characteristic of the model setup.

Therefore, a substantial part of our verification strategy is based on ensuring that all post-processing codes are fully functional and accurate, meaning that they produce the desired output without introducing additional sources of bias and error. To this end, it should be noted that the Gaia code works in cartesian coordinates, while all post-processing codes and additional datasets (crustal thickness, porosity, conductivity maps) are stored in regular latitude-longitude coordinate systems. Thus, one of the aspects to be verified is a correct interpolation of the Gaia-cartesian grid onto a spherical coordinate grid.

Furthermore, potential error sources can be related to the computation of quantities such as surface heat flux, either as a bidimensional map or as an average surface value, or, similarly, temperature distributions and profiles. In addition, a correct reading of the input crustal thickness and conductivity datasets in Gaia should be verified. In the following paragraphs, we will provide a brief description of the verification methods employed.

Two main concepts have been employed throughout the work to verify all analyses, namely: software independence and redundancy. With the former concept, we mean that in addition to using python scripts developed specifically to analyse our Gaia outputs, we used an external general purpose software (ParaView), independently verified, to run sanity checks and inspect the correct interpretation of the outputs. On the other hand, redundancy is ensured by building some degree of overlap between the various python codes. This means that flag quantities, such as heat flux at specific locations or surface average heat flux, are computed in several codes, using different approached, and checked to ensure consistency.

4.2. Validation

In the current section, a summary of how we validated our setup against previous modeling results. Firstly, we will focus on reproducing the results obtained in Laneuville et al. (2013, 2018), which represent the most comparable example of lunar thermal evolution modeling. Thereafter, we will show the consistency of our model with two more studies, characterised by completely different approaches, namely: Siegler and Smrekar (2014) and Warren and Rasmussen (1987).

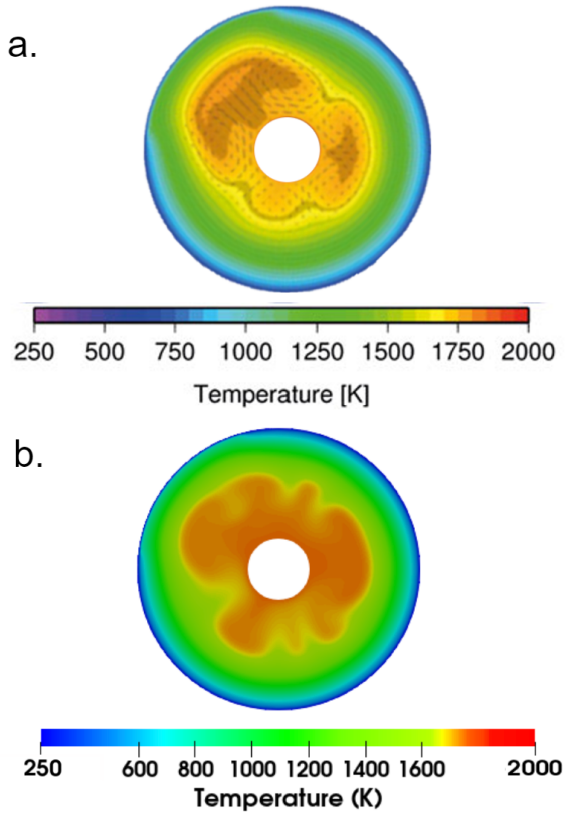

Figure 4.7: Panel a. shows a cross section of the present-day temperature distribution resulting from model 0LW (Laneuville et al., 2013). Panel b. shows the same cross section corresponding to a model produced with our setup, characterised by the same input parameters as model 0LW, except for a slightly more enriched KREEP and crust.

4.2.1. Thermal Evolution Models

Part of the motivation for this study is to improve and expand on the results of Laneuville et al. (2013, 2018). Thus, the initial benchmark used in the present study is model 0LW from Laneuville et al. (2013). We reproduced model 0LW keeping all parameters equal to those used in the original work, including a constant 39 km crustal thickness. However, because of the specific location of the KREEP layer in our setup, with Apollo 15 landing site being exactly on its edge and Apollo 17 outside of it, our reference model has a slightly more enriched KREEP and crustal layer to match the Apollo heat flux values (1.22 and 0.2 ppm instead of 0.82 and 0.14 ppm).

Nevertheless, we are able to reproduce all main characteristics of model 0LW, along with findings related to other model configurations explored in Laneuville et al. (2013). Figure 4.7 shows the same temperature distribution cross section, at present day, for model 0LW (a.) and the same model produced with our setup (b.). The main noticeable feature in figure 4.7 is that, although the thermal evolution is characterized by the instability and chaotic interaction of up- and downwellings, we obtain a strikingly similar present day planform of convection. In particular, we see a main plume developing beneath the KREEP region, as expected in all models including an enriched KREEP layer, but we also see a secondary and tertiary plume, almost equally spaced within the interior. Given the differences between our methods and those used in Laneuville et al. (2013), including the explicit treatment of melting in the latter, such a consistency in temperature distribution was somewhat unexpected. The three plumes are found to have equal relative vigor and distribution in both models, constituting a first validation of our reference case setup.

Let us now move on to the discussion of surface heat flux values between the two models. We find very similar heat flux outside of the KREEP region, namely 11 mW/m^2 in our model and 10 mW/m^2 in the 0LW model. In terms of KREEP heat flux, the two models differ substantially (33 and ~26 mW/m^2,

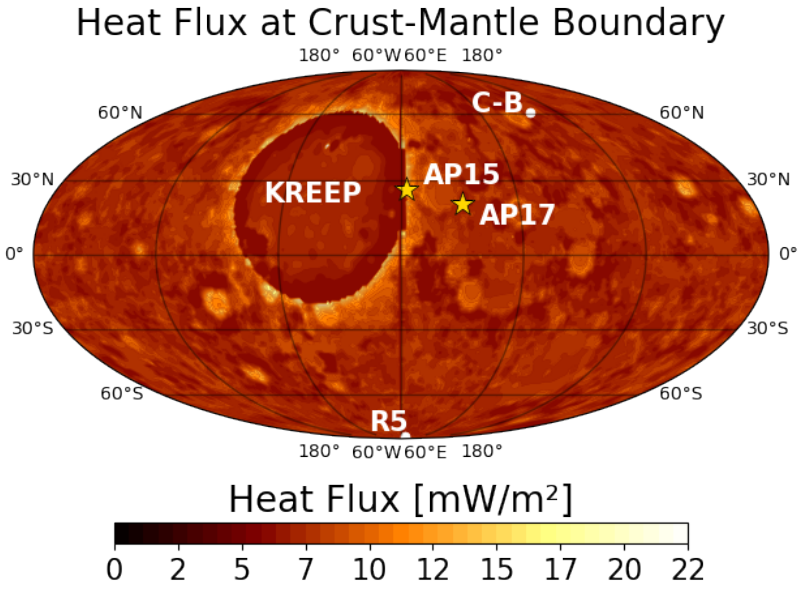

Figure 4.8: Crust-mantle boundary heat flux map computed for our reference case. We find an average heat flux of 7.3 mW/m^2 and a standard deviation of 1.3 mW/m^2. The location identifiers indicate Apollo 15 and 17 landing sites (AP15, AP17), region 5 (R5), Comton-Belkovich region (C-B) and KREEP region.

respectively), but this is mostly due to the mentioned difference in HPE distribution. In addition, we find the effects of depth-wise KREEP location to be coherent with the findings in Laneuville et al. (2013). A KREEP layer located below the crust keeps mantle temperatures higher throughout the evolution and produces a non-negligible gravity anomaly, as opposed to having a KREEP layer spread throughout the crust.

4.2.2. Regional-Scale Models

As a second step in the validation process, we consider the findings of Siegler and Smrekar (2014). In this case, we are focused on validating our treatment of crustal structure (thickness and conductivity) against a more accurate, regional scale model. In particular, the model in Siegler and Smrekar (2014) only corresponds to the Imbrium-Serenitatis region, since it includes both Apollo sites. Within this region, they use a maximum KREEP enrichment of about 12.3 ppm in a 10 km thick layer, which is comparable to our 4.5 ppm enrichment in an layer of average thickness about 30 km. They find KREEP region values about 35 mW/m^2 and outside of KREEP values between 13 and 15 mW/m^2, which are comparable to our reference case with 30 and 12 mW/m^2, respectively.

In addition, an important independent validation point comes from the computation of crust-mantle interface heat flux. In Siegler and Smrekar (2014), they find a plausible range of 9-13 mW/m^2 for the heat flux coming from the mantle in order to match the surface measurements with a KREEP layer comparable to our case. In figure 4.8, we show our reference case results for crust-mantle heat flux. We find a surface average of 7.3 mW/m^2, which is comparable while slightly lower than predicted in Siegler and Smrekar (2014). However, when zooming in on the Imbrium-Serenitatis region (20-45°N, 10°O-20°W), we find higher values that average around 8.5-9 mW/m^2, showing an almost perfect match to the prediction.

5

Conclusion

In this study, we combine a global geodynamic model of lunar thermal evolution with crustal thickness and thermal conductivity distribution models, in order to constrain their effects on the thermal history and present-day state of our satellite, as well as providing constraints on the lateral distribution of HPE within the Moon. We use surface heat flux measurements by Apollo 15 and Apollo 17 missions, LRO diviner instrument, Chang'e 1 and 2 data, and estimates from previous modeling efforts to constrain our model parameters.

In the first part of this study (Part II), we discuss the findings related to the introduction of the crustal thickness distribution model. In particular, we find that lateral crustal thickness variations influence mantle convection planform throughout the evolution, and induce surface heat flux variations in the order of 5 mW/m^2. However, this effect applies to high crustal HPE enrichments (0.5-1 ppm thorium, Jolliff et al., 2000), while becoming negligible for enrichments of the order of 0.2-0.3 ppm thorium. None of the models produced here can explain the high heat flux estimate in the Compton-Belkovich region Siegler and Smrekar, 2014, suggesting the presence of a specific and highly localized feature (e.g., a potential magmatic intrusion) in this region.

Thus, we address multiple scenarios of KREEP region size and enrichment, interpreting the different configuration based on the level of uncertainty related to each measurement. For all KREEP configurations, we favour BSM uranium abundances to be comparable to BSE (~20 ppb), or even lower. Thereafter, we find that the a large KREEP layer below the nearside (~1500 km in diameter), with an enrichment lower than 3 ppm thorium, fits best with the two Apollo measurements and Diviner estimate. A intermediate KREEP size (~1200 km), is optimal to explain the differences between the two Apollo measurements, but overestimates the heat flux at Region 5, of which the uncertainty level is somewhat unclear. A small KREEP size (~800 km) is most consistent with secondary geophysical constraints, coming from volcanic history, crater ring system, and annulus relaxation studies (Broquet & Andrews-Hanna, 2024a; Ding & Zhu, 2022; Hiesinger et al., 2023; Shearer et al., 2023), but can only explain the Apollo measurements if taken at the very edge of their errorbars (15 mW/m^2 for Apollo 15 and 14 mW/m^2 for Apollo 17).

The second part of this work (Part III) is focused on the effect of including a laterally variable thermal conductivity model into the Part II setup. We test multiple thermal conductivity models, which include the presence of basaltic material on the nearside and a porous megaregolith layer on the farside, in order to match constraints related to the viscous relaxation of large basins crustal annuli (Ding & Zhu, 2022). We find that farside crustal conductivity is only negligbly affected by the presence of a porous layer, being comparable to that of compact anorthositic rock (~2 W/(mK)). Conversely, the presence of high-conductivity compact basalt on nearside mare does not allow explaining the observed relaxation, meaning that lunar basalts may have a lower conductivity than expected (<2.5 W/(mK)), or that a more complex treatment of thermal conductivity is needed (i.e. depth-wise pressure-temperature dependence).

Lastly, we explore the possibilities of further improving the present model to increase its inherent consistency. Coupling the thermal evolution with the crustal thickness distribution model through an iterative process, along with including LMO crystallization model data to anchor our initial conditions is deemed pivotal to further increase our understanding of lunar thermal evolution. Similarly, the model can greatly benefit from the inclusion of features such as melt production, tidal deformation, and tidal energy, which can provide further independent constraints to evaluate the different models.

Bibliography

Andrews-Hanna, J. C., Besserer, J., Head III, J. W., Howett, C. J. A., Kiefer, W. S., Lucey, P. J., McGovern, P. J., Melosh, H. J., Neumann, G. A., Phillips, R. J., Schenk, P. M., Smith, D. E., Solomon, S. C., & Zuber, M. T. (2014). Structure and evolution of the lunar procellarum region as revealed by grail gravity data. *Nature*, *514*(7520), 68–71. https://doi.org/10.1038/nature13697

Breuer, D., & Moore, W. (2015). Dynamics and thermal history of the terrestrial planets, the moon, and io. In *Treatise on geophysics* (pp. 255–305). Elsevier. https://doi.org/10.1016/b978-0-444-53802-4.00173-1

Breuer, D. (2009). 4.2.3.4 dynamics and thermal evolution. In *Landolt-börnstein - group vi astronomy and astrophysics* (pp. 323–344). Springer Berlin Heidelberg. https://doi.org/10.1007/978-3-540-88055-4_19

Broquet, A., & Andrews-Hanna, J. (2024a). The moon before mare. *Icarus*, *408*, 115846. https://doi.org/10.1016/j.icarus.2023.115846

Broquet, A., & Andrews-Hanna, J. (2024b). A volcanic inventory of the moon. *Icarus*, *411*, 115954. https://doi.org/10.1016/j.icarus.2024.115954

Canup, R. M., Righter, K., Dauphas, N., Pahlevan, K., Ćuk, M., Lock, S. J., Stewart, S. T., Salmon, J., Rufu, R., Nakajima, M., & Magna, T. (2023). Origin of the moon. *Reviews in Mineralogy and Geochemistry*, *89*(1), 53–102. https://doi.org/10.2138/rmg.2023.89.02

Crawford, I. A., Anand, M., Barber, S., Cowley, A., Crites, S., Fa, W., Flahaut, J., Gaddis, L. R., Greenhagen, B., Haruyama, J., Hurley, D., McLeod, C. L., Morse, A., Neal, C. R., Sargeant, H., Sefton-Nash, E., & Tartèse, R. (2023). Lunar resources. *Reviews in Mineralogy and Geochemistry*, *89*(1), 829–868. https://doi.org/10.2138/rmg.2023.89.19

Davaille, A. (1999). Simultaneous generation of hotspots and superswells by convection in a heterogeneous planetary mantle. *Nature*, *402*(6763), 756–760. https://doi.org/10.1038/45461

Davies, J. H., & Davies, D. R. (2010). Earth's surface heat flux. *Solid Earth*, *1*(1), 5–24. https://doi.org/10.5194/se-1-5-2010

Ding, M., & Zhu, M.-H. (2022). Effects of regional thermal state on the crustal annulus relaxation of lunar large impact basins. *Journal of Geophysical Research: Planets*, *127*(3). https://doi.org/10.1029/2021je007132

Dziewonski, A. M., & Anderson, D. L. (1981). Preliminary reference earth model. *Physics of the Earth and Planetary Interiors*, *25*(4), 297–356. https://doi.org/10.1016/0031-9201(81)90046-7

Elardo, S. M., Laneuville, M., McCubbin, F. M., & Shearer, C. K. (2020). Early crust building enhanced on the moon's nearside by mantle melting-point depression. *Nature Geoscience*, *13*(5), 339–343. https://doi.org/10.1038/s41561-020-0559-4

Gaddis, L. R., Joy, K. H., Bussey, B. J., Carpenter, J. D., Crawford, I. A., Elphic, R. C., Halekas, J. S., Lawrence, S. J., & Xiao, L. (2023). Recent exploration of the moon: Science from lunar missions since 2006. *Reviews in Mineralogy and Geochemistry*, *89*(1), 1–51. https://doi.org/10.2138/rmg.2023.89.01

Gaffney, A. M., Gross, J., Borg, L. E., Hanna, K. L. D., Draper, D. S., Dygert, N., Elkins-Tanton, L. T., Prissel, K. B., Prissel, T. C., Steenstra, E. S., & van Westrenen, W. (2023). Magmatic evolution i: Initial differentiation of the moon. *Reviews in Mineralogy and Geochemistry*, *89*(1), 103–145. https://doi.org/10.2138/rmg.2023.89.03

Gong, S., Wieczorek, M. A., Nimmo, F., Kiefer, W. S., Head, J. W., Huang, C., Smith, D. E., & Zuber, M. T. (2016). Thicknesses of mare basalts on the moon from gravity and topography. *Journal of Geophysical Research: Planets*, *121*(5), 854–870. https://doi.org/10.1002/2016je005008

Grott, M., Knollenberg, J., Hamm, M., Ogawa, K., Jaumann, R., Otto, K. A., Delbo, M., Michel, P., Biele, J., Neumann, W., Knapmeyer, M., Kührt, E., Senshu, H., Okada, T., Helbert, J., Maturilli, A., Müller, N., Hagermann, A., Sakatani, N., … Moussi-Soffys, A. (2019). Low thermal conductivity boulder with high porosity identified on c-type asteroid (162173) ryugu. *Nature Astronomy*, *3*(11), 971–976. https://doi.org/10.1038/s41550-019-0832-x

Grott, M., Knollenberg, J., & Krause, C. (2010). Apollo lunar heat flow experiment revisited: A critical reassessment of the in situ thermal conductivity determination. *Journal of Geophysical Research: Planets*, *115*(E11). https://doi.org/10.1029/2010je003612

Halbert, D., & Parnell, J. (2022). Thermal conductivity of basalt between 225 and 290k. *Meteoritics & Planetary Science*, *57*(8), 1617–1626. https://doi.org/10.1111/maps.13829

Heiken, G. H., Vaniman, D. T., & French, B. M. (1991). *Lunar Sourcebook, A User's Guide to the Moon*.

Henke, S., Gail, H.-P., & Trieloff, M. (2016). Thermal evolution and sintering of chondritic planetesimals: Iii. modelling the heat conductivity of porous chondrite material. *Astronomy & Astrophysics*, *589*, A41. https://doi.org/10.1051/0004-6361/201527687

Hiesinger, H., van der Bogert, C., Michael, G., Schmedemann, N., Iqbal, W., Robbins, S., Ivanov, B., Williams, J.-P., Zanetti, M., Plescia, J., Ostrach, L. R., & Head, J. (2023). The lunar cratering chronology. *Reviews in Mineralogy and Geochemistry*, *89*(1), 401–451. https://doi.org/10.2138/rmg.2023.89.10

Huang, Q., & Wieczorek, M. A. (2012). Density and porosity of the lunar crust from gravity and topography. *Journal of Geophysical Research: Planets*, *117*(E5). https://doi.org/10.1029/2012je004062

Hüttig, C., & Stemmer, K. (2008a). The spiral grid: A new approach to discretize the sphere and its application to mantle convection. *Geochemistry, Geophysics, Geosystems*, *9*(2). https://doi.org/10.1029/2007gc001581

Hüttig, C., & Stemmer, K. (2008b). Finite volume discretization for dynamic viscosities on voronoi grids. *Physics of the Earth and Planetary Interiors*, *171*(1–4), 137–146. https://doi.org/10.1016/j.pepi.2008.07.007

Hüttig, C., Tosi, N., & Moore, W. B. (2013). An improved formulation of the incompressible navier–stokes equations with variable viscosity. *Physics of the Earth and Planetary Interiors*, *220*, 11–18. https://doi.org/10.1016/j.pepi.2013.04.002

Jansen, J., Andrews-Hanna, J., Li, Y., Lucey, P., Taylor, G., Goossens, S., Lemoine, F., Mazarico, E., Head, J., Milbury, C., Kiefer, W., Soderblom, J., & Zuber, M. (2017). Small-scale density variations in the lunar crust revealed by grail. *Icarus*, *291*, 107–123. https://doi.org/10.1016/j.icarus.2017.03.017

Ji, J., Guo, D., Liu, J., Chen, S., Ling, Z., Ding, X., Han, K., Chen, J., Cheng, W., Zhu, K., Liu, J., Wang, J., Chen, J., & Ouyang, Z. (2022, June). The 1:2,500,000-Scale Geologic Map of the Global Moon. https://doi.org/10.12176/03.99.02797

Jolliff, B. L., Gillis, J. J., Haskin, L. A., Korotev, R. L., & Wieczorek, M. A. (2000). Major lunar crustal terranes: Surface expressions and crust□mantle origins. *Journal of Geophysical Research: Planets*, *105*(E2), 4197–4216. https://doi.org/10.1029/1999je001103

Kawamura, T., Lognonné, P., Nishikawa, Y., & Tanaka, S. (2017). Evaluation of deep moonquake source parameters: Implication for fault characteristics and thermal state. *Journal of Geophysical Research: Planets*, *122*(7), 1487–1504. https://doi.org/10.1002/2016je005147

Konopliv, A. S., Park, R. S., Yuan, D.-N., Asmar, S. W., Watkins, M. M., Williams, J. G., Fahnestock, E., Kruizinga, G., Paik, M., Strekalov, D., Harvey, N., Smith, D. E., & Zuber, M. T. (2013). The jpl lunar gravity field to spherical harmonic degree 660 from the grail primary mission. *Journal of Geophysical Research: Planets*, *118*(7), 1415–1434. https://doi.org/10.1002/jgre.20097

Laneuville, M., Taylor, J., & Wieczorek, M. A. (2018). Distribution of radioactive heat sources and thermal history of the moon. *Journal of Geophysical Research: Planets*, *123*(12), 3144–3166. https://doi.org/10.1029/2018je005742

Laneuville, M., Wieczorek, M. A., Breuer, D., & Tosi, N. (2013). Asymmetric thermal evolution of the moon. *Journal of Geophysical Research: Planets*, *118*(7), 1435–1452. https://doi.org/10.1002/jgre.20103

Langseth, M. G., Keihm, S. J., & Peters, K. A. (1976). The revised lunar heat flow values. https://api.semanticscholar.org/CorpusID:91317287

Lawrence, D. J., Feldman, W. C., Barraclough, B. L., Binder, A. B., Elphic, R. C., Maurice, S., Miller, M. C., & Prettyman, T. H. (1999). High resolution measurements of absolute thorium abundances on the lunar surface. *Geophysical Research Letters*, *26*(17), 2681–2684. https://doi.org/10.1029/1999gl008361

Li, H., Zhang, N., Liang, Y., Wu, B., Dygert, N. J., Huang, J., & Parmentier, E. M. (2019). Lunar cumulate mantle overturn: A model constrained by ilmenite rheology. *Journal of Geophysical Research: Planets*, *124*(5), 1357–1378. https://doi.org/10.1029/2018je005905

Liang, W., Broquet, A., Andrews-Hanna, J. C., Zhang, N., Ding, M., & Evans, A. J. (2024). Vestiges of a lunar ilmenite layer following mantle overturn revealed by gravity data. *Nature Geoscience*, *17*(4), 361–366. https://doi.org/10.1038/s41561-024-01408-2

Liu, T., Wünnemann, K., & Michael, G. (2022). 3d-simulation of lunar megaregolith evolution: Quantitative constraints on spatial variation and size of fragment. *Earth and Planetary Science Letters*, *597*, 117817. https://doi.org/10.1016/j.epsl.2022.117817

McDonough, W., & Sun, S.-s. (1995). The composition of the earth. *Chemical Geology*, *120*(3–4), 223–253. https://doi.org/10.1016/0009-2541(94)00140-4

Nayler, J. L. (1969). Soviet space exploration—the first decade. w. shelton. arthur barker, london. 1969. 350 pp. illustrated. 45s. *The Aeronautical Journal*, *73*(700), 342–342. https://doi.org/10.1017/s0001924000053094

Neumann, W., Breuer, D., & Spohn, T. (2014). Differentiation of vesta: Implications for a shallow magma ocean. *Earth and Planetary Science Letters*, *395*, 267–280. https://doi.org/10.1016/j.epsl.2014.03.033

Nozette, S., Rustan, P., Pleasance, L. P., Horan, D. M., Regeon, P., Shoemaker, E. M., Spudis, P. D., Acton, C. H., Baker, D. N., Blamont, J. E., Buratti, B. J., Corson, M. P., Davies, M. E., Duxbury, T. C., Eliason, E. M., Jakosky, B. M., Kordas, J. F., Lewis, I. T., Lichtenberg, C. L., … Zuber, M. T. (1994). The clementine mission to the moon: Scientific overview. *Science*, *266*(5192), 1835–1839. Retrieved March 25, 2024, from http://www.jstor.org/stable/2885032

Paige, D., & Siegler, M. (2016). NEW CONSTRAINTS ON LUNAR HEAT FLOW RATES FROM LRO DIVINER LUNAR RADIOMETER EXPERIMENT POLAR OBSERVATIONS (47th ed.).

Plesa, A.-C. (2011). Mantle convection in a 2d spherical shell. *INFOCOMP 2011: The First International Conference on Advanced Communications and Computation, Barcelona, Spain*, 167–172.

Plesa, A.-C., Hüttig, C., Maurice, M., Breuer, D., & Tosi, N. (2016). Large scale numerical simulations of planetary interiors. In W. E. Nagel, D. H. Kröner, & M. M. Resch (Eds.), *High performance computing in science and engineering ’15* (pp. 675–687). Springer International Publishing.

Plesa, A.-C., Tosi, N., & Hüttig, C. (2013). Thermo-chemical convection in planetary mantles: Advection methods and magma ocean overturn simulations. In *Integrated information and computing systems for natural, spatial, and social sciences* (pp. 302–323). IGI Global. https://doi.org/10.4018/978-1-4666-2190-9.ch015

Plescia, J., Cahill, J., Greenhagen, B., Hayne, P., Mahanti, P., Robinson, M., Spudis, P., Siegler, M., Stickle, A., Williams, J., Zanetti, M., & Zellner, N. (2023). Lunar surface processes. *Reviews in Mineralogy and Geochemistry*, *89*(1), 651–690. https://doi.org/10.2138/rmg.2023.89.15

Richardson, J. E., & Abramov, O. (2020). Modeling the formation of the lunar upper megaregolith layer. *The Planetary Science Journal*, *1*(1), 2. https://doi.org/10.3847/psj/ab7235

Schonfeld, J. (2023). Summary of the contracted deliveries of nasa payloads to the moon via commercial lunar payload services (clps). *2023 IEEE International Conference on Systems, Man, and Cybernetics (SMC)*, 863–866. https://doi.org/10.1109/SMC53992.2023.10394001

Schubert, G., Spohn, T., & Reynolds, R. T. (1986). *Thermal histories, compositions, and internal structures of the moons of the solar system* (J. A. Burns & M. S. Matthews, Eds.) [Provided by the SAO/NASA Astrophysics Data System]. IAU Colloq. 77: Some Background about Satellites. https://ui.adsabs.harvard.edu/abs/1986sats.book..224S

Schubert, G., Turcotte, D. L., & Olson, P. (2001, September). *Mantle convection in the earth and planets*. Cambridge University Press. https://doi.org/10.1017/cbo9780511612879

Shearer, C., Neal, C. R., Glotch, T. D., Prissel, T. C., Bell, A. S., Fernandes, V. A., Gaddis, L. R., Jolliff, B. L., Laneuville, M., Magna, T., & Simon, J. (2023). Magmatic evolution ii: A new view of post-differentiation magmatism. *Reviews in Mineralogy and Geochemistry*, *89*(1), 147–206. https://doi.org/10.2138/rmg.2023.89.04

Siegler, M. A., Miller, R. S., Keane, J. T., Laneuville, M., Paige, D. A., Matsuyama, I., Lawrence, D. J., Crotts, A., & Poston, M. J. (2016). Lunar true polar wander inferred from polar hydrogen. *Nature*, *531*(7595), 480–484. https://doi.org/10.1038/nature17166

Siegler, M., Feng, J., Lehman-Franco, K., Andrews-Hanna, J. C., Economos, R. C., Clair, M. S., Million, C., Head, J. W., Glotch, T. D., & White, M. N. (2023). Remote detection of a lunar granitic

batholith at compton–belkovich. *Nature*, *620*(7972), 116–121. https://doi.org/10.1038/s41586-023-06183-5

Siegler & Smrekar. (2014). Lunar heat flow: Regional prospective of the apollo landing sites. *Journal of Geophysical Research: Planets*, *119*(1), 47–63. https://doi.org/10.1002/2013je004453

Steinbach, V., & Yuen, D. A. (1994). Effects of depth-dependent properties on the thermal anomalies produced in flush instabilities from phase transitions. *Physics of the Earth and Planetary Interiors*, *86*(1–3), 165–183. https://doi.org/10.1016/0031-9201(94)05067-8

Stevenson, D. J., Spohn, T., & Schubert, G. (1983). Magnetism and thermal evolution of the terrestrial planets. *Icarus*, *54*(3), 466–489. https://doi.org/10.1016/0019-1035(83)90241-5

Thompson, T. W., Roberts, W. J., Hartmann, W. K., Shorthill, R. W., & Zisk, S. H. (1979). Blocky craters: Implications about the lunar megaregolith. *The Moon and the Planets*, *21*(3), 319–342. https://doi.org/10.1007/bf00897360

Thomson, J. (1904). Xxiv. on the structure of the atom: An investigation of the stability and periods of oscillation of a number of corpuscles arranged at equal intervals around the circumference of a circle; with application of the results to the theory of atomic structure. *The London, Edinburgh, and Dublin Philosophical Magazine and Journal of Science*, *7*(39), 237–265. https://doi.org/10.1080/14786440409463107

Tosi, N., Breuer, D., & Spohn, T. (2014). Evolution of planetary interiors. In *Encyclopedia of the solar system* (pp. 185–208). Elsevier. https://doi.org/10.1016/b978-0-12-415845-0.00009-8

Tosi, N., Yuen, D. A., de Koker, N., & Wentzcovitch, R. M. (2013). Mantle dynamics with pressure- and temperature-dependent thermal expansivity and conductivity. *Physics of the Earth and Planetary Interiors*, *217*, 48–58. https://doi.org/https://doi.org/10.1016/j.pepi.2013.02.004

Wahl, D., & Oberst, J. (2019). Lateral variations in bulk density and porosity of the upper lunar crust from high-resolution gravity and topography data: Comparison of different analysis techniques. *ISPRS Annals of the Photogrammetry, Remote Sensing and Spatial Information Sciences*, *IV-2/W5*, 527–532. https://doi.org/10.5194/isprs-annals-iv-2-w5-527-2019

Wahl, D., Wieczorek, M. A., Wünnemann, K., & Oberst, J. (2020). Crustal porosity of lunar impact basins. *Journal of Geophysical Research: Planets*, *125*(4). https://doi.org/10.1029/2019je006335

Warren, P. H., & Rasmussen, K. L. (1987). Megaregolith insulation, internal temperatures, and bulk uranium content of the moon. *Journal of Geophysical Research: Solid Earth*, *92*(B5), 3453–3465. https://doi.org/10.1029/jb092ib05p03453

Wieczorek, M. A. (2018). Strength, depth, and geometry of magnetic sources in the crust of the moon from localized power spectrum analysis. *Journal of Geophysical Research: Planets*, *123*(1), 291–316. https://doi.org/10.1002/2017je005418

Wieczorek, M. A., Neumann, G. A., Nimmo, F., Kiefer, W. S., Taylor, G. J., Melosh, H. J., Phillips, R. J., Solomon, S. C., Andrews-Hanna, J. C., Asmar, S. W., Konopliv, A. S., Lemoine, F. G., Smith, D. E., Watkins, M. M., Williams, J. G., & Zuber, M. T. (2013). The crust of the moon as seen by grail. *Science*, *339*(6120), 671–675. https://doi.org/10.1126/science.1231530

Williams, J. G., & Boggs, D. H. (2015). Tides on the moon: Theory and determination of dissipation. *Journal of Geophysical Research: Planets*, *120*(4), 689–724. https://doi.org/10.1002/2014je004755

Williams, J. G., Konopliv, A. S., Boggs, D. H., Park, R. S., Yuan, D.-N., Lemoine, F. G., Goossens, S., Mazarico, E., Nimmo, F., Weber, R. C., Asmar, S. W., Melosh, H. J., Neumann, G. A., Phillips, R. J., Smith, D. E., Solomon, S. C., Watkins, M. M., Wieczorek, M. A., Andrews-Hanna, J. C., … Zuber, M. T. (2014). Lunar interior properties from the grail mission: Lunar interior properties. *Journal of Geophysical Research: Planets*, *119*(7), 1546–1578. https://doi.org/10.1002/2013je004559

Xin, L. (2024). China's chang'e-6 launched successfully — what happens next? *Nature*. https://doi.org/10.1038/d41586-024-01345-5

Zhang, Ding, M., Zhu, M.-H., Li, H., Li, H., & Yue, Z. (2022). Lunar compositional asymmetry explained by mantle overturn following the south pole–aitken impact. *Nature Geoscience*, *15*(1), 37–41. https://doi.org/10.1038/s41561-021-00872-4

Zhang, J., Head, J., Liu, J., & Potter, R. (2023). Lunar procellarum kreep terrane (pkt) stratigraphy and structure with depth: Evidence for significantly decreased th concentrations and thermal evolution consequences. *Remote Sensing*, *15*(7), 1861. https://doi.org/10.3390/rs15071861